

WARSAW UNIVERSITY OF TECHNOLOGY

FACULTY OF MECHATRONICS

Ph.D. Thesis

Wojciech Krauze, M.Sc.

**Method for the numerical analysis of phase biological
microsamples in limited-angle optical tomography**

Supervisor

Prof. dr hab. inż. Małgorzata Kujawińska

Co-supervisor

Dr inż. Piotr Makowski

WARSAW 2018

Streszczenie

Obrazowanie ilościowe jest źródłem ważnych informacji na temat komórek i wycinków tkanek. Najpopularniejszym narzędziem wykorzystywanym w tym celu jest optyczna tomografia dyfrakcyjna (OTD), która jest techniką nieniszczącą i niewymagającą barwienia. Szczególną popularność w środowisku medycznym zyskała technika OTD z ograniczonym zakresem kątowym projekcji (OTDOK). Ograniczony zakres kątowy skutkuje jednak zniekształconymi rekonstrukcjami tomograficznymi, dlatego kluczowe jest opracowanie dedykowanych metod przetwarzania danych do tej metody.

W ramach rozprawy doktorskiej opracowano pełną ścieżkę przetwarzania danych pozyskanych z układu OTDOK w celu dokładnej rekonstrukcji rozkładu trójwymiarowego współczynnika załamania w strukturach biologicznych. W pracy zaproponowano nową procedurę rekonstrukcji tomograficznej, nazwaną TVIC (ang. *Total Variation Iterative Constraint*). Metoda wykorzystuje minimalizację wahania rekonstrukcji w celu odtworzenia granic obiektu oraz algorytm Gerchberga-Papoulisa w celu obliczenia rozkładu współczynnika załamania wewnątrz tych granic. Metoda ta w znaczący sposób zmniejsza zniekształcenie zrekonstruowanych obiektów biologicznych oraz błęd rozkładu współczynnika załamania. Aby zbadać skuteczność zaproponowanej techniki, przeprowadzono szereg symulacji na dedykowanych fantomach numerycznych. Testy te zawierają porównanie wyników otrzymanych metodą TVIC z rekonstrukcjami obliczonymi algorytmami referencyjnymi. Przeprowadzono też analizę zbieżności oraz badanie wpływu liczby projekcji na jakość rekonstrukcji tomograficznej. Wyniki potwierdzają, że wykorzystanie strategii TVIC skutkuje uzyskaniem rekonstrukcji z wyraźniejszymi krawędziami obiektu, bez artefaktów typowych dla OTDOK oraz z poprawionymi wartościami rozkładu współczynnika załamania. Obserwacje te potwierdziły wyniki eksperymentów w których mikro-kulka oraz komórka fibroblastu mierzone były w układzie OTDOK i zrekonstruowane przy użyciu strategii TVIC oraz metod referencyjnych.

Dodatkowo, w celu zwiększenia możliwości stosowania OTDOK, opracowano metodę zwiększenia głębi ostrości. Realizuje się ją poprzez wprowadzenie soczewki zmiennooogniskowej do układu optycznego OTDOK oraz opracowanie dedykowanego przetwarzania danych. W metodzie tej obliczana jest seria rekonstrukcji tomograficznych z różnym przeogniskowaniem, a końcowy wynik uzyskiwany jest poprzez zszycie fragmentów rekonstrukcji znajdujących się w zakresie syntetycznej głębi ostrości. Skuteczność tej techniki potwierdzają wyniki pomiarów mikrokulki, komórki fibroblastu i histologicznego wycinka tkanki.

Słowa kluczowe: *optyka, cyfrowa mikroskopia holograficzna, optyczna tomografia dyfrakcyjna, algorytmy rekonstrukcji tomograficznej, oszczędne próbkowanie, mikro-struktury biologiczne.*

Abstract

Three-dimensional imaging of biological specimens provides important information on biology of cells and tissue samples. The most popular tool for this purpose is optical diffraction tomography (ODT) which is a label-free and non-destructive technique. For the investigation of bio-samples, limited angle ODT (LAODT) is especially promising as its mode of operation is suited for the microscopic measurement convention at medical and biological communities. However, in LAODT projections of a specimen are captured within a limited angular range which leads to distorted reconstructions of the refractive index. Thus, it is crucial that dedicated reconstruction methods are developed.

The objective of the Thesis is to develop a complete processing path for data provided by the LAODT system with the aim of accurate reconstruction of 3D refractive index distribution in biological specimens. In the Thesis the novel tomographic reconstruction strategy, called Total Variation Iterative Constraint (TVIC), is proposed. It is a two-stage approach where total variation minimization retrieves the distortion-free external boundaries of the sample and the Gerchberg-Papoulis algorithm reconstructs the refractive index distribution within these boundaries. It reduces significantly the geometrical distortion and the errors in refractive index value in the case of biological structures with non-piecewise constant refractive index. To prove the effectiveness of TVIC, extensive numerical simulations on dedicated phantoms are carried out. These tests include comparison of TVIC results with reconstructions calculated with reference techniques: Gerchberg-Papoulis and Direct Inversion methods, algorithm convergence analysis as well as dependence of the reconstruction quality on the number of input projections. The results prove that when TVIC strategy is used, reconstructions with sharper object boundaries, limited LAODT artifacts and with more correct refractive index distribution of internal structures are obtained. These observations are confirmed by physical experiments where a PMMA micro-sphere and a fibroblast cell are measured with the LAODT setup and are reconstructed with TVIC and reference methods.

Additionally, in order to enhance the applicability of LAODT, the method of increasing the depth of field is developed. This is realized through insertion of a focus-tunable lens into the LAODT optical setup and through development of dedicated data processing. In this method, a series of defocused tomographic reconstructions is calculated and the final result is created by stitching those fragments of the reconstructions that are within the synthetic depth-of-field. The effectiveness of this technique is proved with experimental analyses performed on a micro-sphere, fibroblast cell and histological tissue slice.

Keywords: *optics, digital holographic microscopy, optical diffraction tomography, tomographic reconstruction algorithms, compressed sensing, biological micro-structures.*

Contents

1	Introduction	7
1.1	Motivation	7
1.2	Aim of the Thesis	9
1.3	Structure of the Thesis	11
1.4	Sources of funding and acknowledgements	11
2	State of the art	12
2.1	Quantitative phase imaging in biological studies	12
2.2	Optical diffraction tomography	14
2.2.1	Optical design	15
2.2.2	Born and Rytov approximations	16
2.2.3	Fourier Diffraction Theorem	21
2.3	Limited-angle optical diffraction tomography	23
2.3.1	Illumination rotation	26
2.3.2	Limitation of LAODT	27
2.3.3	Reconstruction algorithms in LAODT	29
2.4	Quality assessment criteria	32
2.5	Conclusions	33
3	Total Variation Iterative Constraint Method	35
3.1	General description	37
3.2	Reconstruction clearing procedures	39
3.3	Numerical experiments & quality assessment	40
3.3.1	Method	42
3.3.2	Proof of concept	44
3.3.3	Convergence analysis	47
3.3.4	Dependence of the reconstruction quality on the number of projections	52
3.3.5	Analysis of the reconstruction clearing efficiency	53
3.4	Conclusions	57

4	Extended depth-of-field LAODT	58
4.1	Problem description	58
4.2	Main concept	61
4.2.1	Numerical procedures	62
4.3	Conclusions	64
5	Physical experiments	65
5.1	LAODT with TVIC-GP	65
5.1.1	LAODT setup	65
5.1.2	Objects description	66
5.1.3	Experimental results	68
5.1.4	Conclusions	72
5.2	Focus-tunable tomography with TVIC-GP	73
5.2.1	Focus-tunable tomography setup	73
5.2.2	Objects description	73
5.2.3	Experimental results	73
5.2.4	Conclusions	78
6	Conclusions and future trends	81
6.1	Conclusions	81
6.2	Future works	83
	References	85

Chapter 1

Introduction

1.1 Motivation

In the year 2015, almost 1 in 6 deaths was caused by cancer, overtaking cardiovascular disease in some countries [1]. This number will supposedly double during the next 20 years. Not surprisingly, enormous effort is currently directed towards new techniques for cancer treatment. A significant amount of money is spent on projects like Cancer Moonshot in the USA (\$1.8 billion from 2017 to 2024) [2] or projects under European Union Seventh Framework Programme (€ 1.5 billion from 2007 to 2013 with twice as much funding under the Horizon 2020 program) [3]. One of the key priorities in these projects is non-destructive, optical in vitro analysis of the process of transformation from a healthy to a cancer cell.

Another trend visible today is the shift from standard towards digital histology, where histological samples are automatically measured, instead of just being visualized. After the specimen is analyzed, its digital copy is stored on a computer, where it can either be evaluated by a medical doctor or by specialized software.

The common factor in the above examples is the need for a quantitative, fast and reliable method for measuring biological specimens. Until recently, the main tool for in vitro investigation of biological specimens was the standard optical microscopy, which provides qualitative information about the optical field intensity values integrated along the optical axis, which then can be assessed by a medical doctor. To increase the physiological contrast, multiple histological stains are utilized in the process. However, this technique highly depends on the expertise of a doctor and has several disadvantages and limitations. Firstly, the resulting qualitative image of a sample given by the microscope setup strongly depends on the concentration of the stains in the structures of an analyzed specimen, which cannot be precisely controlled. As an effect, images of the same biological structure differ between laboratories worldwide and thus it is difficult (if not impossible) to create objective standards for automatic identification of the

investigated cells based on these images. What is more, due to lack of repeatability of the results, it is not known whether the achieved results are associated with the investigated cellular processes or with the sample preparation itself. Secondly, the staining procedure can be time consuming and it increases the cost of a sample preparation stage. Thirdly, the optical microscopy creates a two-dimensional image only, where the in-focus cell structures overlap with the blurred background. This makes it difficult to properly assess cell anatomy and requires an experienced histology doctor. The main advantages of fluorescence microscopy are enormous popularity, relatively low price and large database with the results.

Other techniques that gained popularity are fluorescence and confocal microscopy. In the case of a fluorescence imaging, fluorophores are introduced into an investigated specimen. When illuminated with a specific wavelength, they emit a different wavelength which can be isolated by the optical setup. Depending on the type of a fluorophore, it is accumulated in different inner structures of a measured bio-sample, and thus this technique is characterized with remarkable functional contrast. An enhancement of the fluorescent microscopy is the confocal microscopy, in which two pinholes are introduced into the optical setup. The purpose of these pinholes is to couple only a small region (ideally, a point) of an investigated sample with the detector. This region can be localized inside the object, so when the sample is scanned for several depths, a 3D high-resolution image of the fluorophore distribution is created. It should be noted that confocal microscopy can be realized without fluorescence, however this mode of operation is the most popular one for biological studies. Unfortunately, fluorescent-based techniques suffer from phototoxicity of the fluorophores used during the measurement, which can alter the properties of an analyzed bio-sample. Also, these methods are subject to photobleaching which significantly limits the time allowed for the measurement of a single object. Furthermore, only qualitative information on the concentration of fluorophores is provided.

These problems inspired researchers to develop a new type of optical techniques, namely quantitative phase imaging (QPI) methods. In general, QPI aims to quantitatively measure the phase of an optical field in an object plane, which then can be used to retrieve the information about refractive index values in the analyzed sample. Similarly to optical microscopy, QPI techniques are non-destructive, however, no biomarkers are required. This means that the measurements of a sample should give the same results regardless of the laboratory where the measurement has been conducted. This allows to create objective standards in evaluation of biological specimens. What is more, QPI can potentially provide possibility to measure live cells in real-time. Among all QPI methods, two have gained more popularity: digital holographic microscopy (DHM) [4] and optical diffraction tomography (ODT) based on holographic projections [5, 6]. DHM, despite being a quantitative technique, returns a two-dimensional integrated phase distribution only. A very strict conditions have to be fulfilled for DHM to provide refractive index distribution in the object plane and most biological samples do not meet these require-

ments. ODT, on the other hand, provides information about three-dimensional (3D) refractive index distribution. This technique is similar to Computed Tomography: an analyzed object is illuminated from various directions and a series of projections is acquired. These projections are then numerically reconstructed to provide 3D refractive index distribution of an investigated sample. In the most common setup, the micro-specimen is placed in a chamber which then is rotated by 360° . A stationary source and detector are used to capture object projections during this rotation. This configuration is called full-angle ODT (FAODT). Its main advantage is the high quality of 3D reconstructions. Its main drawback is associated with the fact that most biological specimens cannot be rotated unperturbed and thus this method is dedicated mainly to technical samples. Another type of ODT is limited-angle ODT (LAODT), where the sample and detector are stationary while the illumination direction is changing. With this type of tomography biological micro-objects can be investigated directly from Petri dishes. LAODT is thus a perfect candidate for precise and nondestructive method for quantitative in-vitro analysis of cancer cells. However, illumination scanning cannot cover 360° angular range. This, in turn, leads to distorted reconstructions of refractive index distribution. In recent years, multiple tomographic reconstruction algorithms that aim to minimize this distortion have been developed [7]. Until now, only a few methods proved to be successful in providing distortion-free reconstructions in LAODT and none of them are dedicated to investigation of biological micro-samples, which significantly differ from the technical ones in terms of refractive index distribution [8–10]. Development of a tomographic reconstruction algorithm which would provide highly accurate 3D refractive index distribution while being consistent with the characteristics of cellular structures would thus be an important milestone and a significant support in the fight against cancer and in general in investigation of biological micro-objects.

1.2 Aim of the Thesis

The main objective (MO) is to develop the complete processing path for data (projections) provided by the limited angle optical diffraction tomography system with the aim of accurate, label-free quantitative 3D investigation of biological specimens.

The label-free nature of the measurement refers to the fact that in a standard biological or histological laboratory, numerous stains are used. Some, like hematoxylin and eosin, help to differentiate cell nuclei from cytoplasm. Other, like Papanicolaou stain, are used to differentiate whole cells from each other. In the Thesis, no stain is allowed during sample investigation. The differentiation of cell structures or whole cells is based only on 3D refractive index distribution.

One of the most versatile methods of acquiring projections in optical tomography is holography. Thus, in the Thesis, all the projections of an analyzed sample are holograms acquired in an image plane. Therefore, the first task which leads to MO is to develop the data preprocessing

and phase retrieval methods with the aim to provide high quality input data for tomographic reconstruction algorithms.

The second task is to develop the tomographic reconstruction algorithm devoted to LAODT which significantly limits the distortion of reconstructed biological structures that is due to limited angular range of acquired projections. In general, biological structures highly differ from each other in terms of optical characteristics and number of internal structures. Some samples, like red blood cells, have a uniform structure with piecewise-constant refractive index distribution. For these specimens, a strong regularization technique, called Total p-Variation minimization, can be used in the tomographic reconstruction procedure to limit the distortion of the calculated reconstruction. Other samples, like most cancer cells, have quasi piecewise-constant structures (e.g. nucleoli) in a non-piecewise-constant medium (cytoplasm). When the Total p-Variation minimization is used to calculate the reconstructions of such samples, the refractive index distribution in the reconstruction is forced to be piecewise-constant which results in erroneous results. There are no strong, dedicated regularization methods that could be applied to such biological structures. Thus, the tomographic methods described in the Thesis are dedicated to weakly scattering biological micro-objects with non-piecewise-constant refractive index distribution. Such broad definition of a target object highly limits the number of regularization techniques that can be utilized in the developed algorithm, but increases its applicability.

To realize the second task under the assumptions described above, I state the following research hypothesis: In LAODT it is possible to minimize the distortion in tomographic reconstructions of biological samples through a dedicated data processing procedure which includes regularization techniques based on Total p-Variation minimization, while preserving the non-piecewise-constant refractive index distribution of the specimens.

The research carried out to prove the hypothesis provides the background to realize the third task, which is focused on increasing the depth of field of the limited angle optical diffraction tomography and through this extending even more the applicability of LAODT. The shallow depth of field results in non-uniform resolution in the calculated reconstruction. This, in turn, limits the quantitative nature of the measurement. Thus, a robust method for the calculation of tomographic reconstructions with uniform resolution in the whole measurement volume will be developed.

It is important to note that the procedures created for LAODT have to provide fully quantitative refractive index analysis. Therefore, it is necessary to specify the metrological requirements for these procedures. Thus, the algorithms described in the Thesis aim to reconstruct transparent and semi-transparent biological micro-samples with the refractive index error below 0.01, where the error is understood as the maximum difference between the reconstructed refractive index and the true refractive index distribution within the volume of an investigated sample introduced by the numerical procedures described in the Thesis. This constraint guarantees

reliability of the developed numerical method.

1.3 Structure of the Thesis

The Thesis is organized as follows. In Chapter 2 a short overview of techniques used to visualize and measure the phase distribution associated with analyzed biological specimens is carried out. Here, a detailed description of ODT and its modification: LAODT is also given. In Chapter 3 a full analysis of the tomographic reconstruction approach proposed in this Thesis, called TVIC, is conducted. In Chapter 4 a new measurement procedure for the extended depth-of-field tomography is proposed. It combines LAODT, focus-tunable electrical lens and TVIC reconstruction strategy. Next, in Chapter 5 experimental verification of the tomographic procedures proposed in the Thesis is carried out on technical and biological micro-samples. Finally, conclusions and future works are described in Chapter 6.

1.4 Sources of funding and acknowledgements

The research leading to the results described in the Thesis has been financially supported through the projects TEAM/2011-7/7 and TEAM TECH/2016-1/4 of Foundation for Polish Science, both co-financed by the European Union under the European Regional Development Fund. Additionally, it was supported by the Dean's Grant and statutory funds at the Mechatronics Department, Warsaw University of Technology.

The Matlab code for the Gerchberg-Papoulis algorithm has been created by dr Piotr Makowski from Warsaw University of Technology. The code for the Total p-Variation minimization has been provided by Tristan van Leeuwen and Folkert Bleichrodt from Centrum Wiskunde & Informatica, Amsterdam, Netherlands.

The close cooperation with dr Arkadiusz Kuś who was responsible for the development of the optical diffraction tomography setup, carrying out the measurements and providing me with the measurement data is highly acknowledged.

I also direct my words of gratitude to dr Dariusz Śladowski from Medical University of Warsaw, Department of Transplantology and Central Tissue Bank, and dr Ewa Skrzypek from Medical University of Warsaw, Department of Pathology, for the preparation of biological samples and inspiring discussions regarding obtained results.

Chapter 2

State of the art

During the last decades, a slow but steady shift from imaging absorption coefficient of the investigated biological specimens (like in classical biological microscopy) to measuring phase values associated with these specimens is observed. This phase carries information about the refractive index distribution of analyzed samples, which, in turn, may be translated into dry mass density - a key parameter describing biological structures.

For many years, the only possibility to visualize the phase of investigated specimens was utilization of qualitative methods like Zernike phase contrast microscopy [11] or Nomarski interference contrast [12]. The greatest weakness of these techniques is that they do not give access to the values of the phase - they only visualize it. Thus, new imaging techniques, called Quantitative Phase Imaging (QPI) methods, which give access to the values of the phase have been developed and are currently one of the most promising imaging tools in biology and medicine. Thus, in this section a short overview of the most important QPI methods is presented.

2.1 Quantitative phase imaging in biological studies

The most basic technique that allows us to measure integrated phase values of transparent and semi-transparent samples is Digital Holographic Microscopy (DHM) [13]. This method has been implemented in different configurations, including lensless [14, 15] or Mach-Zehnder interferometer [16–18] setups. In DHM the sample is placed between the coherent light source and the detector. In most configurations, a microscope objective is also used to match object spatial bandwidth to camera sampling capabilities and image the sample onto the detector. When the sample is illuminated with a light source, the effect of the interference between the light diffracted by the object and a reference beam is recorded. In the case of the lensless DHM, the reference beam is the part of the illuminating beam which was not diffracted by the specimen. In the Mach-Zehnder setup, the reference beam is introduced by a separate reference arm of the

interferometer. Nevertheless, in both cases by utilizing phase retrieval approaches [19–22], the phase, integrated along the illumination direction, can be calculated. This integrated phase may be, under certain conditions, used to determine the refractive index distribution, the topography map or the dry mass distribution of analyzed samples. It is therefore used in numerous clinical studies [23, 24].

A modification of the DHM approach is the Fourier Ptychographic Microscopy (FPM) [25, 26]. In this method, no reference wave is used to calculate the phase associated with the investigated sample. Instead, multiple partially-coherent sources, usually distributed on a flat surface, illuminate the sample from different directions. The range of illumination angles is, however, highly limited. The sources are turned on one by one, so that at a time only 1 source is illuminating the object. A microscope objective placed behind the sample is imaging the object onto a detector which captures projections. The idea behind FPM is to retrieve the high resolution integrated phase information of an analyzed specimen by iteratively processing low resolution intensity distributions from each projection. The method was thoroughly tested and proved to give satisfactory results especially in the case when relatively large field of view has to be investigated.

Another method which gained popularity in recent years is the spatial light interference microscopy (SLIM) [27]. The technique returns a quantitative information about the integrated phase associated with an investigated sample, which, under certain conditions, can be transformed into the refractive index distribution. In short, the principle of operation of SLIM is based on the Zernike phase contrast method. However, in SLIM the phase delay between the scattered and unscattered parts of the object illuminating beam can be precisely controlled with a spatial light modulator. Thus, a standard method of temporal phase shifting can be applied [22] and the integrated phase can be retrieved. The unquestionable advantage of this approach is the possibility of transforming a standard biological microscope into the SLIM device by simply attaching a small module to the body of the microscope. The disadvantage is the fact that in this configuration only the temporal phase shifting method can be applied which limits the imaging speed. Also, only the integrated phase is retrieved which makes it impossible to analyze multi-layered structures. In other cases, however, the method proved to be a highly useful one [28, 29].

Due to the limitations described above, SLIM has been upgraded and the spatial light interference tomography (SLIT) method has been developed [30]. In SLIT, a series of SLIM images is acquired for different positions of an analyzed sample along the optical axis. Due to the fact that in SLIT a low coherence source is used, the coherence gating is possible, which guarantees a decent sectioning property of SLIT. Thus, when a series of defocused images are stitched, a pseudo 3D reconstruction can be obtained. In order to increase the resolution of the calculated reconstruction, a deconvolution of the reconstruction with the experimentally calculated point

spread function is carried out. When compared to SLIM, SLIT offers increased usability at a cost of increased price and system complexity. However, since SLIT does not involve object rotation with respect to the illuminating beam, the results obtained with this method are not fully three dimensional.

2.2 Optical diffraction tomography

The techniques described above do not provide the full 3D refractive index distribution. An alternative to these techniques is the optical diffraction tomography (ODT) [31, 32]. ODT is a noninvasive, label-free method that gives a fairly easy access to the 3D refractive index distribution of an investigated sample. In ODT the sample is illuminated from numerous directions with a laser beam, and the diffraction patterns of light that went through the investigated object are recorded by an appropriate detector (CCD or CMOS camera) as holograms. In the most popular implementation of ODT, after the first holographic projection is captured, the object is rotated by $\Delta\theta$ and another projection is acquired. The source and detector are both stationary.

After capturing a series of projections (holograms), the data are preprocessed to prepare them in the form required by a tomographic reconstruction algorithm. Here, the most important procedure is phase and amplitude retrieval and phase unwrapping. The phase and amplitude retrieval methods are solely dependent on the optical design of the tomography setup. If the carrier frequency is introduced in the ODT detection plane, the Fourier transform method [20] or the spatial carrier phase shifting method [21] are used to demodulate the phase from a hologram. Alternatively, if no carrier frequency is present, but the phase of the reference beam can be controlled, the temporal phase shifting algorithm can be employed [22]. There are also techniques for phase demodulation when there is no reference arm, like those utilizing transport of intensity equation [33], however, they are rarely used in ODT. Regardless of the method used, after this step the amplitude and wrapped phase distributions from each projection are obtained. In the next step, phase unwrapping has to be applied to the wrapped phase. One of the most popular approaches adapted by multiple research groups is the algorithm based on sorting by reliability [34]. However, other techniques like phase unwrapping via graph cuts [35] are also used.

When phase and amplitude distributions are retrieved and processed, they are stacked on top of each other to form the phase and amplitude sinograms. It should be noted that when this process is finished, a complex amplitude distribution u from each holographic projection can be calculated, according to Eq. 2.1.

$$u = A \cdot \exp(i\phi) \quad (2.1)$$

where A and ϕ are amplitude and phase, respectively. The projection acquisition setup and

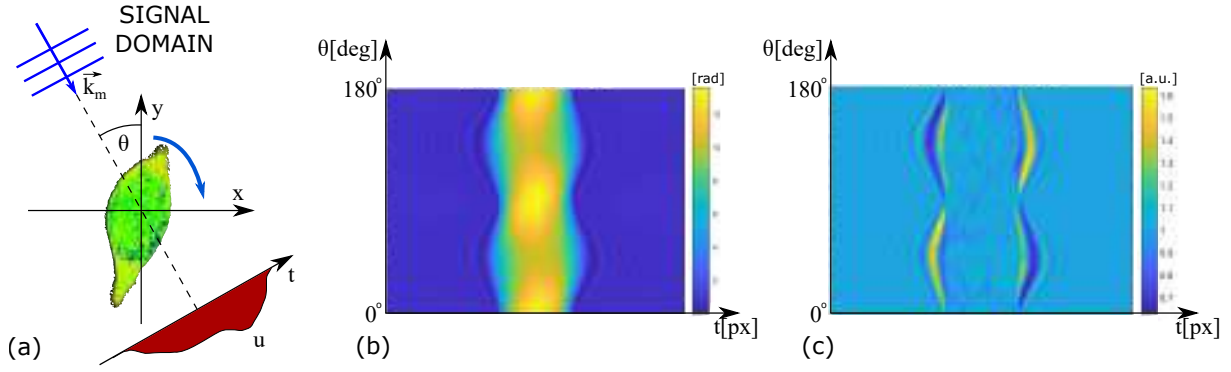


Figure 2.1: Projection acquisition scenario in ODT (a) and the resulting phase (b) and amplitude (c) sinograms. \vec{k}_m - wave vector representing the illuminating plane wave; θ - object rotation angle; u - retrieved complex amplitude.

an example of sinograms are presented in Fig. 2.1. Finally, based on the complex amplitudes, the object function is retrieved by means of dedicated numerical algorithms.

ODT can be used to investigate both technical and biological microsamples. Depending on the type of an analyzed sample, different methods of object rotation have been utilized. When technical samples are under study, the most widely used method is attaching the sample directly to a motorized rotation stage [36, 37]. When biological specimens are measured, it is a common approach to insert these structures into a glass capillary or a hollow-core optical fiber which then is connected to the motorized stage [38, 39]. Alternative solutions include optical tweezers [40], which, however, due to high intensity levels may harm the investigated biological cell.

2.2.1 Optical design

In terms of the optical design of the ODT setup, three configurations are particularly popular. The most widely used is the ODT based on the old concept of the Mach-Zehnder interferometer [41–45], presented in Fig. 2.2(a). In this configuration, the laser beam is divided by a beam splitter into the object beam, which later illuminates an investigated sample, and the reference beam which propagates in free space and interferes with the object beam at the detector plane. The main advantage of this setup is the direct access to the object and reference arms. It is thus relatively easy to utilize different methods for phase retrieval, like the Fourier or spatial carrier phase shifting method (by tilting the reference arm with respect to the object beam which results in carrier fringes at the detector plane) or the temporal phase shifting method (by substituting one of the mirrors in the Mach-Zehnder setup with a piezoelectric mirror). Undoubtedly, the main drawback of this setup is its instability, which is directly associated with the fact that the reference and object beams do not share a common path and thus are subject to different environmental disturbances. Still, however, its versatility makes it the most popular configuration used in ODT.

One alternative to the Mach-Zehnder configuration is the common-path setup [46–48], shown in Fig. 2.2(b). The main concept behind this technique is splitting the laser beam into the object and reference arms after the light passes through an investigated sample. From the laser source down to the specimen, only 1 beam is present. Behind the sample, a diffraction grating is placed in the image plane of the imaging microscope objective. As an effect, several copies of the object field are created as diffraction orders, from which all but two are filtered out. From the remaining two diffraction orders, one is low-pass filtered. Finally, both orders interfere at the detector. Due to the low-pass filtering of one of the beams, the resulting interference pattern resembles the one obtained in the Mach-Zehnder setup, where the object beam interferes with the plane wave. Thus, standard phase retrieval algorithms can be used. The main advantage of this setup is its compactness and relatively high immunity to environmental disturbances. However, in this setup it is relatively difficult to obtain plane wavefront in the reference arm which may complicate the processing of the data and limit the accuracy. Also, it is difficult to modify the frequency of the carrier fringes, as it depends only on the parameters of the diffraction grating.

The other, less popular alternative, is ODT based on the pseudo-shearing interferometry [39], presented in Fig. 2.2(c). In this type of tomography, similarly to the common-path setup, the object field is divided into two beams after passing through the specimen. However, in this configuration the object field is divided equally by a beam splitter. The two beams are reflected by reference mirrors and interfere at the detector plane. The reference beam is tilted by a mirror in such a way that only the part of this beam which is not perturbed by the sample interferes with the object beam. The main disadvantage of this setup is the fact that it is applicable to analysis of samples which cover only a small part of the field of view. Without doubts, the advantage of this method is a very simple optical system design.

2.2.2 Born and Rytov approximations

From the mathematical point of view, investigation of samples with ODT belongs to the class of inverse problems [49]. This means that only external data (object projections captured by the camera) and the measurement system (ODT optical setup) are known, and the input data (object function of an analyzed specimen) has to be retrieved. In order to successfully retrieve an object function, dedicated numerical procedures have been developed. In this section, a brief description of the basis of these procedures is presented. This description is provided as an introduction to the limited angle ODT, which is the primary approach used in this Thesis, and which is described in further sections.

In the case of Computed Tomography, a straight line approximation can be adopted, which states that the rays of incident electromagnetic radiation propagate in straight lines through the sample [50]. When this approach is followed, the radiation is treated mainly as a stream

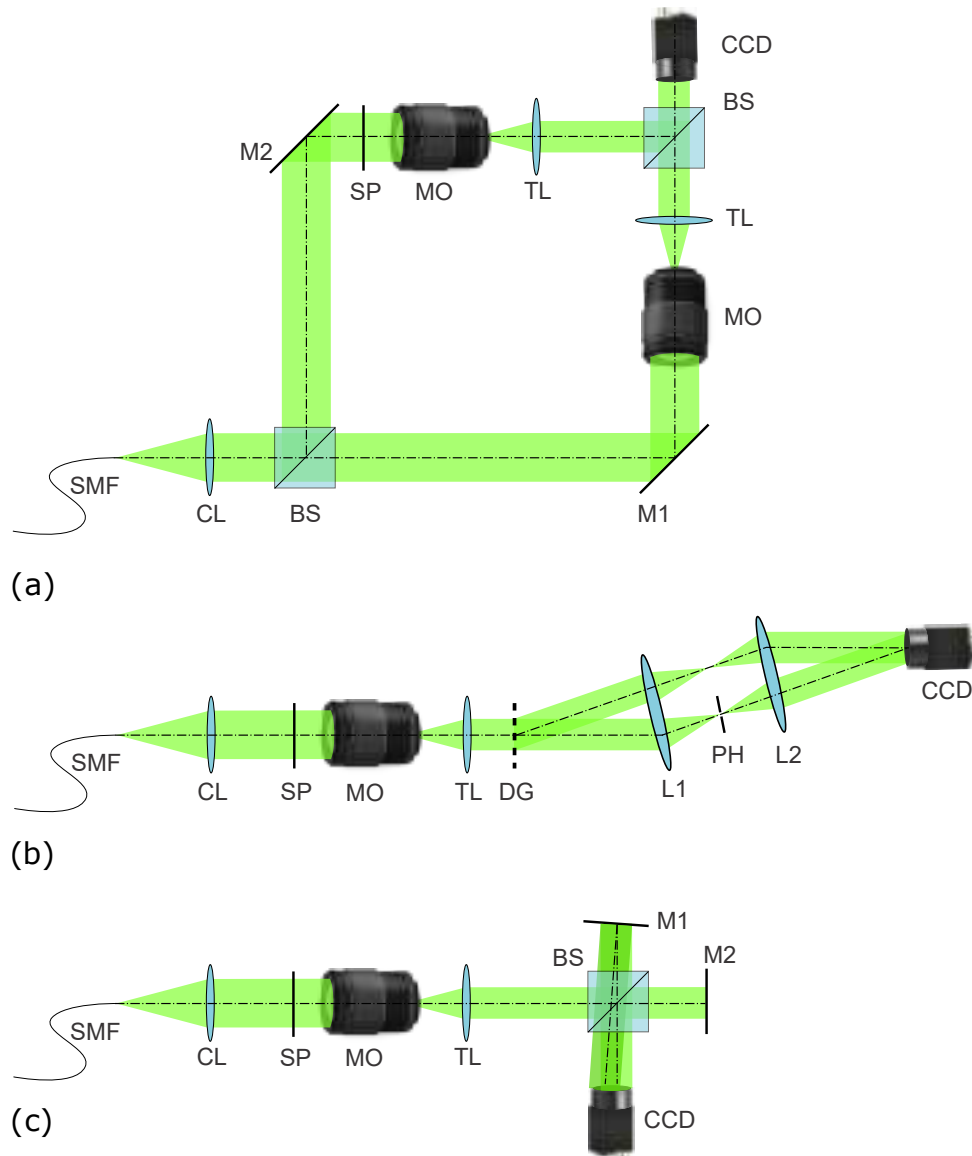


Figure 2.2: Schematic drawings of the three popular setups used in ODT: (a) Mach-Zehnder, (b) pseudo-shearing and (c) common-path setups. SMF - single mode fiber; CL - collimating lens; BS - beam splitter; M1,M2 - mirrors; L1,L2 - lenses; SP - sample plane; MO - microscope objective; TL - tube lens; DG - diffraction grating; PH - pinhole; CCD - charged-coupled device.

of particles and no light diffraction is taken into account. This approximation significantly simplifies tomographic reconstruction procedures. However, it can be applied only to radiation of very short wavelength; in practice, mainly to x-rays. In the case of ODT, such approximation cannot be employed, as there is a significant part of light that diffracts when it propagates through an investigated object. Thus, a more general model of light propagation has to be used if high resolution quantitative tomographic reconstructions are to be calculated. Here, the mathematical description of ODT will be presented based on [43, 51–55].

Every monochromatic wave propagating through a measurement volume with no biological sample inserted has to obey the homogeneous Helmholtz equation:

$$(\nabla^2 + k_m^2)u(\vec{r}) = 0 \quad (2.2)$$

where k_m is the wavenumber in the medium in which the wave propagates:

$$k_m = \frac{2\pi n_m}{\lambda} \quad (2.3)$$

where n_m is the complex refractive index of the immersion liquid and λ is the wavelength of the utilized laser light in vacuum.

When the same wave propagates through some scattering medium, like a biological specimen, a more general version of Eq. 2.2 is necessary. Thus, the wavenumber k_m is replaced with k described as:

$$k(\vec{r}) = k_m \left(1 + \frac{n_\sigma(\vec{r})}{n_m}\right) \quad (2.4)$$

where $n_\sigma(\vec{r})$ is the local deviation of the refractive index of the propagation medium from n_m and is associated with the presence of the investigated sample in the measurement volume of the ODT.

When the wavenumber from Eq. 2.4 is introduced into Eq. 2.2, the inhomogeneous version of the Helmholtz equation is obtained:

$$(\nabla^2 + k_m^2)u(\vec{r}) = -f(\vec{r})u(\vec{r})$$

with

$$(2.5)$$

$$f(\vec{r}) = k_m^2 \left[\left(\frac{n(\vec{r})}{n_m} \right)^2 - 1 \right]$$

where $f(\vec{r})$ is the scattering potential (also called the "object function" [43]) which describes the inhomogeneity associated with the presence of an investigated bio-sample and $n(\vec{r})$ is the absolute refractive index of the investigated sample: $n(\vec{r}) = n_m + n_\sigma(\vec{r})$.

We can represent the total field $u(\vec{r})$ from Eq. 2.5 as the sum of two components:

$$u(\vec{r}) = u_0(\vec{r}) + u_s(\vec{r}) \quad (2.6)$$

where $u_0(\vec{r})$ is the incident field which propagates in free space unperturbed - it is the solution to the homogeneous Helmholtz equation (Eq. 2.2). The component $u_s(\vec{r})$ is the scattered field, exclusively associated with the scattering potential $f(\vec{r})$. In order to retrieve the information about the refractive index distribution inside the analyzed specimen, $u_s(\vec{r})$ has to be calculated. When the total field in the form presented in Eq. 2.6 is substituted to Eq. 2.5, and when the fact that the incident field $u_0(\vec{r})$ must obey the homogeneous Helmholtz equation (Eq. 2.2) is taken into account, the inhomogeneous Helmholtz equation can be written as:

$$(\nabla^2 + k_m^2)u_s(\vec{r}) = -f(\vec{r})u(\vec{r}) \quad (2.7)$$

By employing the Green's function, the solution to Eq. 2.7 can be written as:

$$u_s(\vec{r}) = \int G(|\vec{r} - \vec{r}'|)f(\vec{r}')u(\vec{r}')d^3\vec{r}' \quad (2.8)$$

Unfortunately, the equation 2.8 cannot be solved analytically for the $u_s(\vec{r})$, as the total field $u(\vec{r})$ in the integrand depends on the scattered field $u_s(\vec{r})$ itself, according to Eq. 2.6. There are, however, approximations that can be adopted when specific conditions are met. These approximations linearize the relationship between the two-dimensional scattered field $u_s(\vec{r})$ and a three-dimensional scattering potential $f(\vec{r})$ of an investigated sample. The two methods, called first order Born and Rytov approximations, are the basis of modern optical diffraction tomography and are obligatory to use if high resolution results are to be obtained.

Born approximation

The first order Born approximation assumes that $u_s(\vec{r})$ is small compared to $u_0(\vec{r})$. Under this assumption, the total field $u(\vec{r})$ in the Eq. 2.8, can be substituted with the incident field $u_0(\vec{r})$, resulting in Eq. 2.9, which now can be solved.

$$u_s(\vec{r}) \approx u_b(\vec{r}) = \int G(|\vec{r} - \vec{r}'|)f(\vec{r}')u_0(\vec{r}')d^3\vec{r}' \quad (2.9)$$

This approximation is valid only when the phase difference between the scattered and incident fields is much smaller than π radians [52] (although some sources mention $\pi/2$ [43] and 2π [51]). To analyze the applicability of the 1st order Born approximation, one can calculate the phase delay introduced by a typical biological cell of thickness $d = 10\mu m$, with the refractive index difference Δn between the cell and the surrounding medium equal to 0.04 and a wavelength of light $\lambda = 632.8nm$. The phase difference is then equal to:

$$\Delta\phi = k \cdot \text{OPD} = \frac{2\pi}{\lambda}d\Delta n \approx 4[\text{rad}] \quad (2.10)$$

where OPD is the optical path difference.

Clearly, the 1st order Born approximation is not applicable to analysis of biological specimens, as the maximum phase delay constraint is violated.

Rytov approximation

In order to describe the second approximation, called the 1st order Rytov approximation, the total field $u(\vec{r})$ is rewritten into the form:

$$u(\vec{r}) = \exp(\Psi(\vec{r})) \quad (2.11)$$

where Ψ is the complex phase function. When the total field $u(\vec{r})$ in Eq. 2.5 is substituted with the complex phase form, it gives:

$$(\nabla^2 + k_0^2)u_0(\vec{r})\Psi(\vec{r}) = -[(\nabla\Psi(\vec{r}))^2 + f(\vec{r})]u_0(\vec{r}) \quad (2.12)$$

Since the above equation is just another form of Eq. 2.5, it cannot be solved directly. However, the Rytov approximation assumes that the term $(\nabla\Psi(\vec{r}))^2 = 0$. Also, by analogy to Eq. 2.6, the complex phase of the total field can be represented as the sum of the complex phase $\Psi_0(\vec{r})$ associated with the incident field, and $\Psi_s(\vec{r})$ associated with the scattered field:

$$\Psi(\vec{r}) = \Psi_0(\vec{r}) + \Psi_s(\vec{r}) \quad (2.13)$$

It should be noted that the complex field $\Psi_s(\vec{r})$, often called the Rytov field, can be expressed as:

$$\Psi_s(\vec{r}) = \ln\left(\frac{u(\vec{r})}{u_0(\vec{r})}\right) \quad (2.14)$$

The above formulas and approximations simplify the Eq. 2.12 into the form which now can be solved for the $\Psi_s(\vec{r})$. The solution is presented in Eq. 2.15:

$$\Psi_s(\vec{r}) = \frac{1}{u_0(\vec{r})} \int G(|\vec{r} - \vec{r}'|) f(\vec{r}') u_0(\vec{r}') d^3 \vec{r}' \quad (2.15)$$

When one compares the Eq. 2.15 with Eq. 2.9, a clear relation is visible:

$$\Psi_s(\vec{r}) = \frac{u_b(\vec{r})}{u_0(\vec{r})} \quad (2.16)$$

The Rytov approximation can be successfully performed when the gradient of the complex phase is small. Since the complex phase gradient does not depend on the thickness of an analyzed sample, the Rytov approximation is object-size-independent (in contrast to the Born approximation).

It is important to note that to calculate the scattered field $u_s(\vec{r})$ (in the Born approximation) or complex phase $\Psi_s(\vec{r})$ (in the Rytov approximation), the $u_0(\vec{r})$ field has to be measured. This

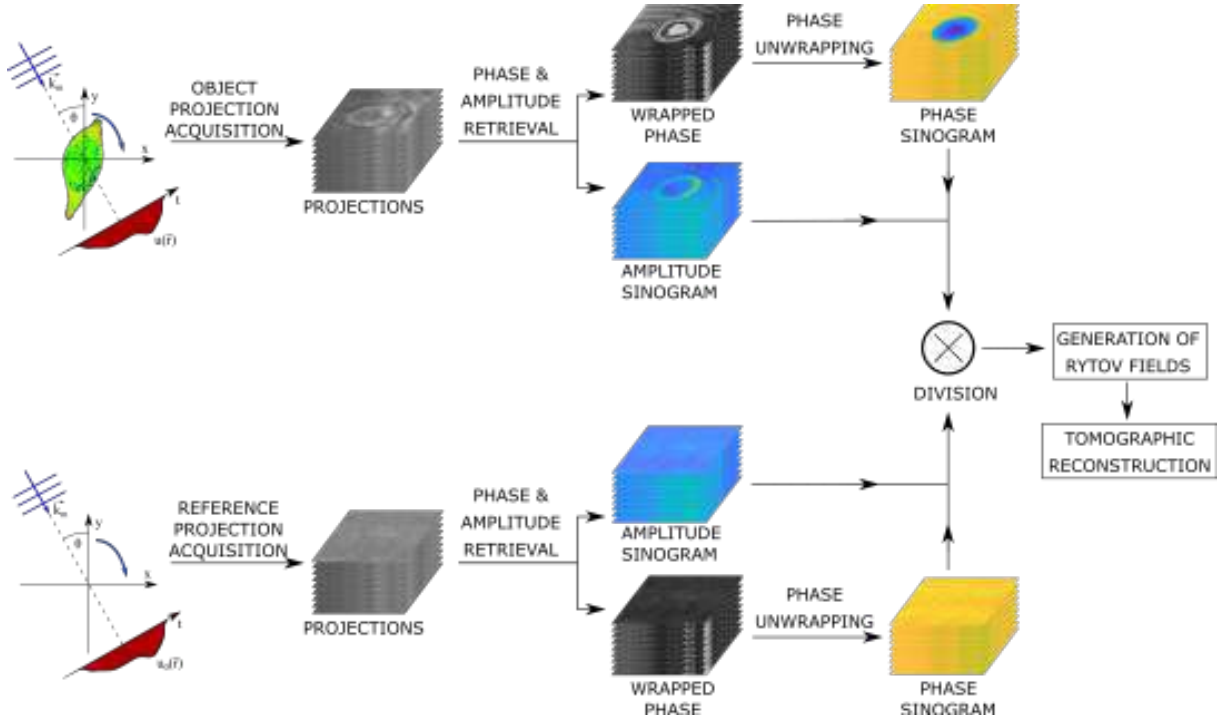


Figure 2.3: Full data processing chain in ODT under Rytov approximation.

is realized by capturing the projections of the measurement volume with no object present - so called reference projections.

Both approximations described above are the first order ones which relates to the fact that it is assumed that each point of the analyzed sample is a source of a scattered wave which then propagates unperturbed to the detector. In other words, no higher order scattering is assumed. Intuitively, it is thus clear that the Born and Rytov approximations are applicable only when analysis of weakly scattering samples is carried out.

Since the procedures described in this Thesis are dedicated to the analysis of biological micro-samples which have relatively small gradients of the refractive index, from now on only the Rytov approximation will be used. The summary of the data processing chain under the Rytov approximation is presented in Fig. 2.3.

2.2.3 Fourier Diffraction Theorem

The Rytov approximation described in the previous section allow us to calculate the complex phase $\Psi_s(\vec{r})$ from each of the object projections captured by the detector. Now, to calculate the 3D refractive index distribution of an analyzed sample from these fields, the Fourier Diffraction Theorem (FDT) can be used [52]. When a specimen is illuminated by a plane wave, FDT relates the 2D Fourier transform of the complex phase $\Psi_s(\vec{r})$ with a spherical surface (called the Ewald's sphere) in the 3D Fourier transform of the scattering potential of the analyzed sample, as shown in Eq. 2.17 (for the sake of simplicity, 2D tomography has been shown).

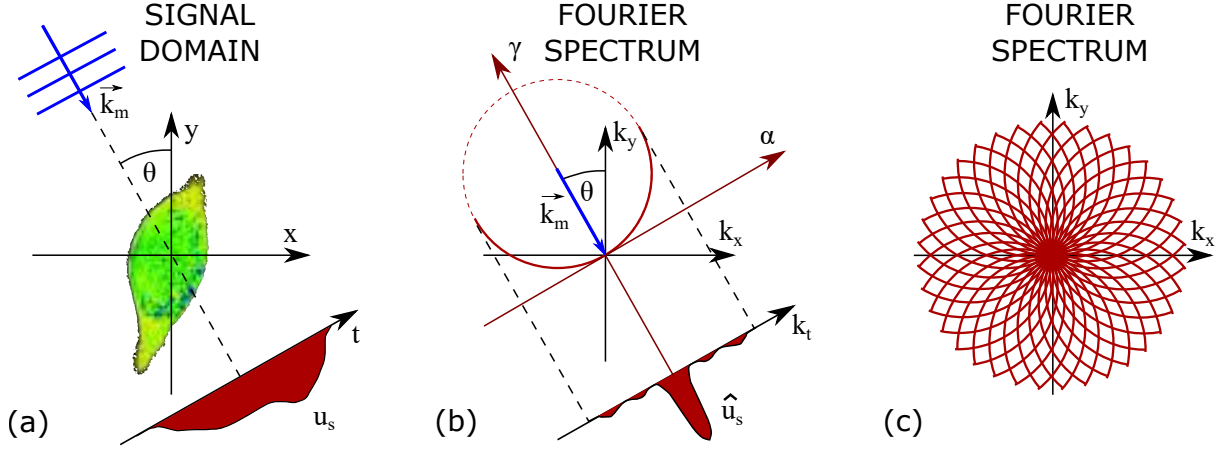


Figure 2.4: Visualization of the Fourier Diffraction Theorem for ODT with object rotation configuration: (a) projection acquisition step; (b) 2D Fourier spectrum filled with data from 1 projection; (c) 2D Fourier spectrum filled with a set of 36 projections captured within a 360° angular range. The red arc in the Fourier spectrum corresponds to the Fourier transform of the complex phase u_s . \vec{k}_m - wave vector representing a plane wave; u_s - scattered field; \hat{u}_s - Fourier transform of the scattered field. Note that the field \hat{u}_s should be divided by a constant factor before being written onto the Ewald's sphere, according to Eq. 2.17.

$$\hat{\Psi}_s(\alpha, l_0) = \frac{j}{2\sqrt{k_m^2 - \alpha^2}} \exp(jl_0 \sqrt{k_m^2 - \alpha^2}) \hat{f}(\alpha, \sqrt{k_m^2 - \alpha^2} - k_m) \quad (2.17)$$

for $|\alpha| < k_m$

where $\hat{\Psi}_s$ and \hat{f} are Fourier transforms of Ψ_s and f , respectively; l_0 is the distance of the detector from the center of the (x, y) coordinate system. It should be noted that most realizations of ODT consist of an optical imaging setup which conjugates the detector plane with the center of an analyzed sample, in which case $l_0 = 0$, and so the above equation can be simplified to:

$$\hat{\Psi}_s(\alpha) = \frac{j}{2\sqrt{k_m^2 - \alpha^2}} \hat{f}(\alpha, \sqrt{k_m^2 - \alpha^2} - k_m) \quad (2.18)$$

for $|\alpha| < k_m$

The theorem is schematically presented in Fig. 2.4. The visualization relates to 2D ODT with object rotation configuration, where the incident field always propagates perpendicular to the surface of the detector. When the analyzed object is rotated and consecutive projections are captured, the Fourier spectrum is filled with Fourier transforms of the scattered fields that are cast onto rotated arcs. When more projections are acquired, the spectrum becomes filled to a greater extent. The result of filling the spectrum with data from projections acquired within 360° angular range (from $\theta = 0^\circ$ to $\theta = 360^\circ$) is presented in Fig. 2.4(c). When all projections are processed, the spectrum is inverse Fourier-transformed, and the scattering potential of the

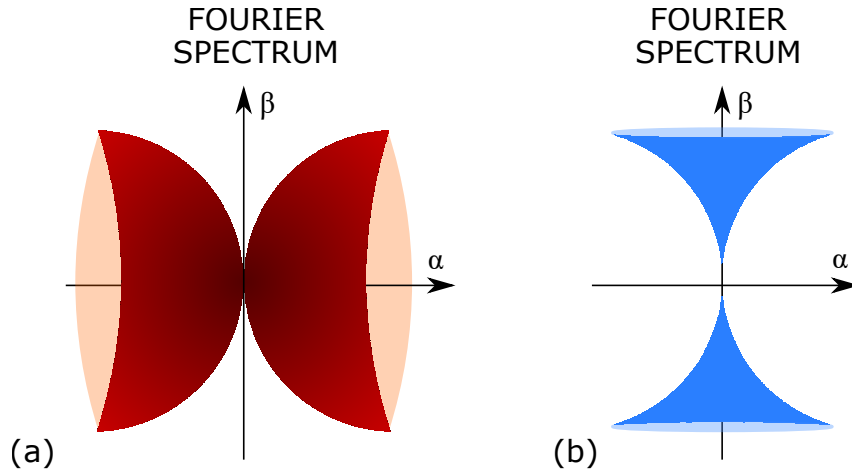


Figure 2.5: (a) Visualization of a 3D spectrum fully filled with Fourier transforms of projections in the case of ODT with object rotation configuration (only 2 opposite Ewald spheres visible); (b) presentation of an empty region in the spectrum which takes the shape of an apple core.

sample is reconstructed. The described procedure is the basic tomographic reconstruction algorithm called Direct Inversion. By analyzing Fig. 2.4, one can immediately notice that ODT offers significantly increased Fourier spectrum coverage compared to DHM, in which only 1 object projection is acquired and thus only 1 Ewald sphere is filled with data.

The procedure described above refers to 2D tomography. However, it can be easily generalized to the 3D case, where each complex phase is a 2D field and its Fourier transform is cast onto the 3D spherical cap [31, 43]. The 3D version of Fig. 2.4(c) is presented in Fig.2.5(a).

As shown in Fig. 2.4, the radius of the Ewald's sphere is equal to the wavenumber k_m . This relation has very profound consequences. As the wavenumber is inversely proportional to the wavelength λ , the Ewald's sphere becomes larger when the wavelength decreases, and, consequently, the arc flattens. When the wavelength is sufficiently small, like, for example, in the case of x-ray radiation ($\lambda \approx 1nm$), the arc can be approximated with a straight line without a significant loss of accuracy. Thus, in the regime of short wavelengths, the FDT transforms into Projection Slice Theorem, which is widely used in Computed Tomography under the name of Filtered Backprojection, for the calculation of tomographic reconstructions [50].

2.3 Limited-angle optical diffraction tomography

A subcategory of the ODT is the limited-angle ODT (LAODT), where the sample and the detector are stationary and the laser beam is rotated to illuminate the investigated object at various angles. The building blocks of LAODT are shown in Fig. 2.6.

This configuration has three main advantages. Firstly, it guarantees that the analyzed bio-sample will not be perturbed during the measurement process in contrast to ODT with object

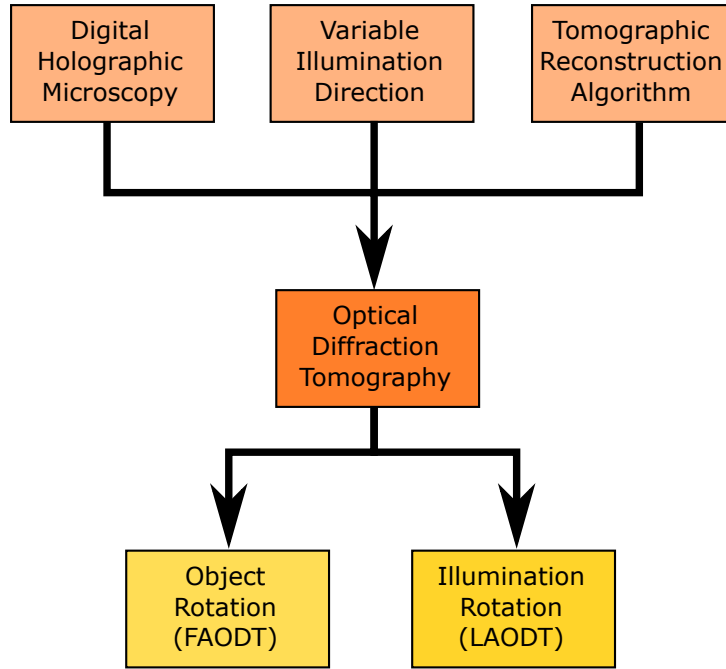


Figure 2.6: LAODT building blocks.

rotation configuration where the rotation of the biological specimen may result in its displacement, and in consequence, in spoiled reconstructions (the acquired projections are no longer consistent with each other). Thus, LAODT is more suitable for analysis of biological objects. Secondly, if LAODT setup is built in vertical configuration, it is perfectly feasible to measure cells directly from the Petri dish in which they were cultured, instead of utilizing the glass capillary which is the source of serious aberrations in the optical system [38]. This property is especially important as the vast majority of in-vitro research is conducted with cultured cells. The last advantage is the fact that controlled rotation of illumination can be realized significantly faster than sample rotation. This allows to investigate dynamic processes in biological micro-objects.

Basically, the principle modules of the data processing chain in LAODT are the same as in ODT. First, the holographic projections of an investigated sample are captured by the CCD detector. To carry out the measurement in accordance with the Rytov approximation, the investigated specimen is then removed from the measurement volume and reference projections are acquired. The reference data is captured in exactly the same way as the object projections, so that at the end each object projection is accompanied by a reference projection. This concludes the data acquisition stage. The process of acquiring two object projections in LAODT is schematically presented in Fig. 2.7

Next, the retrieval of the phase and amplitude is carried out, followed by the phase unwrapping procedure. This step is necessary, as the modulus and phase of the complex phase $\Psi_s(\vec{r})$ (which has to be calculated according to FDT and Rytov approximation) calculated from

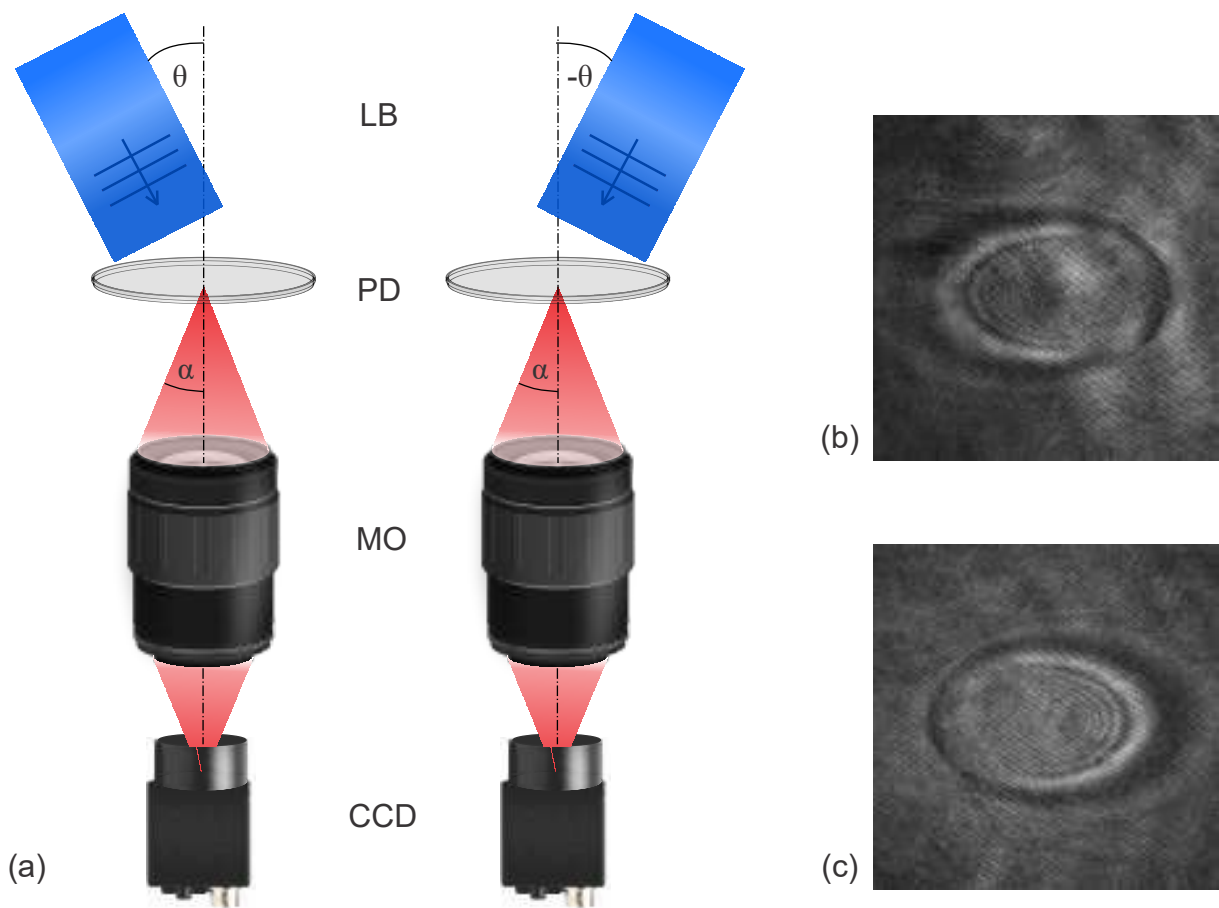


Figure 2.7: LAODT setup in vertical configuration which enables investigation of biological cells directly from Petri dishes. (a) Acquisition of two projections with different illumination directions, and (b,c) two captured projections. LB - laser beam illuminating an investigated sample with a plane wave, PD - Petri dish in the object space, MO - microscope objective, CCD - detector, α - numerical aperture angle.

a complex field with wrapped phase would have discontinuities which spoil the spectrum of the scattering potential. Since the objects under study are biological micro-samples, the projections stored in the sinograms have to be transformed into Rytov fields, according to the Rytov approximation described in Section 2.2.2. Such fields are passed as the input data to a dedicated tomographic reconstruction algorithm to form the 3D refractive index distribution of the specimen.

2.3.1 Illumination rotation

For LAODT, the same configurations of optical setups can be used as for ODT. Regardless of the type of the optical system used for the projection acquisition in LAODT, there is a need to rotate the light beam, so that projections of an investigated sample can be captured for different illumination angles. In the literature, three main methods have been proposed for this purpose [56, 57].

The first idea incorporates galvanometer mirrors (GM) in the optical system [43, 58–60]. Originally, GM were devices with a mirror that rotated when electric current has been detected in the circuit. In optical systems, these instruments are now used for precise tilting of the mirror with a controlled electric current. The main advantage of the GM is the high frequency of operation, usually in the range of several kHz. A single GM can rotate around 1 axis, thus a set of 2 GM is used in LAODT setups to freely deflect the laser beam. The simple operating principle is a significant advantage of the GM. It's biggest disadvantage is associated with the fact that its surface should be conjugate to a sample, which cannot be directly realized when 2 mirrors are incorporated into LAODT setup.

The second concept introduces a digital micromirror device (DMD) into the LAODT setup [61]. DMD is an array of several hundred thousand mirrors, where the size of a single mirror is in the range of several micrometers. Each mirror is controlled with electric current and can be tilted independently. However, most devices allow only for binary tilting, which means that the mirror may be positioned in one of the two possible states: parallel or tilted with respect to the DMD substrate surface. Thus, in order to deflect the laser beam, a binary Lee-type hologram [62], playing the role of an active diffraction grating, is formed by the mirrors. When the laser beam is reflected from the DMD, it is diffracted into several diffraction orders. A single diffraction order is then selected as an object illumination beam. By changing the parameters of the grating, deflection of the object beam can be controlled. One of the main advantages of the DMD-based LAODT setups is extremely high frequency of operation (tens of kHz) and relatively low price. The main disadvantage is low diffraction efficiency of the displayed Lee holograms which leads to loss of the laser beam power. Also, a standard DMD has a fill factor of around 90% [63], which has a negative impact on the quality of the displayed hologram and further deteriorates the parameters of the output beam.

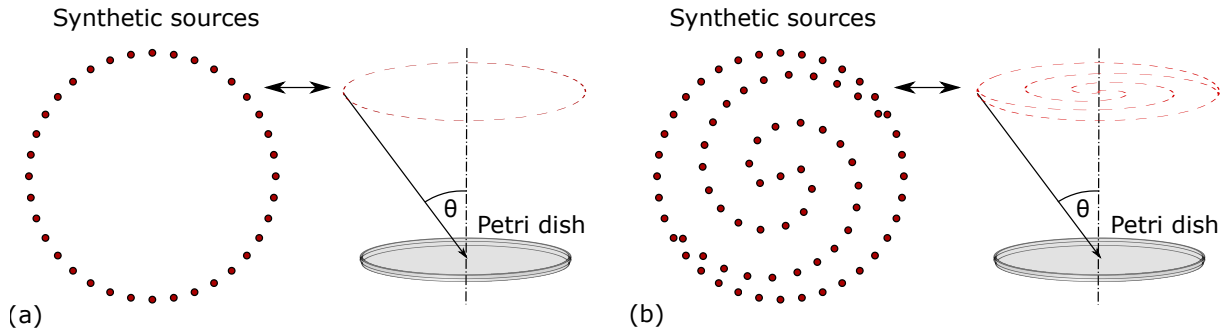


Figure 2.8: Two illumination scanning scenarios: (a) conical, where the laser beam follows a circular pattern and (b) spiral, where the laser beam follows a double spiral pattern.

The last method for rotating the illumination beam is utilization of a phase-only reflective spatial light modulator (SLM) [64]. The main component of this SLM is a high-resolution liquid crystal on silicon (LCoS) microdisplay. This computer-controlled display can change the phase of the incoming light. When a blazed phase grating is displayed on the SLM, the light that is reflected from its surface is diffracted into a single diffraction order. By changing the parameters of this grating, the angle of the laser beam reflection can be controlled. The SLM has a relatively low operating frequency (around 60Hz) and a fill factor similar to that of the DMD. However, in contrast to the DMD, each pixel of the SLM is addressed with a 8-bit signal, which means that each pixel can display 256 gray levels. This versatility allows to optimize the parameters of the output beam in terms of diffraction efficiency and the quality of the wavefront. Additionally, SLM can be used for compensation of some aberrations in the illuminating beam [64]. However, the high price of the SLM limits its wide application.

Regardless of the method used to rotate the laser beam, the sample has to be illuminated from different directions and projections have to be captured by the detector. The exact distribution and number of illumination directions differs depending on the adopted measurement method. However, two most popular illumination scenarios include conical and spiral illumination [42, 61, 64, 65], both presented in Fig. 2.8.

2.3.2 Limitation of LAODT

The visualization of FDT, presented in Section 2.2.3, refers to ODT with object rotation configuration. In LAODT the object and the detector are stationary, and the illumination is rotating. This means that in most cases the incident wave will not fall on the detector perpendicular to its surface, but rather will be inclined. Thus, the Fourier spectrum will be filled in a different way, as shown in Fig. 2.9. Here, the Fourier transform is again cast onto the arc in the Fourier spectrum. However, consecutive projections result in shifted, not rotated, arcs being filled with data. As before, 2D tomography is presented, although this concept can easily be employed for 3D tomography.

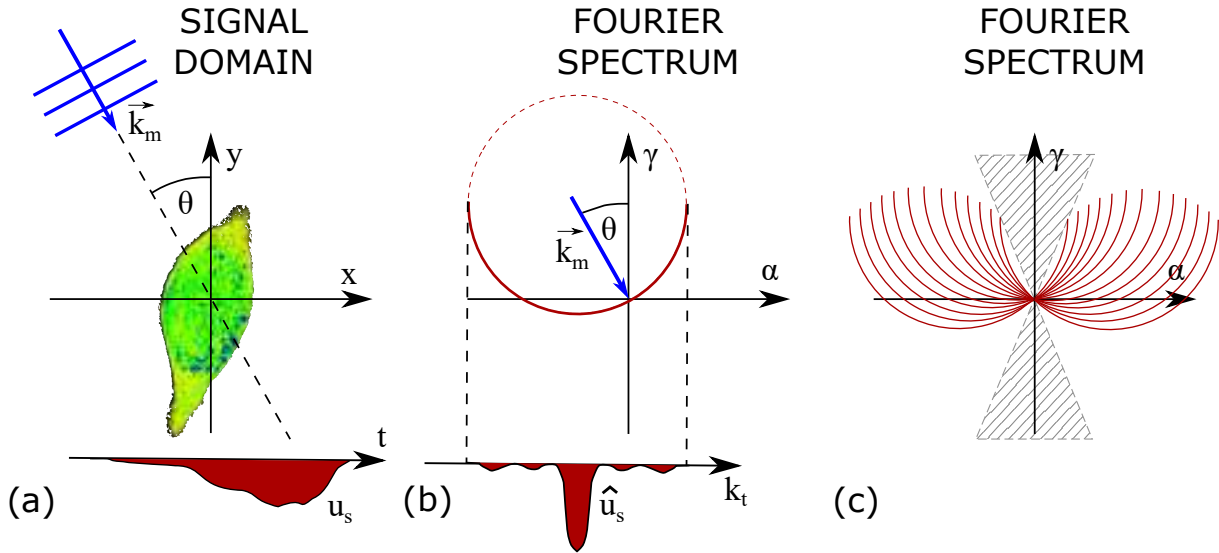


Figure 2.9: Visualization of the FDT for LAODT. (a) Projection acquisition configuration; (b) corresponding arc in the Fourier spectrum of the object's scattering potential; (c) example of a spectrum filled with data from multiple projections (the gray sector represents an empty region in the spectrum).

Unfortunately, despite indisputable advantages, the principle of operation of LAODT is a source of its biggest drawback. Due to the fact that the detector is stationary during the measurement process and the illumination is rotating, there is a limited angular range of illumination directions within which the projections can be acquired. This is caused by the limited numerical aperture of the microscope objective in the imaging system. When looking at Fig. 2.7 it is clear that if the illumination angle θ was to be increased, the light would not propagate through the optical setup to the detector. As a consequence, when all projections are captured by the LAODT setup and the spectrum of the reconstruction is filled with their Fourier transforms according to FDT, still a relatively big area of the spectrum remains empty. As presented in Fig. 2.9(c), in the cone around γ axis, no information about spatial frequencies is provided. Thus, in LAODT it is not possible to fill the spectrum completely like in ODT (compare Fig. 2.4(c) with 2.9(c)). This inherent property of LAODT results in highly distorted tomographic reconstructions of analyzed samples when simple reconstruction procedures, like Direct Inversion, are used. The effect of a partial lack of information in the spectrum on the reconstruction is shown in Fig. 2.10. By analyzing this image, two main errors can be distinguished in the LAODT reconstruction:

- the refractive index value in the case of LAODT is, by average, lower than in the case of ODT;
- the external geometry and the geometry of internal structures is distorted, "blurred" and thus it is difficult to recognize these structures on the reconstruction.

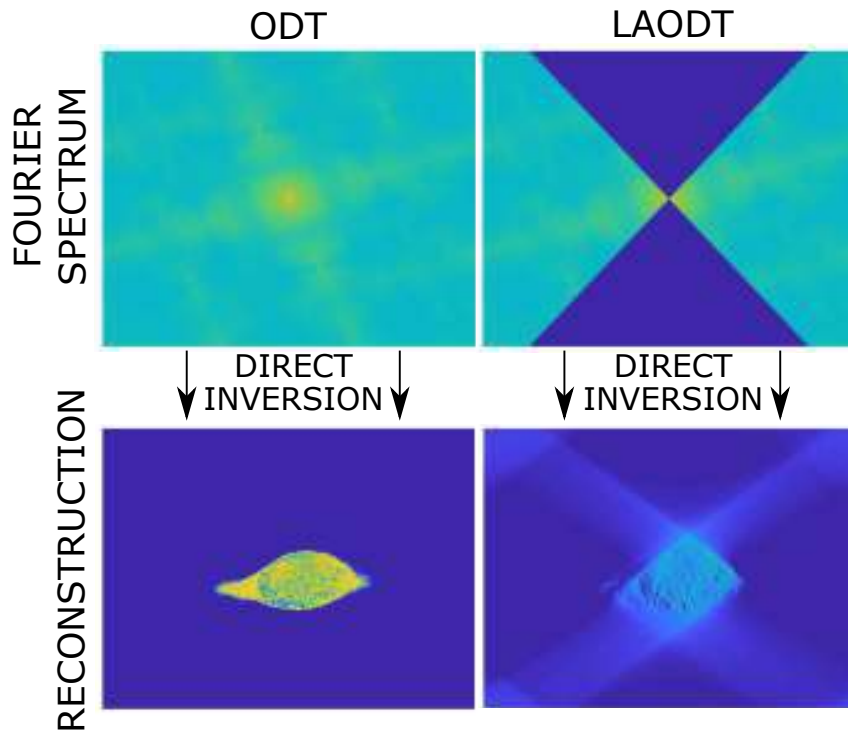


Figure 2.10: Visualization of the effect of the empty region in the Fourier domain on the tomographic reconstruction of a biological cell, calculated with the Direct Inversion method. The reconstructions share a common color scale.

Without doubt, LAODT has strong advantages over the standard ODT techniques. However, the reconstruction errors, that are present when standard ODT reconstruction procedures are applied to LAODT data, undermine the quantitative nature of the measurements carried out with LAODT as the correlation between the reconstructed refractive index and the true refractive index distribution of an analyzed sample becomes loose. Therefore, in order for the LAODT to become a usable and precise technique for investigation of biological specimens, it is crucial that dedicated reconstruction methods are developed, which take the empty region in the Fourier domain into account and iteratively fill it with data based on *a priori* information.

2.3.3 Reconstruction algorithms in LAODT

As it has been proved in the previous section, LAODT requires dedicated tomographic reconstruction procedures in order to limit the distortion of the reconstructed refractive index distribution of an investigated sample. In recent years, a few of such techniques have been proposed. One feature that is common for all of these algorithms is their iterative nature. Unlike the well known Filtered Backprojection [50] or Direct Inversion [66] algorithms which are single step methods (which means that after only 1 step the final reconstruction is obtained), the iterative algorithms require a step which is repeated multiple times: during this process the calculated reconstruction is converging towards its final form.

One group of such methods are algebraic algorithms, like Algebraic Reconstruction Technique [67], Simultaneous Algebraic Reconstruction Technique [68] or Simultaneous Iterative Reconstruction Technique [69]. Here, the reconstruction process consists of solving a set of equations where the voxels of a 3D reconstruction are the unknowns. However, these methods cannot take light diffraction effects into account and so their usefulness in optical tomography without additional regularization is highly limited.

Another group of methods are those that directly make use of the Fourier Diffraction Theorem [43, 70]. In these methods, the Fourier transforms of captured projections are written into an empty spectrum of the investigated object's scattering potential. When the spectrum is filled with all data, the inverse Fourier transform is calculated. In the signal domain, a constraint is employed and the first approximation of the refractive index distribution of the investigated sample is obtained. Next, the Fourier transform of this reconstruction is calculated, and the Fourier transforms of original projections are again written into this spectrum. Now, however, the region that has been empty in the first iteration remains filled. This process is repeated multiple times until the user decides to stop or the algorithm stopping condition has been reached.

The advantage of iterative methods over single step ones is the fact that they can utilize regularization techniques in each iteration. These techniques consist of introducing mathematical constraints (additional boundary conditions) to enable calculating a solution of ill-posed inverse problems. In LAODT, these regularizers make use of *a priori* information to fill the empty space in the Fourier spectrum. The type of this information depends solely on the nature of the analyzed sample. The most basic regularizer is the non-negativity constraint, in which it is assumed that the phase values of the reconstructed sample cannot be lower than the background values (e.g. of an immersion liquid). If the analyzed specimen is optically denser than the surrounding medium, application of this constraint increases the convergence of most iterative algorithms. Also, it improves the quality of a reconstruction, limiting the distortion that is present due to the limited angular range of acquired projections, although the improvement is not significant.

Another type of the *a priori* knowledge that can be employed in the reconstruction process is the information about the point spread function (PSF) of the tomographic optical system. Basically, the image of an object formed by a microscope objective is the convolution of every point of this object with the PSF of the optical system, which carries information about the "blur" that every point will undergo when imaged, according to Eq. 2.19.

$$I(x,y) = O(x,y) \otimes \text{PSF}(x,y) \quad (2.19)$$

where $I(x,y)$ is the object image and $O(x,y)$ is the object function in the object space (for the sake of simplicity, imaging system magnification of 1 has been assumed). The PSF can be used in LAODT algorithms to reverse the above-mentioned blurring which takes place during image formation process. By deconvolving the image with the PSF, a higher resolution image

can be obtained - ideally $O(x,y)$ can be retrieved. One problem with this approach is the fact that it does not limit the LAODT artifacts in the reconstruction that are present due to limited angular range of projections. Thus, it is usually used together with non-negativity constraint [42]. Another disadvantage is the difficulty to experimentally determine the PSF of an optical system. Finally, the quantitative nature of the resulting reconstruction is questionable.

In the last few years, great interest was directed toward tomographic reconstruction methods which utilize compressed sensing (CS) regularization. CS provides tools to retrieve sparse signals from incomplete data. The *a priori* knowledge about the sparse nature of the original signal is a very strong constraint which allows to retrieve this signal with unprecedented effectiveness. Thus, if a tomographic reconstruction in LAODT could be represented in a sparse form, by applying CS techniques one could retrieve the reconstruction without artifacts associated with limited angular range of acquired projections. Unfortunately, mathematical spaces in which most biological specimens could be represented in a sparse form are not known. One of the very few spaces in which a small group of bio-samples is sparse is the gradient of the refractive index [71]. The CS tool which can be applied to this type of objects is Total p-Variation (TpV) minimization, which minimizes the TpV norm of a reconstruction. Basically, the TpV norm is the L_1 norm of the gradient magnitude of the three-dimensional reconstruction f [72], as shown in Eq. 2.20:

$$\|f\|_{TV} = \|(|\nabla f|)\|_1 \quad (2.20)$$

Since the reconstruction f is a scalar matrix, its gradient is defined as:

$$\nabla f = \vec{i} \frac{\partial f}{\partial x} + \vec{j} \frac{\partial f}{\partial y} + \vec{k} \frac{\partial f}{\partial z} \quad (2.21)$$

where $\vec{i}, \vec{j}, \vec{k}$ are directional vectors. The magnitude of this gradient is defined as:

$$|\nabla f| = \sqrt{\left(\frac{\partial f}{\partial x}\right)^2 + \left(\frac{\partial f}{\partial y}\right)^2 + \left(\frac{\partial f}{\partial z}\right)^2} \quad (2.22)$$

Formally, the norm present in Eq. 2.20 should be the L_0 norm, which returns a number of non-zero voxels in the reconstruction. However, minimization of the L_0 norm is a NP hard problem [73] and thus, it is commonly substituted with the L_1 or L_2 norm which are easier to minimize.

In tomography, TpV minimization is applied together with algebraic reconstruction methods, like SART or SIRT [59, 71, 72, 74]. The problem can be stated as follows:

$$\begin{aligned} & \underset{\vec{f}}{\text{minimize}} && \|\vec{f}\|_{TV} \\ & \text{subject to} && A\vec{f} = \vec{b} \quad \vec{f}_j \geq 0 \end{aligned} \quad (2.23)$$

where \vec{f} is the reconstruction function f represented in the vector form, where elements of the vector are \vec{f}_j with $j = 1, 2 \dots N$, where N is the total number of voxels in the reconstruction; A is the system matrix which holds information about illumination scenario in the tomographic setup, number of acquired projections and number of detector pixels; \vec{b} is the sinogram with measurement data represented in the vector form, where elements of the vector are \vec{b}_j with $j = 1, 2 \dots M$, where M is the total number of pixels in all acquired projections. Minimization in Eq. 2.23 is constrained with two conditions. The first, $A\vec{f} = \vec{b}$, forces the resulting reconstruction to be consistent with the sinogram. The second, $\vec{f}_j \geq 0$, is the non-negativity condition which uses *a priori* knowledge that phase values in the reconstruction cannot be negative.

Technically, the minimization from Eq. 2.23 can be carried out with various optimization algorithms. One example is the Chambolle-Pock method [75, 76]. It is an iterative algorithm, where the optimization problem is reformulated, according to Eq. 2.24.

$$\underset{\vec{f}}{\text{minimize}} \{ \|A\vec{f} - \vec{b}\|_1 + \lambda \|(|\nabla f|)\|_1 \} \quad (2.24)$$

where λ is a weighting factor. This algorithm minimizes the sum of two functions: $\|A\vec{f} - \vec{b}\|_1$ which is inconsistency of the reconstruction with the measurement data and $\|(|\nabla f|)\|_1$ which is TpV norm of the reconstruction.

As it has been mentioned earlier, algebraic reconstruction methods cannot take light diffraction into account. However, when these methods are combined with the TpV regularization, often high quality reconstructions in LAODT can be obtained [77, 78]. Unfortunately, this approach assumes that the refractive index distribution of the object under study can be described with a piecewise-constant function, which often is not true. This is especially problematic when biological specimens, other than red blood cells (which fulfill this requirement), are investigated. It is thus dedicated mostly to technical samples, like optical fibers.

2.4 Quality assessment criteria

The methods presented in this Thesis are purely quantitative ones. Thus, in order to objectively assess the efficiency and precision of tomographic reconstructions calculated with these methods, two quantitative quality assessment methods are used throughout this Thesis.

The first method is calculation of the well-known root-mean-square error (RMSE) between the reconstructed three-dimensional refractive index distribution and the reference data. RMSE does not prioritize any regions of the reconstructed volume, treating every voxel equally, according to Eq. 2.25.

$$RMSE = \sqrt{\frac{1}{n} \sum_{i=1}^n (y_i - \hat{y}_i)^2} \quad (2.25)$$

Because of the mathematical construction of RMSE, it is possible that a reconstruction of a biological cell will have small error, despite the fact that internal structures of a cell are hardly visible, just because the surrounding of a cell, which carries no useful information, has been reconstructed correctly. Thus, the second quality assessment method has been chosen, which calculates a parameter called 'a universal image quality index' [79], hereinafter referred to as the Q parameter. It utilizes structural similarity, which, effectively, prioritizes regions of a dataset which carry important information. The algorithm processes the analyzed dataset in a way which mimics human perception. Mathematically, Q-parameter is a product of three components, as presented in Eq. (2.26).

$$Q = \frac{\sigma_{ab}}{\sigma_a \sigma_b} \cdot \frac{2\bar{a}\bar{b}}{\bar{a}^2 + \bar{b}^2} \cdot \frac{2\sigma_a \sigma_b}{\sigma_a^2 + \sigma_b^2} \quad (2.26)$$

where \bar{a} and \bar{b} are average values of all pixels in images a and b , respectively; σ_a and σ_b are standard deviations of pixel values in images a and b ; σ_{ab} is the covariance between pixel values in images a and b . According to [79], the three components in Eq. (2.26) are: loss of correlation between images, luminance distortion and contrast distortion. Q-parameter takes values in the range $[-1, 1]$, where 1 means ideal correspondence between the two compared images.

The above-mentioned assessment methods are used in two cases. The first one is when numerical simulations are carried out and the calculated tomographic reconstruction can be compared with the numerical phantom used in the study. The second one is when a known experimental sample, with calibrated geometry and refractive index distribution is investigated and its reconstruction can be compared with its known parameters. However, in the Thesis, multiple experimental samples with unknown geometry and refractive index distribution are analyzed, like biological cells and tissue slices, where there is no possibility to quantitatively determine reconstruction errors, since there is no reference reconstruction. In these cases, the correctness of the calculated reconstruction is extrapolated from the numerical simulations. What is more, qualitative evaluation of these results by experienced medical doctors is performed. This evaluation does not provide information about reconstruction errors. However, it is the first step to validate the proposed methods in an operational environment.

2.5 Conclusions

Certainly, LAODT is a candidate for the comprehensive method for measuring the 3D refractive index distribution of biological micro-samples. Combining the LAODT approach with the FDT and the Rytov approximation creates a firm metrological basis for the retrieval of the scattering potential associated with the specimen. However, limited angular range of acquired projections, inherent in LAODT, leads to the empty space in the reconstruction spectrum, which results in

distorted reconstructions. Without a reconstruction procedure which would minimize this deformation and would be dedicated to biological micro-structures, usability of LAODT is highly limited. Thus, in the next section, a detailed description of such method is presented.

Chapter 3

Total Variation Iterative Constraint

Method

The problems described in previous sections of the Thesis are the motivation for the development of a new tomographic reconstruction procedure. It became apparent that without a procedure dedicated to analysis of biological samples in LAODT, the assessment of the acquired tomographic results is very difficult.

In Section 2.3.3, a procedure called TpV minimization has been introduced. It is a powerful regularization method, which, when combined with algebraic reconstruction algorithms, returns a tomographic reconstruction of the refractive index distribution of an investigated sample. What is important, this reconstruction is almost entirely free of the distortion that is present due to limited angular range of acquired projections. Thus, this technique is the main candidate for the LAODT reconstruction procedure. Unfortunately, it can be used only with samples whose refractive index distribution can be approximated with a piecewise-constant function. This constraint limits its applicability to most technological objects and only a few biological specimens. When this method is used to reconstruct most of biological micro-structures, corrupted reconstructions are obtained. This is due to the fact that TpV minimization forces the refractive index distribution of the reconstruction to become piecewise-constant, regardless of the true nature of this distribution. The effect of application of TpV minimization combined with ART to tomographic projections of a biological cell phantom with smooth refractive index distribution in the cytoplasm region is presented in Fig. 3.1. The phantom is formally presented in Sec. 3.3.1. The projections of the phantom were captured in the limited angular range with the illumination scanning scenario presented in Fig. 2.8(a). When analyzing the cross-sections through the calculated reconstruction, shown in Fig. 3.1(b), it is apparent that the smooth structures in the phantom disappeared. Instead, the piecewise-constant refractive index distribution has been retrieved, which can be recognized by the presence of patches with constant refractive

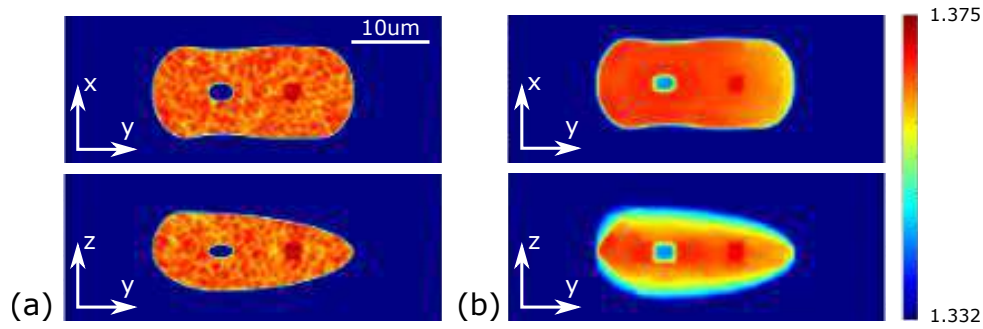


Figure 3.1: Effect of the TpV minimization procedure combined with the ART algorithm applied to tomographic projections of a numerical phantom presented in (a). Two cross-sections through the reconstruction are presented in (b).

index values.

Fig. 3.1 provides 1 additional important information. When the $z - y$ cross-section (z being the optical axis) through the reconstruction is analyzed, one can notice that unlike the internal refractive index distribution, the external geometry has been retrieved with decent accuracy. This is especially clear, when this reconstruction is compared with the one shown in Fig. 2.10. In both cases, originally there has been an empty region in the spectrum of the reconstruction. However, when the TpV minimization procedure has been applied, this empty region became partially filled, which resulted in the correct external geometry reconstruction. To understand this phenomenon, one can notice that a biological cell covers usually only a small part of the measurement volume. Thus, in the extreme case, when TpV procedure is applied, the cell as a whole is approximated as one big 3D patch with a constant refractive index value (being the average value of the refractive index distribution of the whole specimen). This approximation is used in the TpV minimization procedure and this is the reason, why the external geometry is correctly retrieved. This phenomenon led to development of a novel reconstruction approach, which I called the Total Variation Iterative Constraint (TVIC) method and which can be applied to specimens with non-piecewise-constant refractive index distribution [64, 77, 80]. **This method is the main novelty of my Thesis.** In this section, the detailed description of this procedure is provided.

Disclaimer: In order to standardize nomenclature, in the Thesis I abbreviated the name of the tomographic reconstruction strategy from Generalized Total Variation Iterative Constraint (GTVIC - which is how the method is called in some research papers) to Total Variation Iterative Constraint (TVIC).

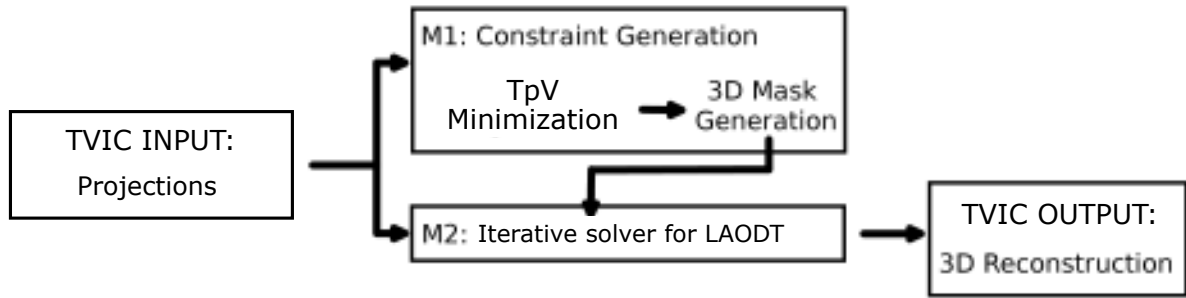


Figure 3.2: TVIC strategy scheme

3.1 General description

The idea behind the TVIC approach is to divide the process of tomographic reconstruction of non-piecewise-constant samples into 2 parts. In the first one, the **external geometry** (information about investigated object’s boundaries), free from the deformation characteristic to LAODT reconstructions, is retrieved. Here, it is assumed that the sample under study is distinguishable from the surrounding medium in terms of the refractive index. This part is carried out according to the TpV minimization procedure described in detail in Section 2.3.3. As a result, a 3D reconstruction of the measured biological micro-sample is obtained, which defines the spatial limits of the specimen - it has, however, erroneous refractive index distribution of internal structures. That is why, it is binarized and a 3D mask is created. In the second part, the **refractive index distribution of internal structures** is reconstructed with an iterative tomographic solver. Figure 3.2 presents the flow diagram of the TVIC strategy. The M1 module, presented in the figure, is constant for all tomography data types. The tomographic solver from M2 module, however, depends on whether the diffraction effects can be neglected (like e.g. in x-ray tomography or optical tomography of extremely thin objects with the detection plane optically coupled with the center of the sample) or not. In the M2 module, no piecewise-constancy of the refractive index is assumed - it is thus perfectly suited for the analysis of non-piecewise-constant specimens. This part is, however, strongly supported with the mask, adaptively optimized during the first stage. This 3D mask is applied in every iteration of the tomographic solver, becoming a support constraint. This allows the algorithm to reconstruct the refractive index distribution of an analyzed sample with the minimized distortion associated with the LAODT. What is more, it enhances the convergence rate of the utilized algorithm. In general, the TVIC procedure is a universal one and can easily be adopted for different tomography setups. It is however, dedicated mainly to the reconstruction of the 3D refractive index distribution of non-piecewise-constant samples.

The second stage is an arbitrary iterative reconstruction procedure. In this Thesis, a Gerchberg-Papoulis (GP) algorithm is used [81]. It is an iterative version of the reconstruction procedure based on FDT, which was described in Section 2.3.3. The core of this algorithm is the iterative

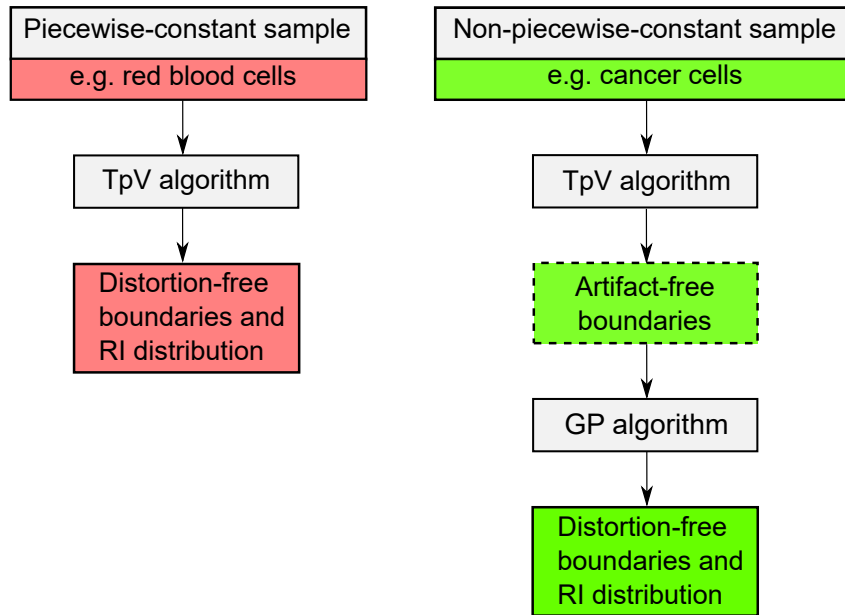


Figure 3.3: Dependence of the reconstruction scheme on investigated object type; TpV - total p-variation algorithm, GP - Gerchberg-Papoulis algorithm. [83]

filling of the reconstruction spectrum with the appropriately prepared Fourier transforms of the acquired projections. These Fourier transforms are cast onto the Ewald's spheres, as shown in Fig. 2.9. What is more, the Rytov approximation has been utilized, as it is coherent with the nature of biological specimens. In each iteration of this algorithm, the mask from the first stage is applied onto the reconstruction. Contrary to the first stage of the method, the number of iterations of this stage is not fixed. The criteria specifying this number are discussed in Section 3.3.1. In the Thesis, the GP algorithm supported with the TVIC strategy will be called TVIC-GP.

It should be noted that the idea behind the TVIC strategy (utilization of a binary mask to support the process of the tomographic reconstruction) is coherent with recent advances in Computed Tomography which uses x-ray radiation for the investigation of samples which are characterized by the piecewise-constant absorption coefficient [82]. In Computed Tomography, however, the diffraction of radiation is ignored and the angular span of projections equals 360° , thus no artifacts associated with a limited angular range of projections are present.

To conclude, depending on the nature of the investigated sample, different reconstruction approach has to be adopted when LAODT is used. If the sample is characterized with the refractive index distribution that can be approximated with a piecewise-constant function, the TpV algorithm may be sufficient to retrieve the distortion-free refractive index distribution. If, however, the sample has a non-piecewise-constant nature, like most biological specimens have, the TVIC procedure should be applied. This has been visualized in Fig. 3.3.

3.2 Reconstruction clearing procedures

One common problem present in most tomographic reconstruction approaches is the presence of unwanted objects in the measurement volume, like dust particles, cellular debris, air bubbles and others. Usually, these inclusions are reconstructed together with the analyzed sample. The presence of these inclusions may result in the partially obscured reconstructed image, which may cause difficulties during e.g. assessment of the parameters of a reconstructed biological cell.

One of the advantages of the TVIC method is the straightforward possibility to introduce procedures for removing the unwanted objects from the reconstructed results. Here, two different methods for removing these structures are presented. In both cases the TVIC procedure is carried out in the same standard way until the piecewise-constant version of the reconstruction is calculated with the TpV minimization method and the 3D mask based on this reconstruction is created. This mask carries information about the distortion-free geometry of the analyzed sample and of the unwanted objects in the measurement volume.

In the first reconstruction clearing procedure, the calculated mask undergoes segmentation. As a result, all objects (both the investigated one and the unwanted inclusions) are identified as separate structures. Thus, now it is a straightforward procedure to remove the information about all structures but the largest one from the mask (it should be emphasized that it is assumed that the sample under study is larger than the inclusions). This modified mask is saved under a different name in the computer memory. Then, the process of the tomographic reconstruction is conducted in a standard way with the iterative solver of choice. In each iteration, the unmodified version of the mask is applied to the reconstruction. However, when the last iteration is finished, the 3D reconstruction is masked with the modified version of the mask. This way, only the investigated sample is left in the 3D reconstruction. The procedure is presented in Fig. 3.4(a).

The second approach is a more complex one: it removes unwanted objects from the reconstruction by clearing the original sinogram. In the first step, the 3D mask calculated with the TpV method is segmented. Then, the investigated object is removed from this reconstruction. This way, only the unwanted structures are left. In the next step, a phase sinogram, based on this reconstruction, is recalculated. This sinogram calculation step mimics the experimental process of acquiring projections of the investigated measurement volume. As a result, the sinogram of the unwanted inclusions is obtained. Finally, this sinogram is subtracted from the original phase sinogram, resulting in a inclusion-free phase sinogram of the analyzed specimen.

There are two remarks that should be made. Firstly, for simplicity, the sinogram recalculation process is performed with the straight line approximation (the inverse of the Filtered Backprojection algorithm), which means that no diffraction is taken into account. Secondly, the amplitude sinogram remains intact, which leads to inconsistency between the phase and

amplitude sinograms. Still, however, the procedure assures that the phase associated with the unwanted inclusions is removed from the original data. This modified sinogram is then passed to the tomographic reconstruction algorithm. This procedure is presented in Fig. 3.4(b).

The advantage of the second approach is the fact that it can be applied to every tomographic reconstruction algorithm as it is independent from the reconstruction content. Thus, when this sinogram clearing procedure is done, the modified sinogram can be saved and passed to any reconstruction technique. Furthermore, it is important to note that when unwanted structures in the reconstruction do not have sharp edges (have blurry structure) it is not possible to correctly perform their segmentation with the first clearing method. As a consequence, when this procedure is used these inclusions are not completely removed. However, in the second method the only structure that is segmented in the clearing process is the investigated object. Whatever is left in the TpV reconstruction after this object is removed will not be present in the final result. Unquestionably, this is a crucial advantage of the second clearing strategy.

There is another reason why the second approach should be used when high accuracy TVIC-GP reconstructions are calculated. In each iteration of TVIC-GP the mask with retrieved geometry of an object is applied in the reconstruction domain. This means that all inclusions are removed from the reconstruction in each iteration (since the mask covers only the investigated sample). At the same time, however, in each iteration these inclusions are again introduced to the reconstruction by replenishing a part of the spectrum with Fourier transforms of original projections where these structures are still present. As an effect, the refractive index values associated with unwanted structures are pushed inside the investigated object, which introduces reconstruction errors. Thus, in order to achieve high quality results, the second clearing strategy, which removes information about the inclusions from the original sinogram, has to be utilized. However, this approach, compared to the first one, is more time-consuming as it requires additional TpV minimization and sinogram recalculation procedures. In this Thesis, the second approach is used.

The numerical verification of both clearing methods is carried out in Section 3.3.5.

3.3 Numerical experiments & quality assessment

In this section, the TVIC-GP procedure is numerically tested. The purpose of these tests is to assess the errors that are present in the reconstructions and that are associated with the principle of operation of TVIC. Also, this section aims to assess the degree to which the reconstruction distortions, that are present due to limited angular range of acquired projections, are minimized. All the test conducted in this section are carried out on numerical phantoms.

First, the numerical phantoms used in the study are presented. The second part of this Section is dedicated to analysis of convergence of the TVIC-GP approach. Then, dependence of

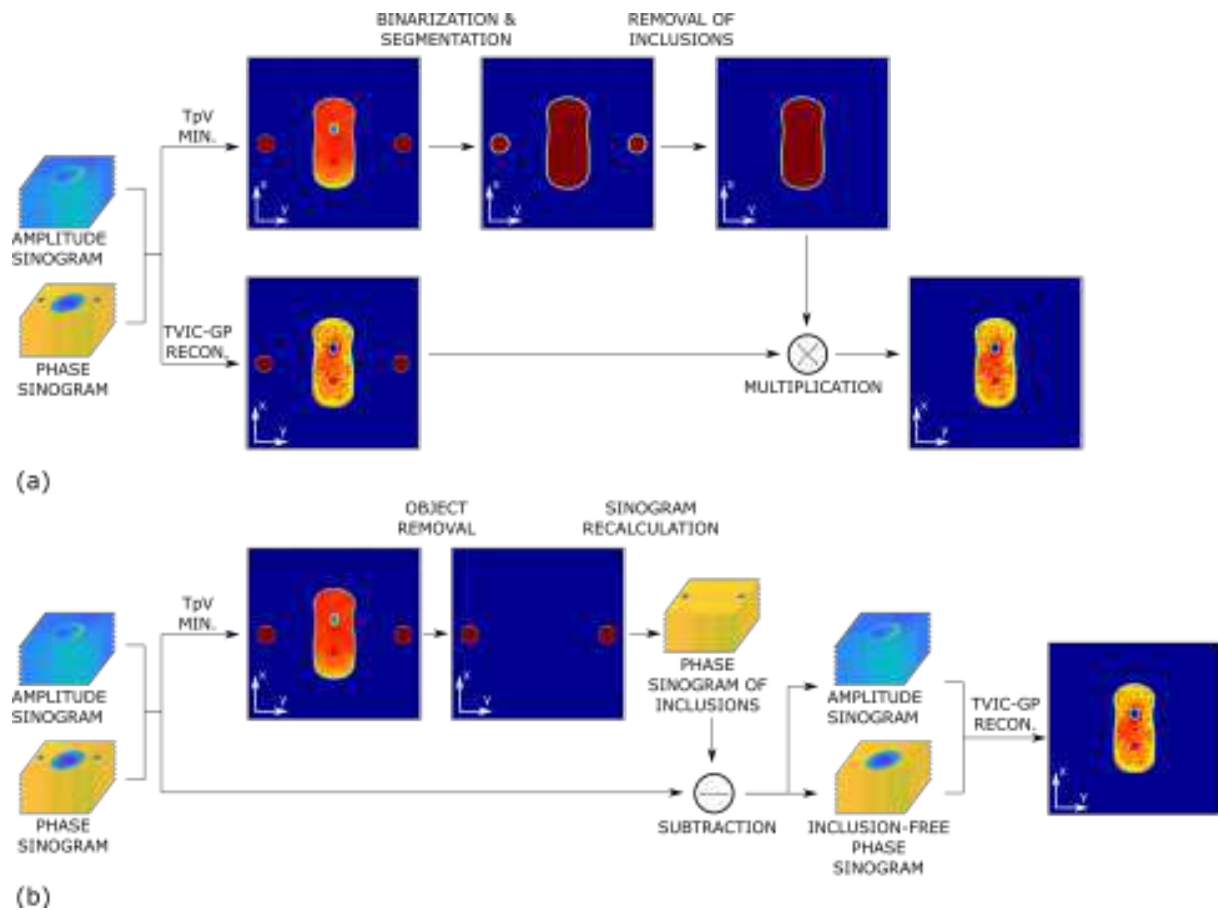


Figure 3.4: Processing schemes for two reconstruction clearing procedures: (a) method of removing structures from the final reconstruction with the modified mask and (b) method of clearing the input sinogram.

the TVIC-GP method on the number of acquired projections is analyzed. Finally, the efficiency of the reconstruction clearing procedures, described in the previous section, is evaluated.

3.3.1 Method

First, the parameters of the TVIC-GP approach have to be specified. The sufficient number of 100 TpV iterations has been determined experimentally as the number that guarantees retrieval of 3D geometry of an investigated biological specimen. Higher number of iterations increases the computational load of the algorithm and does not bring significant improvement (the difference between next consecutive reconstructions is small). At the end of this step, this reconstruction is binarized with a threshold level equal to $0.7h$, where h is the threshold level calculated automatically with Otsu's method [84], resulting in a 3D mask with the retrieved true geometry of the investigated sample. This step is implemented in Matlab environment with the use of ASTRA Tomography Toolbox [85, 86]. The mask is then passed to the second stage (GP algorithm) of the algorithm as a support constraint, where properly reconstructed object boundaries will be filled with correct refractive index values.

For the analysis of the TVIC-GP accuracy and effectiveness, three-dimensional phantom objects have been modeled.

The first numerical phantom is a sphere with the constant refractive index value $n_{HeNe} = 1.4905$ surrounded by the immersion liquid with refractive index value $n_{HeNe} = 1.5173$. Diameter of the sphere equals $10\mu m$. The size of the matrix with the phantom is $500 \times 500 \times 500$ pixels, with the simulated pixel size of $0.24\mu m$. This phantom represents piecewise-constant objects. Despite the fact that the procedures developed in this Thesis are dedicated to biological micro-samples with non-piecewise-constant refractive index distribution, the piecewise-constant sphere is still the perfect testing object, as all the reconstruction artifacts are well noticeable.

Since the TVIC-GP procedure is designed for the reconstruction of biological micro-objects, the second phantom structure was based on the real biological cell. The phantom is presented in Fig. 3.5. This simplified phantom is based on the structure of a Paramecium cell.

The phantom consists of:

- immersion medium surrounding the cell, with constant refractive index value equal to $n_{HeNe} = 1.3317$,
- cytoplasm with refractive index value varying in the range $n_{HeNe} = 1.359 - 1.369$,
- a cell core with refractive index value varying in the range $n_{HeNe} = 1.37 - 1.375$,
- a vacuole with constant refractive index equal to $n_{HeNe} = 1.3317$,

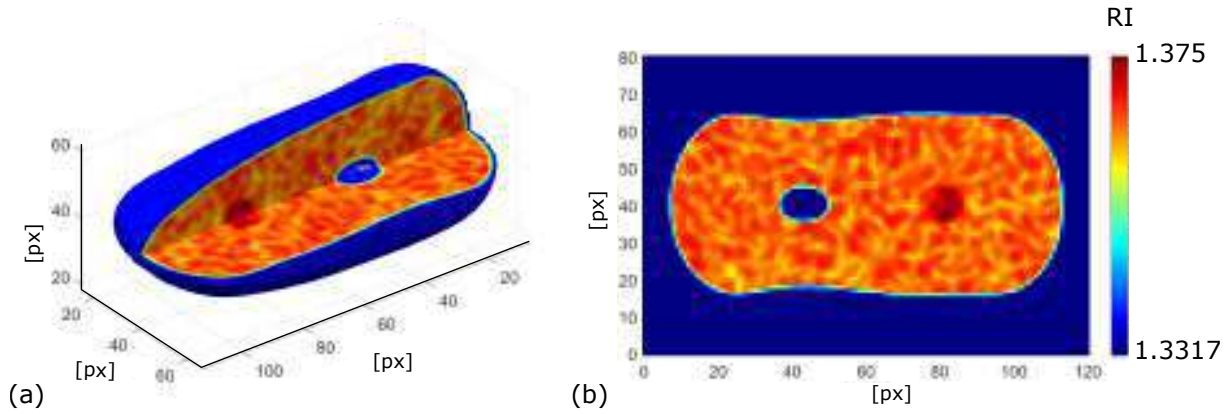


Figure 3.5: Numerical phantom of a biological cell: (a) 3D geometry with a partial cross-section and (b) full cross-section through the center of the phantom.

- a cell wall with a refractive index that smoothly transits from the refractive index of the cytoplasm to the refractive index of the immersion medium.

Since this object should not be piecewise constant, the cytoplasm and nucleus of the phantom were designed to contain smoothly varying, quasi-random refractive index distribution. These structures were designed as a scaled Fourier transform of a zero-padded matrix with pixels with random values. The size of the matrix with the phantom is $500 \times 500 \times 500$ pixels, with the simulated pixel size of $0.24 \mu m$. The size of the phantom itself is approx. $267 \times 125 \times 107$ pixels.

To carry out the simulations, the projections of the phantom objects described above are calculated by conducting the reverse process of FDT: the Fourier transform of the scattering potential of the phantom is calculated and the data lying on the Ewald's sphere is extracted and inverse-Fourier-transformed. By choosing specific Ewald's spheres, different phantom projections can be generated. The orientation of the phantoms with respect to the optical system in this simulation is presented in Fig. 3.6. It should be noted that projections calculated in this way do not take higher order scattering into account which may result in overvalued quality of obtained reconstructions. Still, however, this does not interfere with the possibility of fair assessment of LAODT artifacts.

In the process of generating numerical projections, the LAODT system with the given parameters has been simulated:

- camera pixel size: $3.45 \mu m \times 3.45 \mu m$
- wavelength: $0.633 \mu m$
- imaging system magnification: 30
- numerical aperture of the microscope objective: 1.3

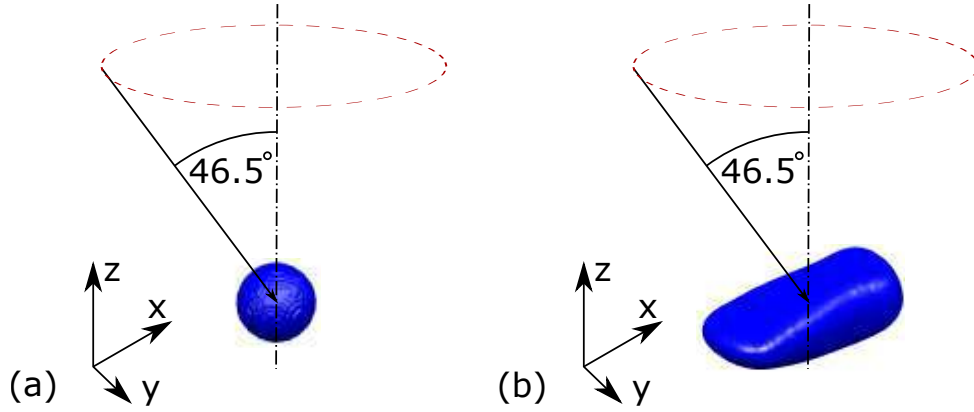


Figure 3.6: Numerical projection acquisition scenario and orientation of the phantom objects with respect to the optical system in the case of a (a) sphere, (b) biological cell.

- illumination scenario: conical (see Fig. 2.8) with $\theta = 46.5^\circ$
- number of captured projections: 180

The appearance of an example of phase and amplitude projections of both phantoms is shown in Fig. 3.7.

3.3.2 Proof of concept

In this section, the advantage of the tomographic reconstruction algorithm (GP) supported with the TVIC approach over a reference tomographic algorithm (GP only), in terms of the reconstruction quality, is presented.

To prove the efficiency of the TVIC-GP method, the micro-sphere phantom is reconstructed. The projections are created according to the sinogram generation procedure described in the previous section. Both GP and TVIC-GP approaches are stopped automatically when the changes in the reconstruction, introduced by next iterations, are sufficiently small. Figure 3.8(c,d) presents the $x-z$ and $x-y$ cross-sections through the center of the reconstruction calculated with the GP method. Analogous results for the TVIC-GP procedure are presented in Fig. 3.8(e,f). In Fig. 3.8(a,b), the reference cross-sections are presented. The $x-y$ cross-sections in both cases look similar. However, when TVIC-GP is used, a significant improvement in the $x-z$ cross-section is visible. Firstly, the boundaries of the sphere are correctly reconstructed and the elongation of the reconstruction in the z direction is no more present. What is more, the refractive index distribution inside the sphere is retrieved with increased accuracy. The reconstruction improvement is better visible in Fig. 3.9, where the 1D z -cross-sections through the $x-z$ results presented in Fig. 3.8 are shown. The gray color in the plot is the central 1D z -cross-section through the reference phantom data. The red and blue lines represent the reconstructions calculated with GP and TVIC-GP, respectively. It can be easily noticed that the TVIC-GP procedure

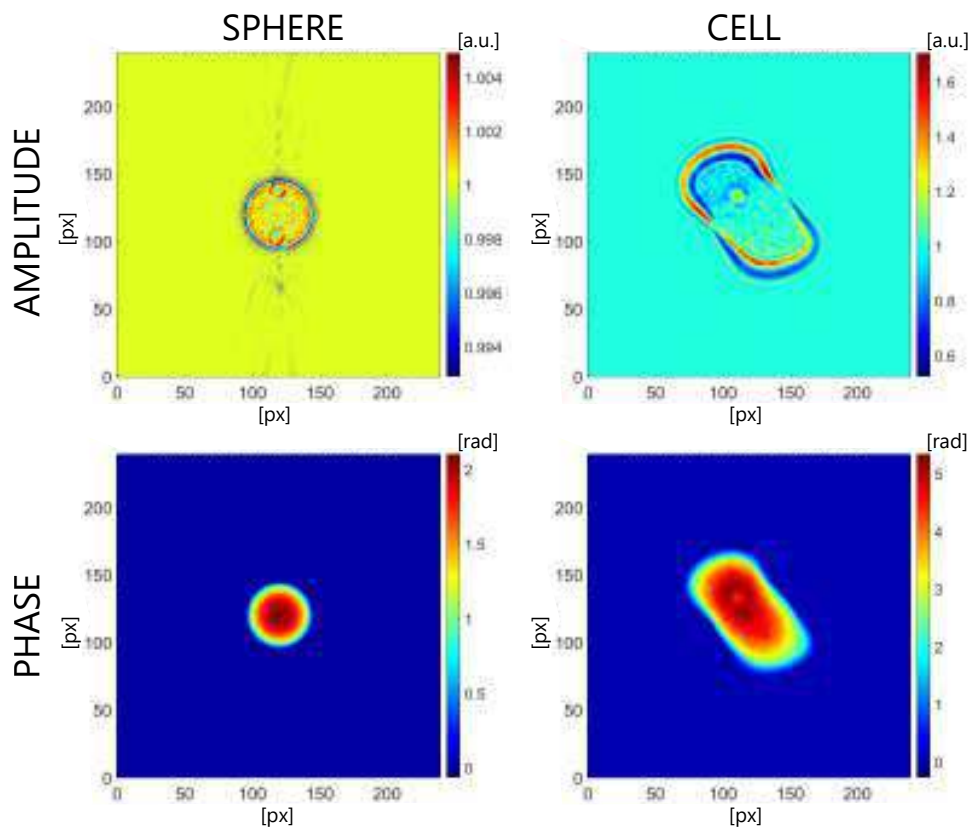


Figure 3.7: Example amplitude and phase numerical projections for (a) the sphere and (b) biological phantom.

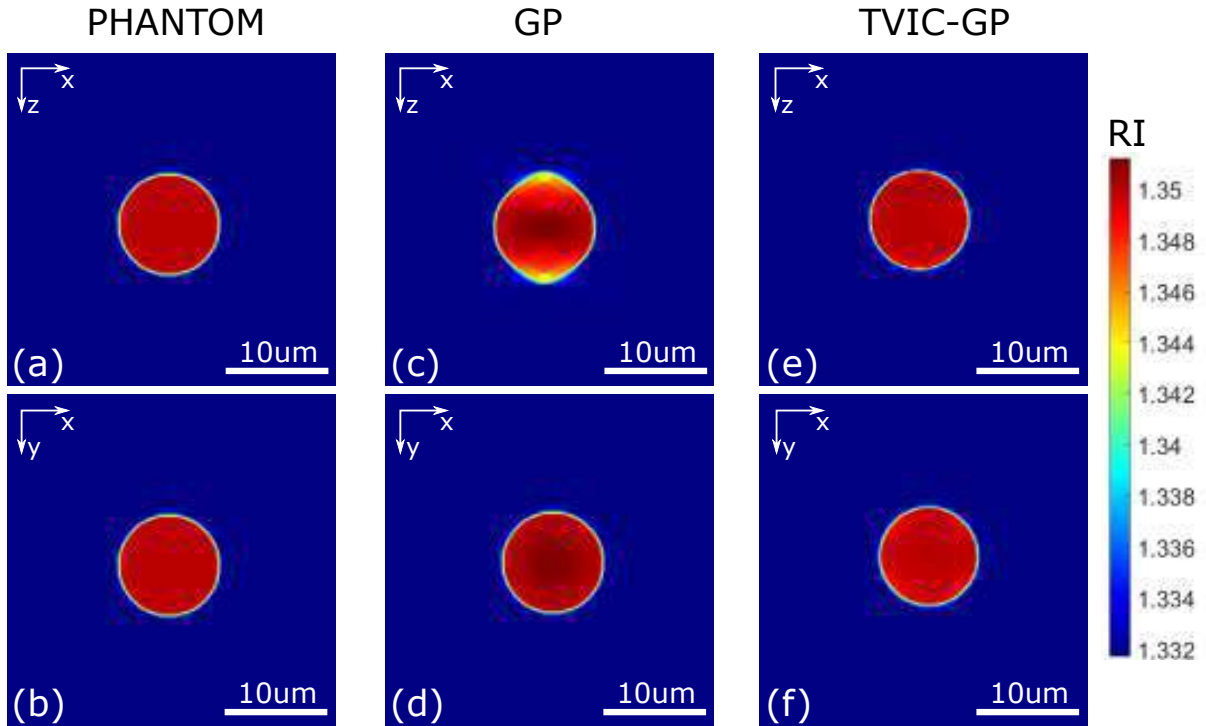


Figure 3.8: Two-dimensional cross-sections through the phantom object and two reconstructions calculated with the GP and TVIC-GP procedures. RI - refractive index.

retrieves the object boundaries and the inner refractive index distribution with higher accuracy. This property is associated exclusively with the utilization of the 3D mask with the retrieved precise information about geometry of the analyzed sample. Basically, the cross-section shown in Fig. 3.9 is always the worst-quality cross-section in the whole reconstruction volume as it covers the distortion of the result in the z direction. Therefore, here the reconstruction errors have the highest values. When the TVIC-GP method is used, the error of refractive index in this cross-section, understood as the maximum difference between the TVIC-GP reconstruction and reference data, is smaller than 0.001. Thus, with regard to simulations, the metrological requirement stated in the "Aim of the Thesis" is fulfilled for this object.

To confirm the above observations, global quality values were calculated: when the GP algorithm has been used, the RMSE calculated for the whole measurement volume equals 9.46×10^{-5} , and the Q parameter equals 99.08% for the $x - z$ and 99.93% for the $x - y$ cross-sections, respectively. When the TVIC-GP method is applied, the RMSE equals 5.78×10^{-5} , and the Q parameter equals 99.69% and 99.54% for the $x - z$ and $x - y$ cross-sections. Especially the RMSE values show a significant improvement in the reconstruction quality. What is more, the TVIC-GP reconstruction has been calculated in 10 iterations in comparison to 21 iterations that were necessary in the GP case.

To further visualize the effectiveness of the TVIC-GP algorithm, the above analysis is repeated for the biological cell phantom. All the sinogram generation and reconstruction param-

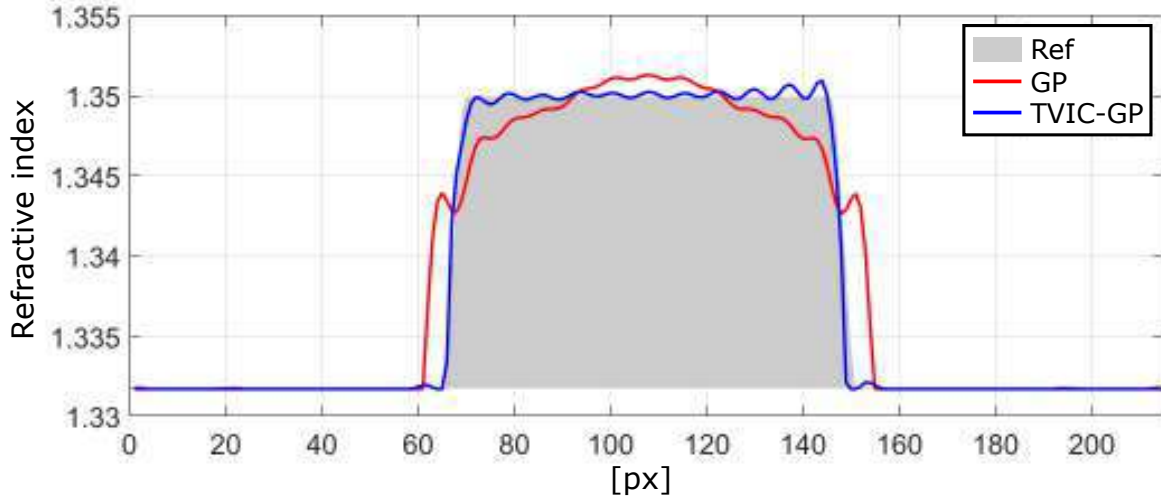


Figure 3.9: One-dimensional cross-sections in the z direction through the two-dimensional $x - z$ cross-sections presented in Fig. 3.8.

eters remain unchanged. The GP and TVIC-GP algorithms are stopped automatically. The cross-sections through the phantom data and the reconstructions calculated with GP and TVIC-GP are shown in Fig. 3.10. The advantage of the TVIC-GP procedure over the GP is clear. The boundaries are retrieved perfectly. What is more, the improvement of the refractive index distribution in $x - z$ and $x - y$ cross-sections is evident. Again, these observations are supported with the 1D z -cross-sections shown in Fig. 3.11. Close inspection of this cross-section reveals that in most part the error is smaller than 0.05. The only place, where it takes higher values is the central part, where the vacuole is present. Similarly to the case of the micro-sphere, this is associated with steep edges.

As before, the global quality values confirm the enhanced reconstruction quality. For the GP case, the RMSE calculated for the whole measurement volume equals 7.33×10^{-4} , and the Q parameter equals 99.05% for the $x - z$ and 99.48% for the $x - y$ cross-sections. For the TVIC-GP case, the RMSE equals 3.43×10^{-4} , and the Q parameter equals 99.21% and 99.28% for the $x - z$ and $x - y$ cross-sections. Again, these values show quality improvement, especially in the $x - z$ cross-section. Also, the TVIC-GP method stopped after 13 iterations, whereas the GP algorithm required 23 iterations.

3.3.3 Convergence analysis

Investigation of the algorithm convergence is one of the most important analyses that characterizes the efficiency of any iterative tomographic reconstruction method. In short, as the iterations progress, the tomographic reconstruction calculated with a tomographic reconstruction algorithm should approach towards the true refractive index distribution of an investigated sample. Often, it is possible to carry out a mathematical proof of the convergence of a given

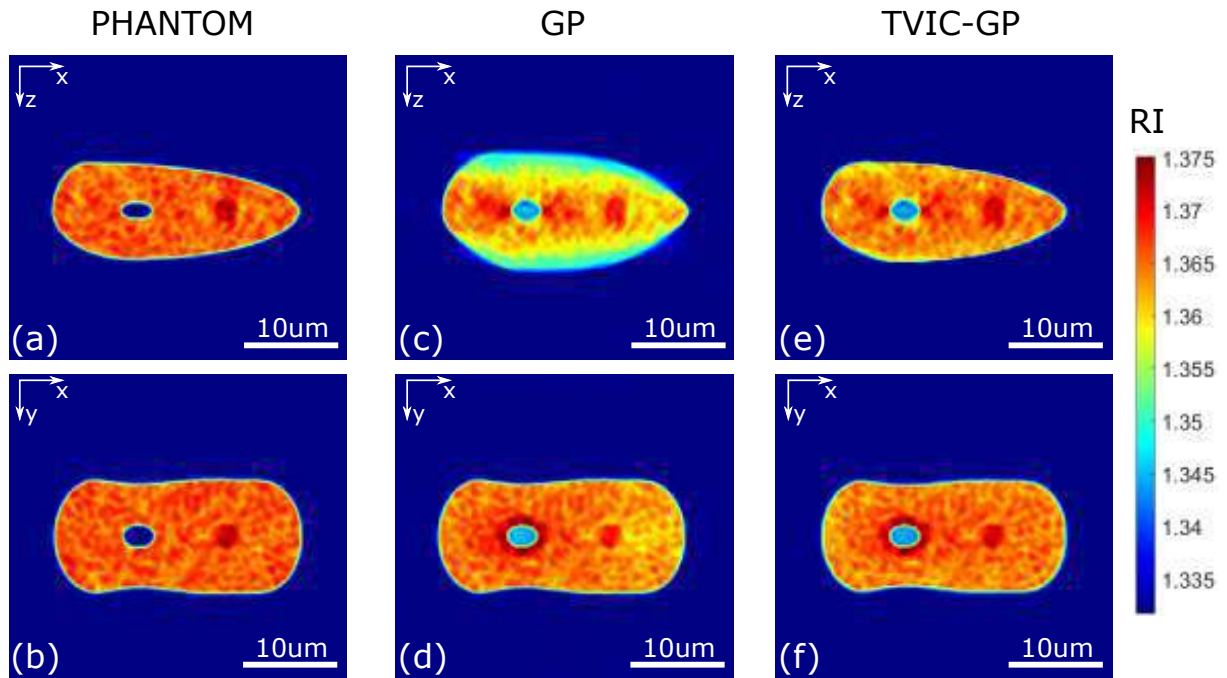


Figure 3.10: Two-dimensional cross-sections through the biological phantom object and two reconstructions calculated with the GP and TVIC-GP algorithms. RI - refractive index.

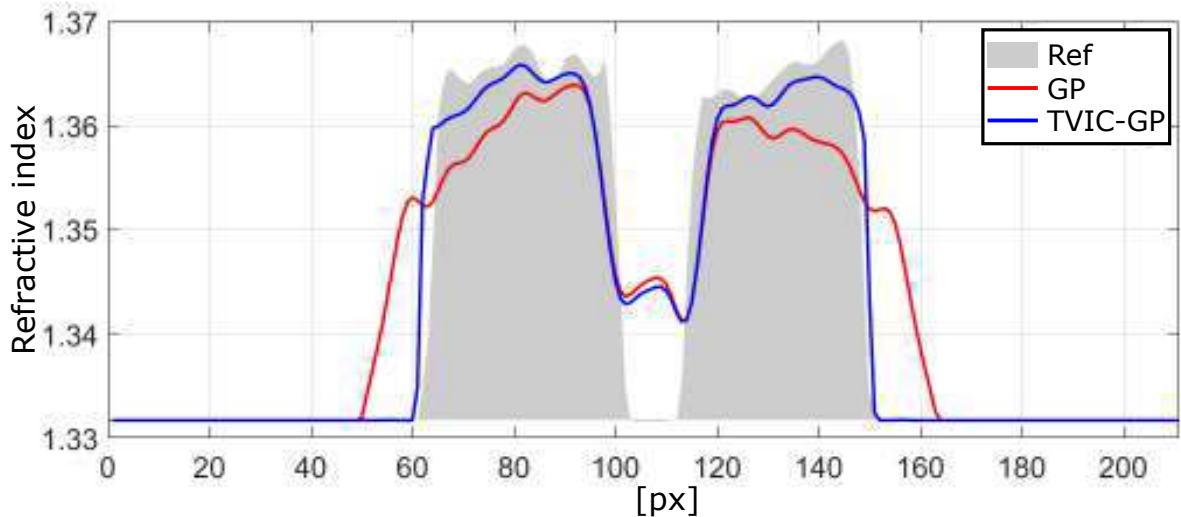


Figure 3.11: One-dimensional cross-sections in the z direction through the two-dimensional $x-z$ cross-sections presented in Fig. 3.10.

method. This assures the effectiveness of the algorithm.

Basically, tomographic algorithms have different convergence properties. In one group of methods, the quality of the reconstruction will increase together with the iterations up to a point, where no more improvement is visible and the solution stagnates. In the other group, instead of stagnating, the quality of the reconstruction decreases after a certain critical number of iterations is reached. When numerical simulations are carried out, it is relatively simple to specify the stopping criterion for both groups of algorithms. What is necessary, is calculation of the quality of a reconstruction after every iteration. This quality is specified by comparing the current reconstruction with the phantom data. Then, the quality of the current reconstruction is compared with the quality of reconstructions in previous iterations, and based on that comparison, the stopping criterion is set. In the first group of algorithms, when the quality difference between two consecutive iterations drops below a certain value, the algorithm is stopped and next iterations are not calculated. In the second group, the stopping occurs when the quality starts to decrease [49].

In this section, the convergence property of the TVIC-GP approach is investigated. Since the TVIC-GP method is not an analytical one, it is not possible to mathematically determine the convergence. It is, however, possible to conduct a simulation which will experimentally show how the quality of the calculated tomographic reconstruction changes as the algorithm iterations progress.

The analysis has been carried out with the biological cell phantom. 180 object projections have been acquired according to the procedure described in the previous section. First, a mask with the 3D geometry of the phantom has been retrieved by running the 1st stage of the TVIC-GP procedure. The mask is then passed to the second stage, the GP algorithm. For this experiment (and this experiment only), 100 GP iterations were run. The quality of the reconstruction calculated in each iteration of the GP algorithm supported with the TVIC strategy is presented in Fig. 3.12. The figure presents the RMSE (calculated for the whole reconstruction volume) and Q values (calculated for the central $x - z$ cross-section of the reconstruction) of the biological cell reconstruction. From the shape of the curves, it is clear that after a certain number of iterations is reached, the reconstructions become worse. In this specific case, this point is reached after 15 iterations for the Q parameter and 14 iterations for the RMSE. Therefore, it is important to stop the algorithm when this point (for Q or RMSE) is reached.

The analysis presented above proves how important it is to stop the TVIC-GP when the maximum of the Q-curve, or minimum of the RMSE-curve occurs. However, in real-life measurements, where biological micro-structures are investigated, there is no possibility to generate any of these curves, as there is no reference phantom with which the reconstructions can be compared. There are two solutions to this problem. The first involves performing a set of numerical simulations to experimentally find the optimal number of iterations for a given class

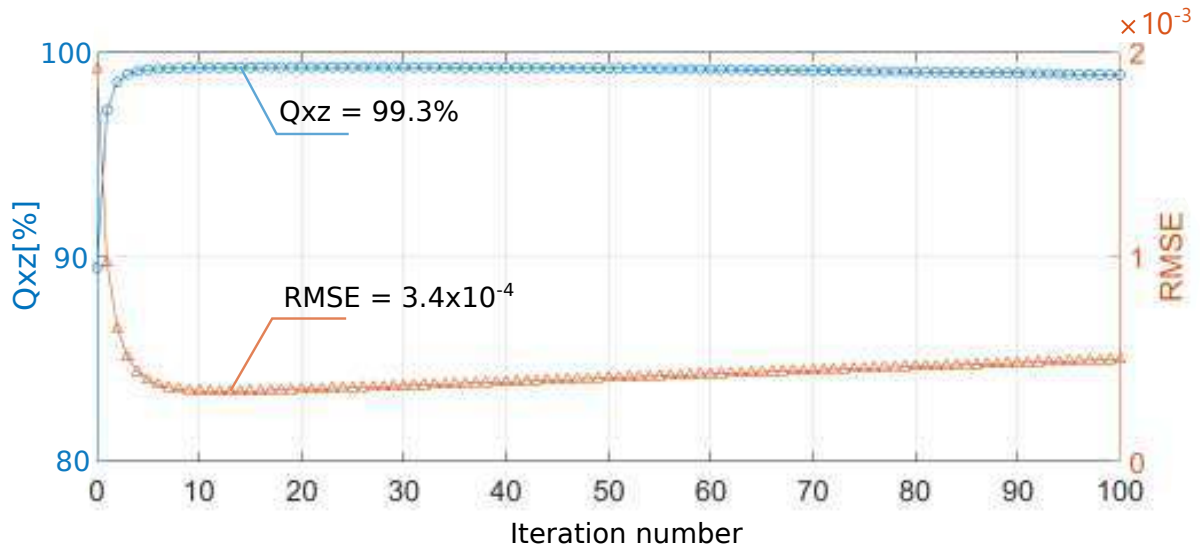


Figure 3.12: TVIC-GP convergence analysis presented as the dependency of RMSE and Q-parameter on the number of algorithm iterations in the case of noise-free projections.

of analyzed samples and use these values in physical measurements. In this approach, a table with the number of iterations associated with a given type of an analyzed object is created, e.g. 10 iterations for $10\mu\text{m}$ size biological cells in suspension, 20 iterations for histological tissue slices without staining etc. In the second approach, no look-up table is created. Instead, the differences between consecutive reconstructions (instead of the quality measures for these reconstructions) are calculated. Then, when the difference between two reconstructions is smaller than a threshold value, the algorithm stops. The justification for this method can be understood when one analyzed Fig. 3.12 again. Regardless of which curve is analyzed, it is clear that after approximately 10 iterations, the differences between next consecutive reconstructions are very small. The TVIC-GP method described in this Thesis utilizes the second approach.

To better understand the behavior of the TVIC-GP method, the convergence analysis in the case of noisy data is conducted. For this experiment, the sinogram of a biological cell phantom is used again. This time, however, noise is added to each phase and amplitude projection. In real-life experiments, the main source of the noise in projections is the electronic noise of the detector which captures the holograms. However, without tests it is difficult to determine how the noise from the hologram is transmitted into phase and amplitude of a projection, and thus it is not possible to create noisy phase and amplitude sinograms which would be a realistic input to the TVIC-GP method. To conduct the analysis in this section in a reliable way, a synthetic off-axis hologram, which mimics a real hologram captured in the LAODT setup, is created. This hologram is presented in Fig. 3.13(a). It simulates the case, where two spherical objects are in the measurement volume of the LAODT setup. The two objects are at different depths, however, one of them is currently in focus. In the next step, a random Gaussian noise is added to the hologram (see Fig. 3.13(b)). The resulting signal-to-noise ratio (SNR) equals 6dB.

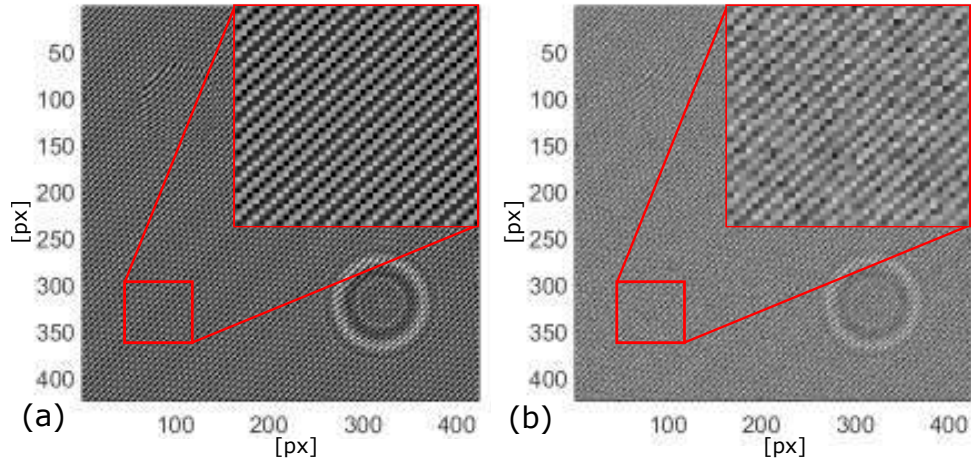


Figure 3.13: Synthetic hologram (a) without and (b) with Gaussian noise.

Next, both the noise-free and noisy holograms are processed with the Fourier transform method of phase and amplitude retrieval [20]. When the holograms are demodulated, the SNRs in the amplitude and phase distributions associated with the noisy hologram are calculated by comparing them with the corresponding noise-free distributions. This provides information on how the noise in the hologram is transmitted to the retrieved phase and amplitude. The SNR in the amplitude distribution equals 8.8dB and in the phase distribution 18dB.

This simple test allows me to generate phase and amplitude sinograms of a biological cell phantom with appropriate noise levels and without the inaccuracy introduced by the hologram demodulation procedure. These noisy sinograms are created by imposing the SNR from the example demodulated hologram presented above. This way, an evaluation of the convergence of the TVIC-GP method in real-life conditions can be conducted. The random Gaussian noise is added to the amplitude sinogram in such a way that the SNR for each projection equals 8.8dB. The noise with a different variance is added to the phase projections to achieve SNR equal to 18dB. It should be noted that this procedure is only an approximated way of generating noise and does not follow the physical process of noise creation fully. Because each phase projection in the phase sinogram has a slightly different variance, and due to the fact that when the Gaussian noise is added to each projection, a constant SNR is enforced, the variance of the noise in each projection also differs, which should not be the case (the same is true for the amplitude projections). Still, however, the projections generated in this simplified way may provide important information about the effectiveness of the TVIC-GP procedure when holograms with SNR equal to 6dB are captured, as these projections are now used to reconstruct the refractive index distribution and to evaluate the convergence.

The resulting quality plot is presented in Fig. 3.14. The curves presented in this figure show that when TVIC-GP is used to process data from holograms with SNR equal to 6dB, the nature of the convergence does not change. After a number of iterations, the Q-curve and RMSE-curve

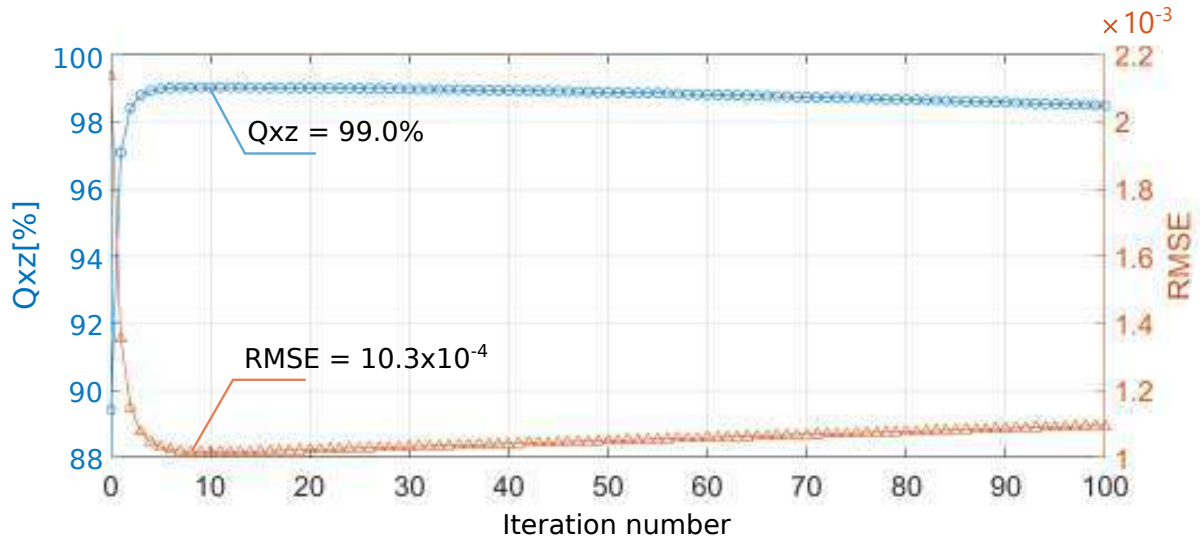


Figure 3.14: TVIC-GP convergence analysis presented as the dependency of RMSE and Q-parameter on the number of algorithm iterations in the case of noisy projections.

reach maximum and minimum, respectively. However, the maximum value reached by the Q parameter is lower when compared to the noise-free case (99.0% vs 99.3%) and the minimum value of RMSE is higher (10.3×10^{-4} vs 3.4×10^{-4}), which is expected. This experiment proves that the TVIC-GP procedure is predictable in real-life scenarios.

3.3.4 Dependence of the reconstruction quality on the number of projections

In ODT, and LAODT in particular, it is crucial to understand how the number of acquired projections influences the quality of the calculated reconstruction. If the number of projections can be reduced without significant loss of the reconstruction accuracy, both the data acquisition and reconstruction time can be highly limited. This, in turn, leads to the possibility of investigating dynamic processes that are taking place in biological specimens. At the same time, this relation is one of the most important ways of evaluating the efficiency of the reconstruction algorithm. Thus, in this section, an analysis showing the dependence of the TVIC-GP reconstruction on the number of input projections is carried out.

The analysis is conducted with the biological cell phantom. 180 noise-free projections were first generated according to the procedure described in Section 3.3.1. First, a sinogram consisting of all available projections has been used to calculate the tomographic reconstruction. As was described in Section 3.1, 100 iterations of the TpV procedure were calculated to generate the object mask, which is passed to the second stage of the TVIC-GP method. In the next step, GP iterations were calculated with the automatic stopping criterion described in previous section. Then, the quality of the obtained reconstruction is calculated by comparing the recon-

struction with the utilized cell phantom. The Q parameter is calculated for central $x-y$ and $x-z$ cross-sections through the reconstruction and the RMSE is calculated for the whole reconstruction volume. When the quality parameters are saved, the procedure is repeated for a reduced number of projections in the sinogram. In this study, the following set of projection numbers has been analyzed: 180, 165, 150, 135, 120, 105, 90, 75, 60, 45, 30, 25, 20, 15, 10, 5. Selected reconstructions are presented in Fig. 3.15. The quality plots are shown in Fig. 3.16. This plot shows that the quality of the calculated reconstruction changes only slightly when the number of projections used is greater or equal to 90. This conclusion is supported both by the RMSE and Q-parameter curves. When the number of projections is further reduced, the accuracy of the retrieved refractive index distribution decreases significantly.

The above experiment has been repeated for the GP algorithm and the quality plots are shown in Fig. 3.15 with dotted lines. Inspection of this plot reveals that GP algorithm gives significantly worse results when it is not supported with the TVIC strategy. This relation is true for all numbers of projections analyzed in this experiment except for the case with 5 projections where the value of the Q parameter is higher for GP than for TVIC-GP. This analysis is another confirmation of the effectiveness of the TVIC-GP procedure.

The analysis carried out in this section proves that when the TVIC-GP procedure is used, the number of acquired projections can be strongly reduced. This is a very important conclusion as it means that the projections acquisition time can be limited, which, in turn, allows LAODT to investigate dynamic processes that take place in live biological samples.

3.3.5 Analysis of the reconstruction clearing efficiency

In this section, the efficiency of the reconstruction clearing procedures, described in detail in Section 3.2, is carried out. The objective of these methods is to remove all objects from the reconstruction volume but the greatest one.

For this experiment, the biological cell phantom is used. Additional 6 spherical inclusions are added to the phantom volume. Each inclusion has a diameter of 50 pixels (or $12\mu m$ with the simulated pixel size of $0.24\mu m$) and a constant refractive index value of 1.42. These inclusions symbolize unwanted objects that are often present in the measurement volume, like dust particles or cellular debris. The distribution of these objects is presented in Fig. 3.17.

First, the procedure where the modified version of the mask (describing only the investigated object) is applied to the final tomographic reconstruction is analyzed. The numerical sinogram of the biological cell phantom with inclusions has been reconstructed with the TVIC-GP approach. The standard version of the mask has been applied in every iteration of the algorithm. When the tomographic reconstruction has been calculated, the modified version of the mask, with only the investigated object left, has been used. In Fig. 3.18 the effect of utilizing this procedure is shown. In Fig. 3.18(a) and (b), the standard and modified version of the mask is

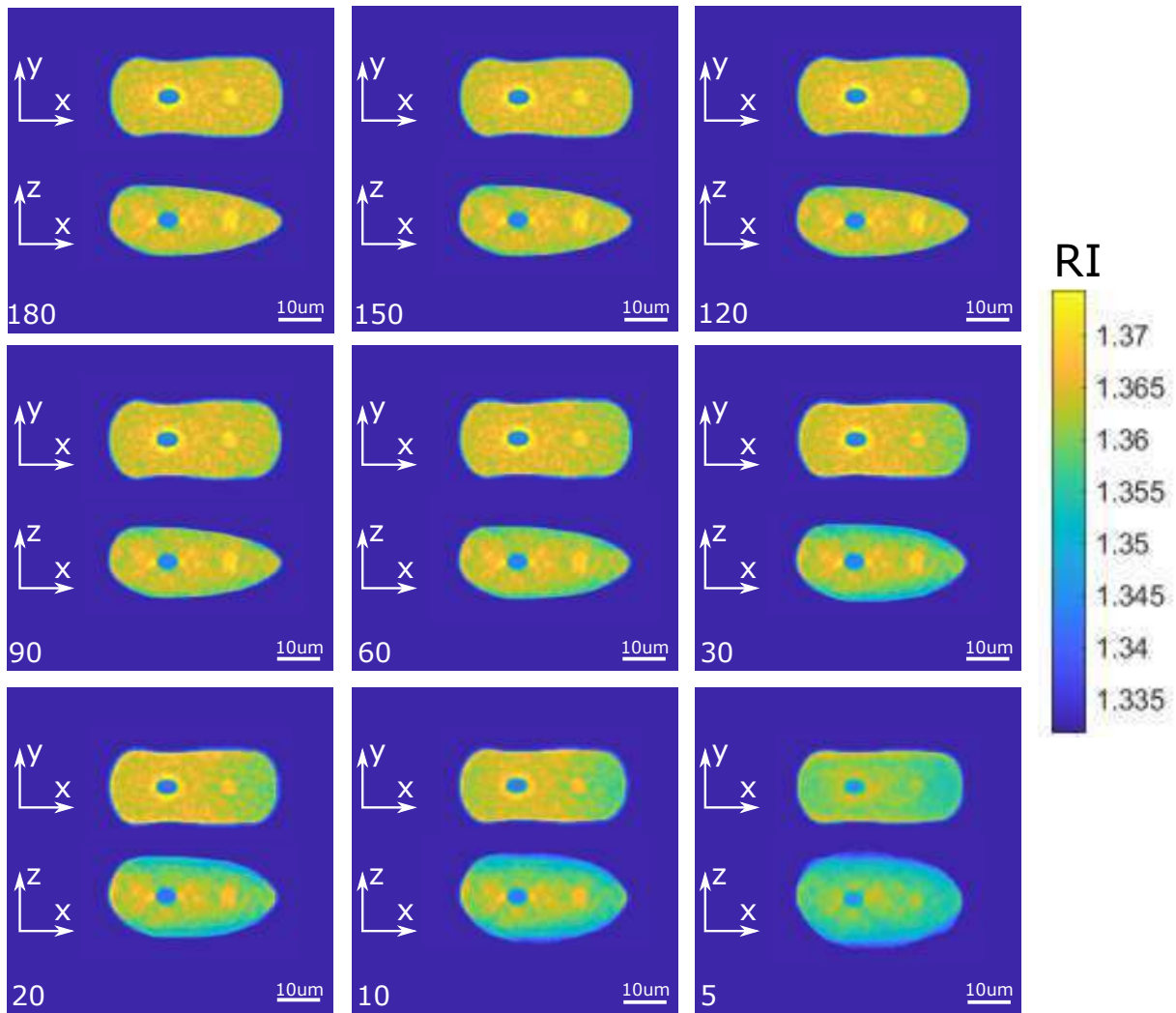


Figure 3.15: Selected $x - y$ and $x - z$ cross-sections through the reconstructions calculated with TVIC-GP for different number of input projections. The number in the corner is the number of projections. All reconstructions share the same color bar. RI - refractive index.

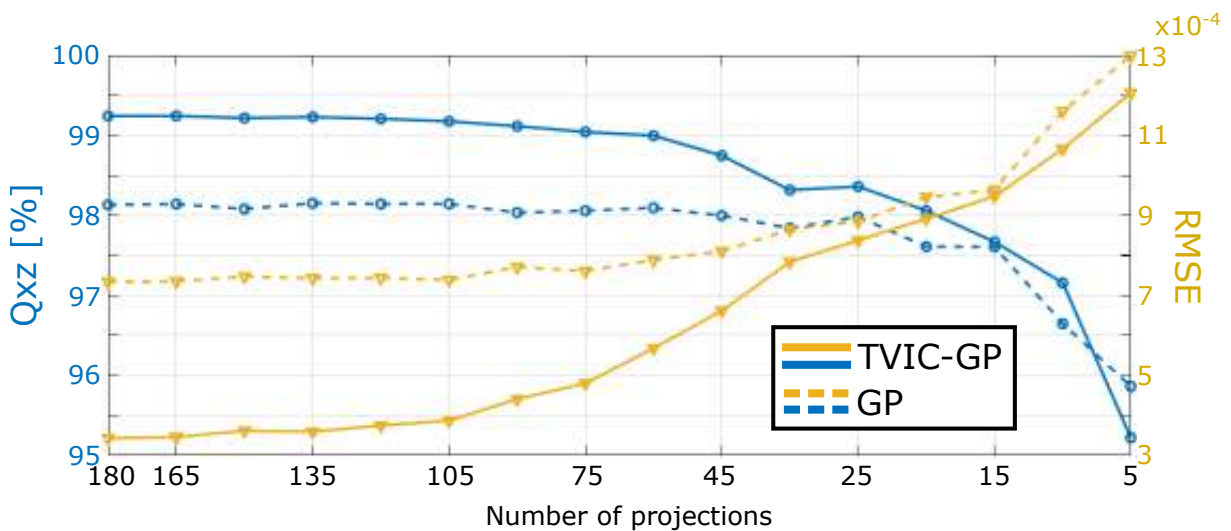


Figure 3.16: TVIC-GP and GP reconstruction quality as a function of number of projections.

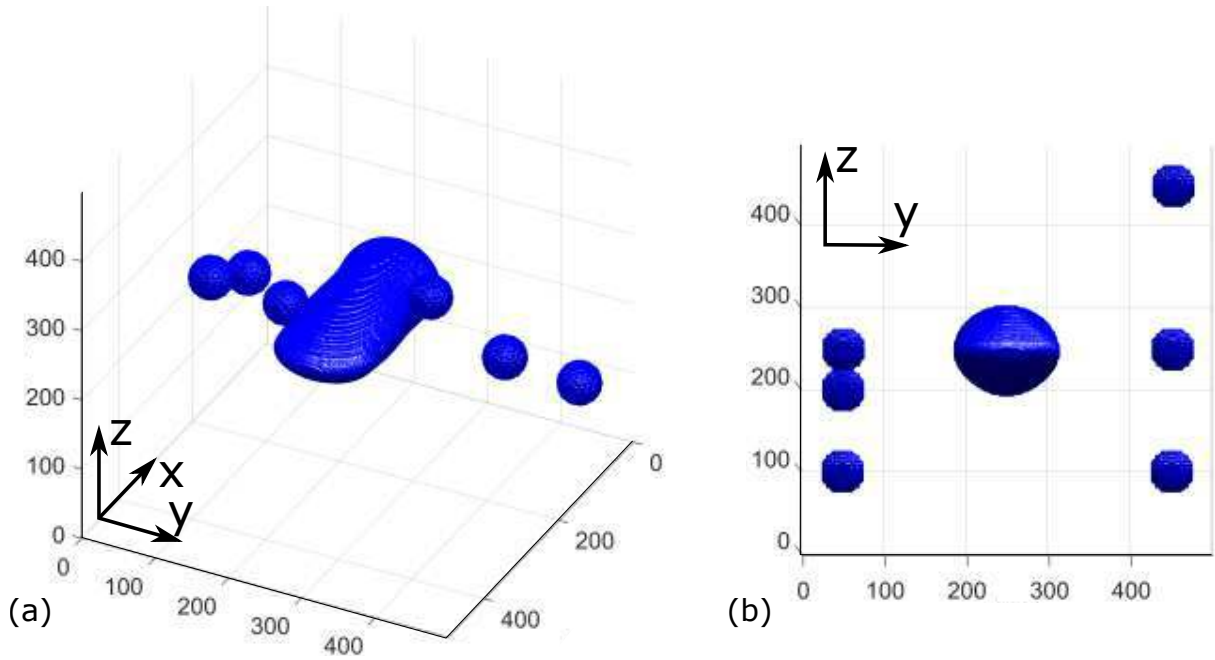


Figure 3.17: Visualization of the biological cell phantom with 6 spherical inclusions.

presented. In Fig. 3.18(c), the $x-y$ and $x-z$ cross-sections through the final cleared reconstruction is shown. The Q parameter calculated for this reconstruction is equal: $Q_{xy} = 98.47\%$ and $Q_{xz} = 98.93\%$ for the central $x-z$ and $x-y$ cross-sections, respectively. The RMSE calculated for the whole 3D reconstruction equals 6.52×10^{-4} .

The second, more advanced, procedure for clearing the reconstruction, which involves clearing the input phase sinogram is now evaluated. The same numerical phantom is used as in the previous experiment. The effect of applying this procedure is presented in Fig. 3.19. In Fig. 3.19(a) phase distribution of one of the numerical tomographic projections is shown. In Fig. 3.19(b), the same projection after applying the sinogram clearing algorithm is presented. Residual phase of the inclusions is still visible, however, most of their phase has been removed. The final tomographic reconstruction calculated with the TVIC-GP strategy supported by this sinogram preprocessing approach is shown in Fig. 3.19(c). The presented cross-sections look similar to the ones presented in Fig. 3.18(c), however, the quality is higher: $Q_{xz} = 99.14\%$ and $Q_{xy} = 99.07\%$ for the central $x-z$ and $x-y$ cross-sections, respectively, and $RMSE=5.41 \times 10^{-4}$.

Conducted experiments prove that the second approach of clearing the reconstruction gives results with higher quality. However, as it was mentioned, it is also more computationally demanding.

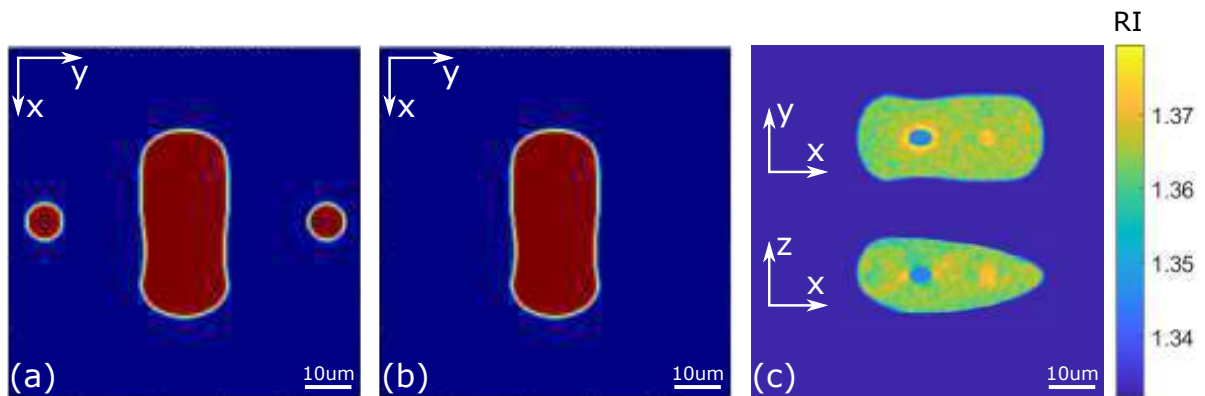


Figure 3.18: Visualization of the effect of applying the reconstruction clearing procedure for removing unwanted objects from the reconstruction: (a) $x - y$ cross-section through the standard mask; (b) the same cross-section through the modified mask with removed unwanted objects; (c) $x - y$ and $x - z$ cross-sections through the final reconstruction. RI - refractive index.

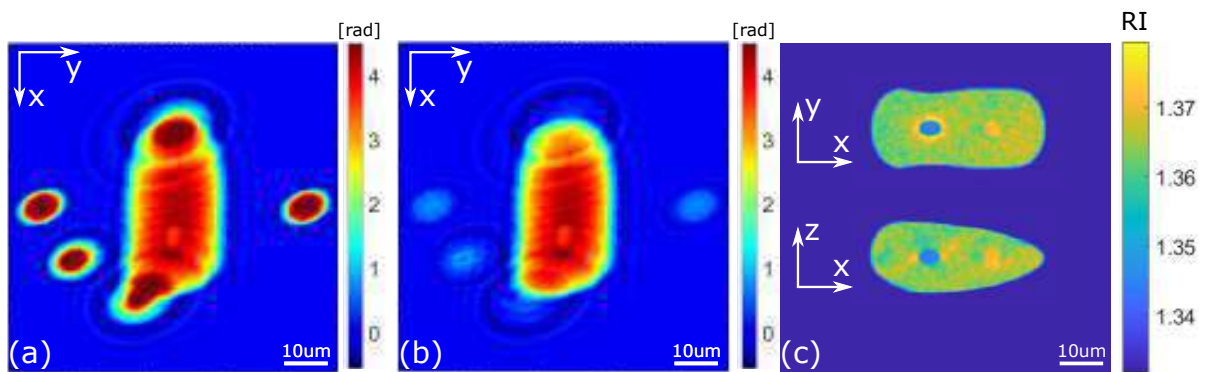


Figure 3.19: Visualization of the effect of applying the sinogram clearing procedure for removing unwanted objects from the reconstruction: (a) phase distribution of 1 of the numerical projections of the biological cell phantom - unwanted objects visible; (b) the same projection with removed unwanted objects; (c) cross-sections through the final reconstruction. RI - refractive index.

3.4 Conclusions

In this section, the TVIC-GP approach has been thoroughly tested. The analyses that were carried out show that this approach is a comprehensive method for precise reconstruction of the 3D refractive index distribution of non-piecewise-constant biological micro-samples.

The most important conclusion from this section is the fact that this approach effectively limits the distortion of a 3D reconstruction that is usually present due to limited angular range of acquired projections of a measured phantom with biological characteristics. Both the geometry and the inner refractive index distribution is significantly corrected. **These simulations give grounds to confirm the research hypothesis stated in this Thesis.** However, the experimental verification is still necessary, and is presented further in the Thesis.

It has been shown that the algorithm converges to the solution even when the investigated object's projections are noisy, which is an important conclusion. What is more, the tests proved that the number of input projections can be significantly limited. Also, a reconstruction clearing procedure has been proposed which be a significant help when the evaluation of the results is to be performed by medical doctors and biologists.

All these analyses lead to the conclusion that TVIC-GP approach is, according to my knowledge, the first effective tomographic reconstruction procedure dedicated to measurement of biological samples in LAODT.

However, this method does not correct all errors that are present in the reconstruction. In particular, certain errors in retrieval of the refractive index may be observed in parts of a reconstruction that are distant from the central $x - y$ plane: see Fig. 3.10(e) where the refractive index erroneously decreases near the horizontal boundaries of the biological cell phantom. Thus, in the next section a solution to this problem is proposed and tested.

Chapter 4

Extended depth-of-field LAODT

As it has been mentioned in the previous Chapter, one of the drawbacks of LAODT that is not solved by the TVIC strategy is the non-isotropic resolution of the tomographic reconstruction. In fact, the resolution is maximum in the region of the reconstruction that is within the depth of field (DOF) of a utilized microscope objective and decreases with the distance from this region. This phenomenon makes it difficult to identify all the inner structures of an analyzed sample. This is especially problematic, when the sample is thick and some inner structures are found near the object boundary. In this section, the detailed description of the origin of this problem together with a solution is described.

4.1 Problem description

The basic step in LAODT is acquisition of a single projection. As a result, a hologram with encoded information about the integrated complex refractive index distribution along the illumination direction is recorded by a detector. A microscope objective in the optical setup conjugates a central z -plane (where z is the optical axis) of the measurement volume with a detector, and thus the part of the integrated complex refractive index that comes from the surrounding of this z -plane is diffraction-free since it is within the DOF of the optical setup. DOF highly depends on the NA of the optical setup, according to the relation:

$$DOF \propto \frac{\lambda n}{NA^2} \quad (4.1)$$

where λ - wavelength in vacuum, n - immersion refractive index, NA - numerical aperture.

So, it is clear that with high NA microscope objectives, utilized in LAODT setups, DOF is extremely shallow. This is important, because the effect of non-central planes (z -planes that are outside of DOF) on the integrated complex refractive index is nonlinear. When analyzing the influence of these z -planes, it is necessary to take diffraction into account. What is more, the

further the z -plane is from the center of a measurement volume, the more significant the effect of diffraction is.

The two well-known methods that linearize the relationship between refractive index distribution of z -planes that are outside of the optical system DOF with the recorded projection are 1st order Born and Rytov approximations, described in Sec. 2.2.2. It has already been proven that when biological micro-structures are measured, 1st order Rytov approximation provides superior results.

The property of spatially-variant resolution is inherent to the Rytov approximation that is utilized during the numerical reconstruction procedure. However, there is a lot of confusion in research papers regarding this subject. In particular, many sources claim that the Rytov approximation has spatially invariant accuracy. In [43], one can read “This condition basically asserts that the Rytov approximation is independent of the specimen size and only limited by the phase gradient (...)”. Also, in [53] it reads “(...) the size of the scatterer is not a factor in determining the accuracy of the Rytov approximation”. It can be argued that these statements are not precise and may lead to incorrect conclusions. While it is true that the validity condition for the Rytov approximation is associated only with the phase gradient (unlike Born approximation), it is not equivalent to the fact that a 3D reconstruction calculated with the Rytov approximation will have a uniform resolution in the whole measurement volume. This is just the condition for the type of an object that can be reconstructed with this approximation. Let us recall the Helmholtz equation in the complex phase form from Section 2.2.2:

$$(\nabla^2 + k_0^2)u_0(\vec{r})\Psi(\vec{r}) = -[(\nabla\Psi(\vec{r}))^2 + f(\vec{r})]u_0(\vec{r}) \quad (4.2)$$

The Rytov approximation is carried out by removing the component with the gradient of the complex phase from this wave equation. This operation can be successfully performed when this gradient is small (only then the approximation holds). Consequently, the gradient of the complex phase is small when the gradient of the refractive index distribution in the measurement volume is small. Note that if the gradient of the object’s refractive index distribution is small, the gradient of the Rytov field emitted by a chosen object plane will be small regardless of the thickness of the object, and in this sense the Rytov approximation does not depend on the object size. This can be compared with the Born approximation which depends on the total energy of the scattered field. The above equation is, however, used to propagate the complex field and to calculate the tomographic reconstruction. Since this is not a rigorous propagation algorithm, it introduces errors, and these errors increase with the propagation distance from the plane in focus of the optical setup. As a result, the resolution of the reconstruction decreases with the distance from the center of the measurement volume (in the case of ODT with object rotation) or from the focal plane in the object space (in the case of LAODT). It is important to understand that despite the fact that in the TVIC-GP method no propagation is directly calculated, filling the

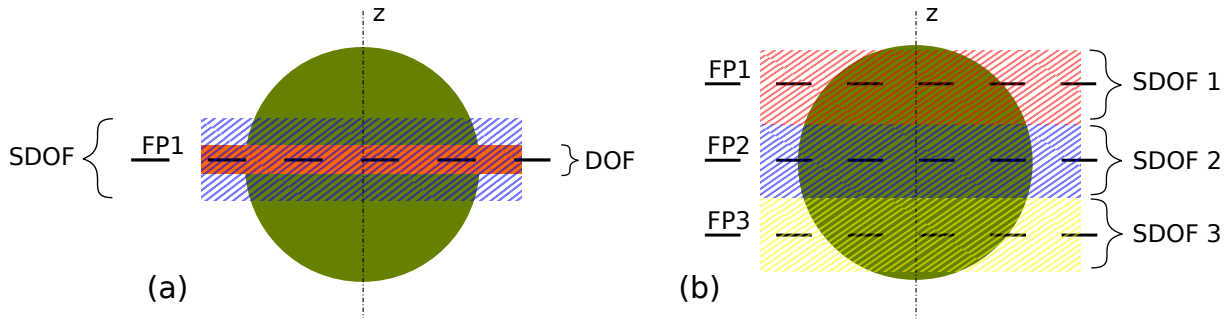


Figure 4.1: Example of a measured micro-sphere with illustrated (a) depth-of-field (DOF) and synthetic depth-of-field (SDOF); (b) arrangement of SDOFs in focus-tunable tomography; FP - focal plane. [83]

spectrum with complex phases on Ewald's spheres and calculating the inverse Fourier transform (which takes place in the second stage of TVIC-GP) is equivalent to direct propagation of the complex phase with the simplified wave equation presented above, as has been proved in [87], and thus, the same errors are present. It should be noted that these errors are superimposed with the errors that are due to inaccurate interpolation of data in the Fourier space. However, these have known character [88] and were not analyzed in this chapter. Further literature covering this subject can be found in [89, 90].

In the case of LAODT, if the errors in the calculated tomographic reconstruction increase with the distance from the focal plane, one can define a Synthetic Depth of Field (SDOF) as a region around the focal plane, in which the Rytov approximation holds. As it was described in [90], the errors introduced by the Rytov approximation depend on the refractive index contrast in the investigated sample, and thus the thickness of the SDOF will change when different objects are investigated. Unfortunately, currently there is no established method for defining the thickness of the SDOF in the case of LAODT. Instead, it can be estimated for a given class of biological micro-structures based on experiments. It is, however, clear that the size of SDOF is significantly larger than the size of a standard DOF of the imaging system. Inside SDOF, diffraction effects are compensated in the reconstruction process. A symbolic relationship between DOF and SDOF is presented in Fig. 4.1(a). If the measurement volume is large, i.e. the thickness of a cell or tissue sample is significant, the SDOF may cover it only partially. As a result, when a tomographic reconstruction is calculated, regions of a sample that are outside of SDOF have lower resolution compared to the parts that are within the SDOF due to violation of the Rytov validity condition. Such anisotropy of resolution deteriorates the measurement conditions and reduces the quality of the reconstructed data.

In principle this problem can be solved by proper manipulation of input holographic data and their processing as shown in [44, 91], where a complex field retrieved from each projection is rigorously propagated to multiple planes that cover the range of the whole sample. In the

next step, Rytov fields are calculated from the propagated fields and the final reconstruction is obtained. This method requires capturing only a single set of projections, which is a significant advantage. However, it involves extensive and time consuming data processing and it suffers from narrowed field of view.

The spatially-variant accuracy problem can also be addressed with hardware-based methods, in which a sample stage is scanned in z direction while acquiring projections [92]. Unfortunately, it is difficult to achieve high mechanical stability of such a setup, especially if a fast measurement is to be performed. Also, this removes the main advantage of the LAODT, namely stationarity of the investigated biological micro-object which is usually placed in a liquid environment.

Therefore, I propose an alternative method of capturing projections for multiple positions of focal planes in the measurement volume by introducing a liquid focus-tunable lens between an imaging microscope objective and a CCD camera. This solution, called Focus-Tunable Tomography (F-TT) [83, 93, 94], assures stationarity of an object and allows fast, optoelectronic-based selection of focal planes, for which the sequential sets of projections are captured, followed by tomographic reconstruction and stitching of the data volumes. This approach is combined with the TVIC-GP procedure to fully address the main downsides of LAODT, that is the missing frequency problem and spatially-variant axial accuracy. In this section the measurement methodology and full processing chain of this combined technique will be presented.

4.2 Main concept

The idea behind F-TT is to achieve quasi-uniform resolution within the whole object volume through acquisition of multiple projections for a single illumination direction. Each projection is acquired for a different position of the focal plane in the measurement volume. This way, SDOFs that correspond to different focal planes cover the whole measurement volume (see Fig. 4.1(b)).

A focus-tunable lens is a liquid-filled membrane, whose optical power is controlled with electric current and which can change its curvature 60 times per second. Thus, by applying specific values of electric current, different sections of an investigated sample are conjugated to the detector plane. The measurement scenario is presented in Fig. 4.2. First, the lens is set to conjugate first focal plane (FP1) in the space of the object with the detector. Then, projections of the object are acquired with the illumination scanning system and a sinogram is created for the given optical power of the lens. Then, the electric current value is modified, and the procedure is repeated for FP2 and FP3. As a result of this stage, multiple sinograms are recorded for different focal planes in the object space.

In the example presented above, 3 focal planes were used. However, the number of focal

planes within a measurement volume varies, and depends on three parameters. The first is thickness of an investigated sample. For thick samples, more focal planes are necessary. The second parameter is a scattering potential of the sample. In the case of weakly scattering objects the distance between focal planes is higher than in the case of highly scattering ones. As a rule of thumb, in the case of highly scattering samples, like tissue sections, in order to achieve highly accurate results this distance should be set to around $0.5\mu m$, whereas in weakly scattering ones it may be around $2-3\mu m$. It should be noted, however, that the combination of scattering potential and thickness of an object has to be small enough for the light to pass through the measurement volume in a state that allows to correctly retrieve its phase and amplitude. This mainly refers to the phase unwrapping procedure, which in the case of strong noise or inconsistency in phase data returns significant errors. The last parameter is the allowed duration time of the measurement. If the biological sample under study is non-stationary or some dynamic phenomena are to be measured, fewer focal planes are used to limit the projection acquisition time. Ideally, the number of focal planes should be sufficient for the SDOFs to cover the whole volume of an investigated sample. In practice, a trade-off between the uniformity of the resolution and measurement time is necessary.

When all the data is acquired, the sinograms are processed. To achieve quasi-uniform resolution of a complex refractive index distribution, the following approach has been implemented. First, each sinogram is reconstructed independently with an appropriate reconstruction algorithm that works within the TVIC strategy. The choice of an algorithm depends on the type of a measured sample and design of an optical setup. As a result, a series of 3D reconstructions is obtained, where each reconstruction is calculated for a different focal plane position, which means that for each reconstruction the SDOF covers a different region. In the next step, from each reconstruction a fragment that is within its SDOF is extracted. Lastly, a final reconstruction is obtained through stitching of the cut-out fragments that represent data reconstructed with high accuracy. The processing scheme is presented in Fig. 4.2(a).

4.2.1 Numerical procedures

As it has been already mentioned, an arbitrary tomographic reconstruction algorithm can be used in F-TT. However, to achieve the best results, the chosen algorithm should be designed for LAODT systems to minimize errors that are due to limited angular range of acquired projections. The method described in this paper is dedicated to investigation of non-piecewise-constant, weakly scattering biological micro-samples, therefore it is justified to combine this technique with the TVIC-GP approach, which will reconstruct the sinograms. The TVIC-GP reconstruction of each of the sinograms is carried out in the same way as described in the previous sections. After a series of reconstructions are obtained, the appropriate fragments of these reconstructions are extracted and stitched with each other.

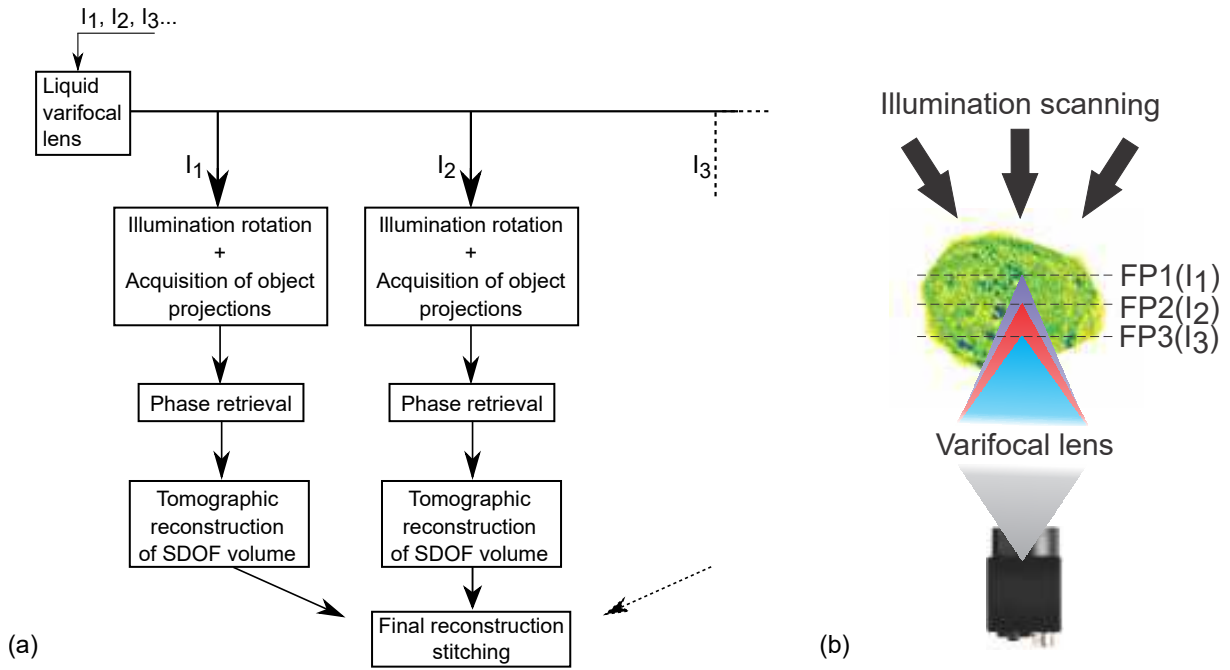


Figure 4.2: (a) Processing path in extended depth-of-field LAODT. I_1, I_2, I_3, \dots - electric current values controlling the focus-tunable lens; (b) projection acquisition scheme for different electric current values, FP1, FP2, FP3 - focal planes. [83]

The stitching procedure aims to combine the correctly reconstructed parts of the object (i.e. located within SDOFs) within a common coordinate system. The stitching method is a correlation-based technique. This method minimizes stitching errors that are due to possible object displacement between acquisition of consecutive sinograms and nonlinear response of a focus-tunable lens to electric current. The input to this technique are TVIC-GP reconstructions calculated for different focal planes. First, all obtained output matrices are sorted with respect to the electric current value applied to the focus-tunable lens. At a time, two adjacent reconstructions are stitched. For a given pair of reconstructions, e.g. for FP1 and FP2, two fragments that lie between the two focal planes are extracted. These parts, which represent the same piece of an analyzed object, are used to determine the translation vector. Initial matching of these fragments is carried out based on experimental knowledge, whereas fine tuning is conducted by calculating the cross-correlation between these fragments. The calculated translation vector is then used to stitch the two reconstructions. Stitching of data based on the translation vector can be successfully applied to F-TT because there is no rotation of the reconstructions calculated for different focal planes with respect to each other. This procedure is then repeated for stitching with the next reconstruction (i.e. with FP3).

4.3 Conclusions

In this Chapter I present a novel method for extended depth-of-field LAODT in which the change of a focal plane position is performed with a liquid focus-tunable lens, which together with the proposed processing of data guarantees a uniform resolution in the whole measurement volume. To implement this method, the LAODT setup with scanning of illumination have been modified by adding an axial scanning module which allows for aberration-free shifting of the focal plane during acquisition of object projections. The main advantage of this idea is lack of mechanical movement in an optical setup. This allows for analyzing biological specimens that are immersed in a liquid medium, without the risk of moving the object during projection acquisition stage.

The experimental verification of this method is presented in Section 5.2.

Chapter 5

Physical experiments

All the measurement setups described in this Chapter were built by MSc. Eng. Arkadiusz Kuś, who also acquired all of the object projections [57].

Biological experimental samples have been prepared at the Department of Transplantology and Central Tissue Bank, Centre of Biostructure Research of Medical University of Warsaw and at the Department of Pathology of Warsaw Medical University.

All numerical procedures described in this section are carried out in Matlab environment (version R2017a) on a PC with Intel i7 3770, 32 GB DDR3 RAM and Nvidia GeForce GTX 1070 8GB.

5.1 LAODT with TVIC-GP

In this section, the efficiency of the TVIC-GP approach is verified by presenting the reconstruction results for one technical reference object and one biological specimen. The reconstructions calculated with TVIC-GP are compared to the ones obtained with the Direct Inversion (DI) and GP methods. First, the optical setup used for the experimental verification is presented. Also, the data processing methods are described.

5.1.1 LAODT setup

To carry out the experiments in this part, the LAODT optical setup, presented in Fig. 5.1, is used for acquisition of projections of an investigated sample. The setup is based on the Mach-Zehnder configuration. To realize the illumination rotation, a galvanometric mirror (GM) is used. The laser beam ($0.633\mu\text{m}$ wavelength) is divided into the object and reference beams after it is reflected by the GM. This way, the beam inclination introduced by the GM affects both arms which results in a constant carrier fringes frequency in the detector plane, which simplifies the automatic fringe pattern analysis. The total magnification of the system is $76\times$

and the detector pixel size is $3.45\mu\text{m}$. The samples are illuminated with a conical illumination scenario (see Fig. 2.8(a)) with $\theta = 46.5^\circ$. The numerical aperture of microscope objectives is 1.3. For each investigated sample, 120 projections are captured.

When all projections of an investigated sample are captured, data preprocessing steps are conducted in order to retrieve the phase and amplitude information. In the LAODT optical setup described above, the projections are captured as in-plane, off-axis holograms, therefore to demodulate the object integrated phase and amplitude, the Fourier transform method [20] for fringe analysis is used. It is followed by the phase unwrapping technique based on sorting by reliability [34]. As was described in Section 2.3, each acquired projection is accompanied by a reference projection that is captured with the same parameters (illumination angle, focal plane position etc.) but without the investigated object in the measurement volume. These reference projections undergo the same phase retrieval procedure as object projections. After phase and amplitude information is extracted from all projections, complex phase is generated from each projection by dividing each object complex field by the reference complex field (from the reference projections), and by calculating the logarithm of this quotient, according to the Rytov approximation described in Sec. 2.2.2. Lastly, the complex phases are stacked to form a sinogram, which is the input data to the tomographic reconstruction procedure.

5.1.2 Objects description

First, in order to verify the proof of concept of the TVIC-GP, a static object with well defined geometrical and optical parameters is measured. The selected object is the PMMA micro-sphere (microParticles, Germany) with the diameter of $23.5\pm 0.36[\mu\text{m}]$ and a constant refractive index value in the whole volume $n_{He-Ne}=1.4905$ [95], so it represents an object with piecewise-constant refractive index distribution. For the measurement the micro-sphere has been placed in a sample chamber and immersed in a refractive-index-matching liquid at a slight mismatch ($n_D=1.5200$, $n_{He-Ne}=1.5173$, Cargille Series A).

To prove effectiveness of the TVIC-GP approach in reconstructing biological structures, a fibroblast cell is measured. The chosen cell comes from the permanent mouse fibroblast cell line Balb/c 3T3, which has been used in numerous validated biological tests [96]. The cells were cultured on Glass Bottom Dish, 35mm (Ibidi, Germany) in DMEM, supplemented with 10% fetal calf serum, 4 mM glutamine, penicillin and streptomycin in humidified incubator at 37°C , 7.5% CO_2 . The cells were seeded at concentration where single cells were available as a target for microscopy. The description of the cell preparation procedure as well as the cells themselves were provided by dr Dariusz Śladowski from Medical University of Warsaw. Unlike the PMMA micro-spheres, these cells represent objects with non-piecewise-constant refractive index distribution in the range of 1.36-1.41. These cells have length up to $50\mu\text{m}$ (although longer cells can be observed).

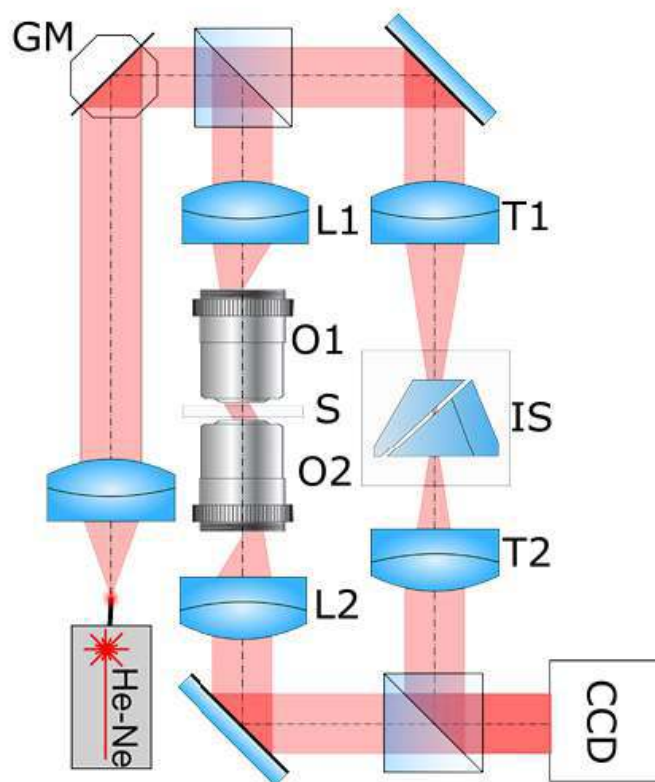


Figure 5.1: Optical setup for LAODT. GM - galvanometric mirror, L1,L2 - lenses, O1,O2 - microscope objectives, S - specimen stage, T1,T2 - collimating lenses, IS - inverting prism.
 Author: A. Kuś

5.1.3 Experimental results

The sinogram of the technical sample has been reconstructed with the DI, GP and TVIC-GP methods. In all cases, automatic algorithm stopping condition is used. All approaches are supported with the non-negativity constraint. The results are presented in Fig. 5.2.

The Figure proves that the DI algorithm, as the most simple one does not minimize the distortion of the reconstruction that is present due to limited angular range of acquired projections. The elongation in the z direction is clearly visible. What is more, the average refractive index of the reconstructed micro-sphere in the $x - y$ cross-section is too high (1.4963 while the reference value is 1.4905). Also, a strong noise around the retrieved object is present.

The GP method turned out to be relatively successful in retrieving the distortion-free reconstruction. The average refractive index in the $x - y$ cross-section (1.4929) is closer to the reference value. However, the elongation in the z direction is not completely corrected and the boundaries are still blurry. Again, the noise around the sample is present, although it is not as strong as in the case of the DI method. This reconstruction was calculated after 22 iterations.

Finally, the TVIC-GP procedure proved to be the most effective. The average refractive index (1.4931) is very similar to the result obtained with the GP algorithm. However, the elongation of the reconstruction is now almost entirely corrected. Also, all object boundaries are now sharper. This is caused by the mask, which, when applied in each iteration of the GP algorithm, increased the average refractive index value of the sphere near the boundaries, which proves the effectiveness of the TVIC strategy. What is more, the surrounding of the object is free from noise and artifacts associated with LAODT. This reconstruction was calculated after 10 iterations.

The above observations are supported with the cross-sections presented in Fig. 5.3, where the GP and TVIC-GP reconstructions are compared (the DI result is not presented as it clearly returns erroneous reconstructions). For clarity, reference values of the measured micro-sphere are also shown in the plot. It can be seen that the reconstruction calculated with the TVIC-GP approach is closest to the refractive index distribution of the reference micro-sphere. In the figure, the TVIC-GP reconstruction error is also presented. The error has been calculated as the absolute value of the difference between the TVIC-GP reconstruction and the reference data. One important conclusion that can be drawn from these images is that in the TVIC-GP reconstruction, significant errors are present at the boundaries. These errors resemble ringing artifacts, often present in image processing near sharp edges. Fortunately, beyond the boundary region, the reconstruction quality is high and the refractive index error is smaller than 0.01. Thus, in my opinion the metrological requirement stated in the "Aim of the Thesis" is fulfilled.

The experiment has been repeated for the biological cell. Again, reconstructions calculated with DI, GP and TVIC-GP are compared. The results are shown in Fig. 5.4.

Similarly to the measurement of the micro-sphere, DI method gives the worst results. The

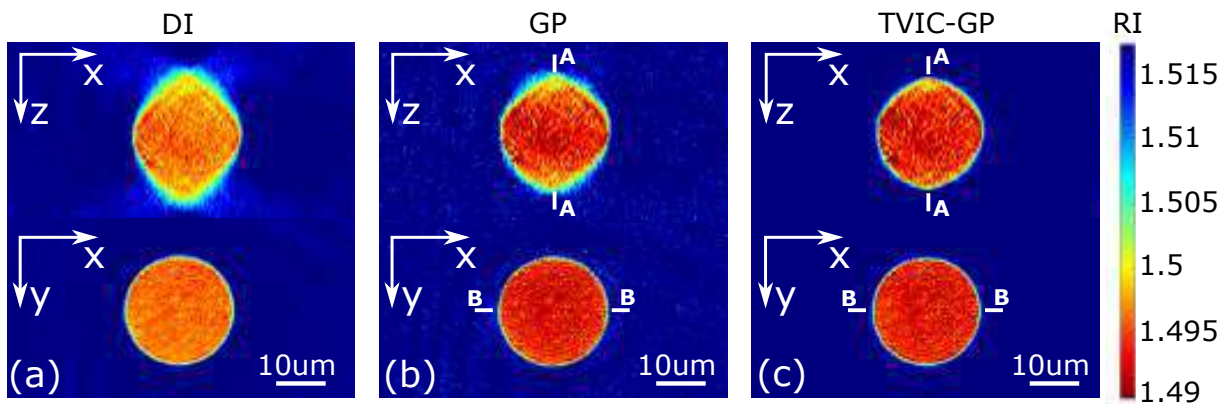


Figure 5.2: Cross-sections through the center of reconstructions calculated with (a) DI, (b) GP and (c) TVIC-GP procedures. All images share the same color scale. Note the inverted colorbar.

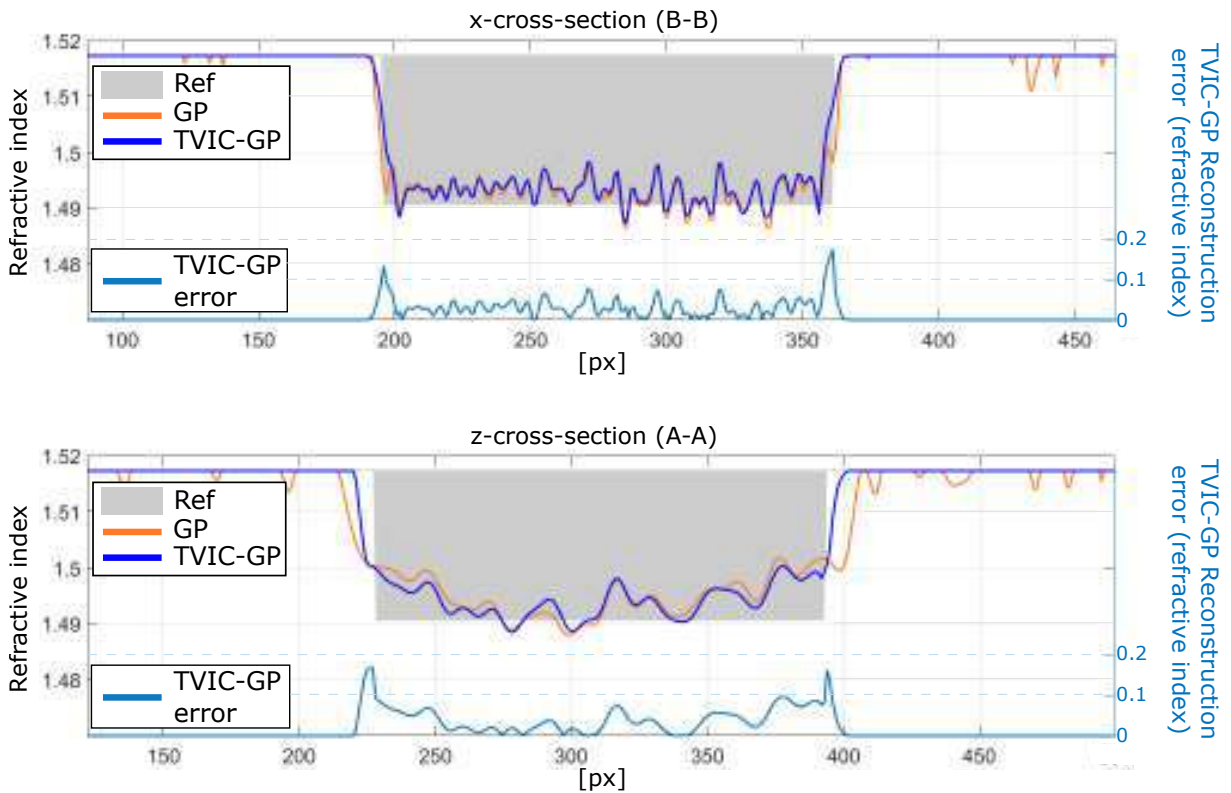


Figure 5.3: Central x - and z -cross-sections (B-B and A-A lines shown in Fig. 5.2) through the reconstructions of a micro-sphere calculated with the GP and TVIC-GP methods.

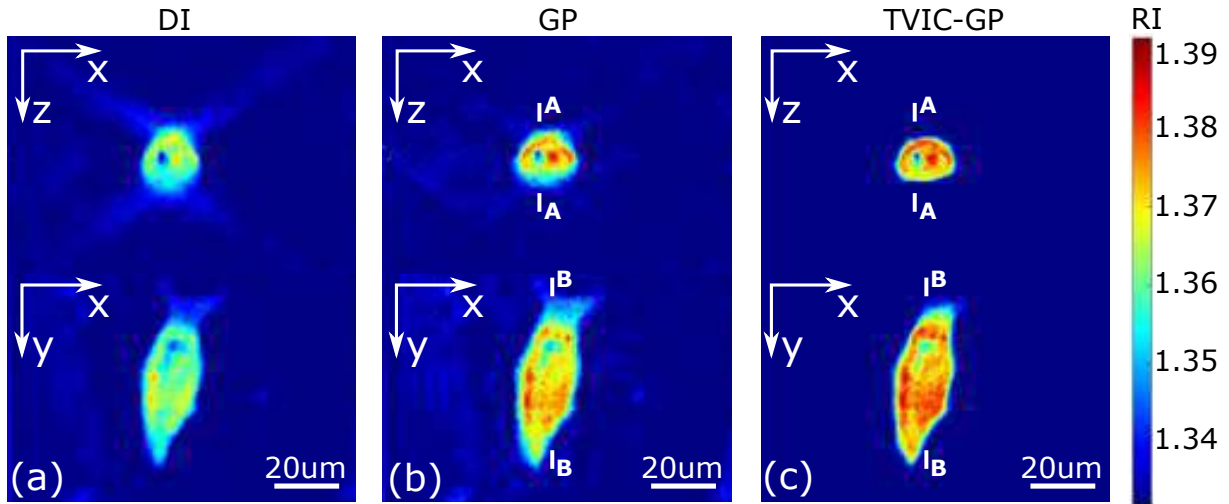


Figure 5.4: Cross-sections through the center of reconstructions of a biological cell calculated with (a) DI, (b) GP and (c) TVIC-GP procedures. All images share the same color scale.

average refractive index is too low for the fibroblast cell and in the $x - z$ cross-section, the elongation of the reconstruction is not minimized. Also, the noise surrounding the retrieved specimen is present.

GP approach provides visible correction of the reconstruction compared to the DI method. The average refractive index is higher and the LAODT artifacts surrounding the sample are weaker. However, the distortion of the reconstruction is not completely minimized and the boundaries in the $x - z$ cross-section are blurry. This result was obtained after 24 iterations.

The best results are obtained with the TVIC-GP procedure. All cross-sections have sharp boundaries, the elongation of the reconstruction is completely minimized and the average refractive index has the highest value. What is more, there are no LAODT artifacts around the investigated specimen. This result was calculated after 14 iterations. In this reconstruction, a nucleus of the cell is clearly visible in the $x - y$ cross-section as the region with lower refractive index distribution.

The above observations are confirmed by the cross-sections presented in Fig. 5.5. When analyzing these plots it is clear that when GP algorithm is supported with the TVIC strategy, the external geometry of the sample is retrieved with increased accuracy. But what is more important, the average refractive index of the reconstructed specimen is higher which is consistent with the results of numerical simulations presented in Section 3.3.2. This is the effect of the support constraint applied in every iteration of the GP algorithm. This effect is especially important near the boundaries of the reconstruction, where decreased refractive index values are characteristic to LAODT reconstructions. This is the main proof of the effectiveness of the TVIC strategy in enhancing the reconstruction quality.

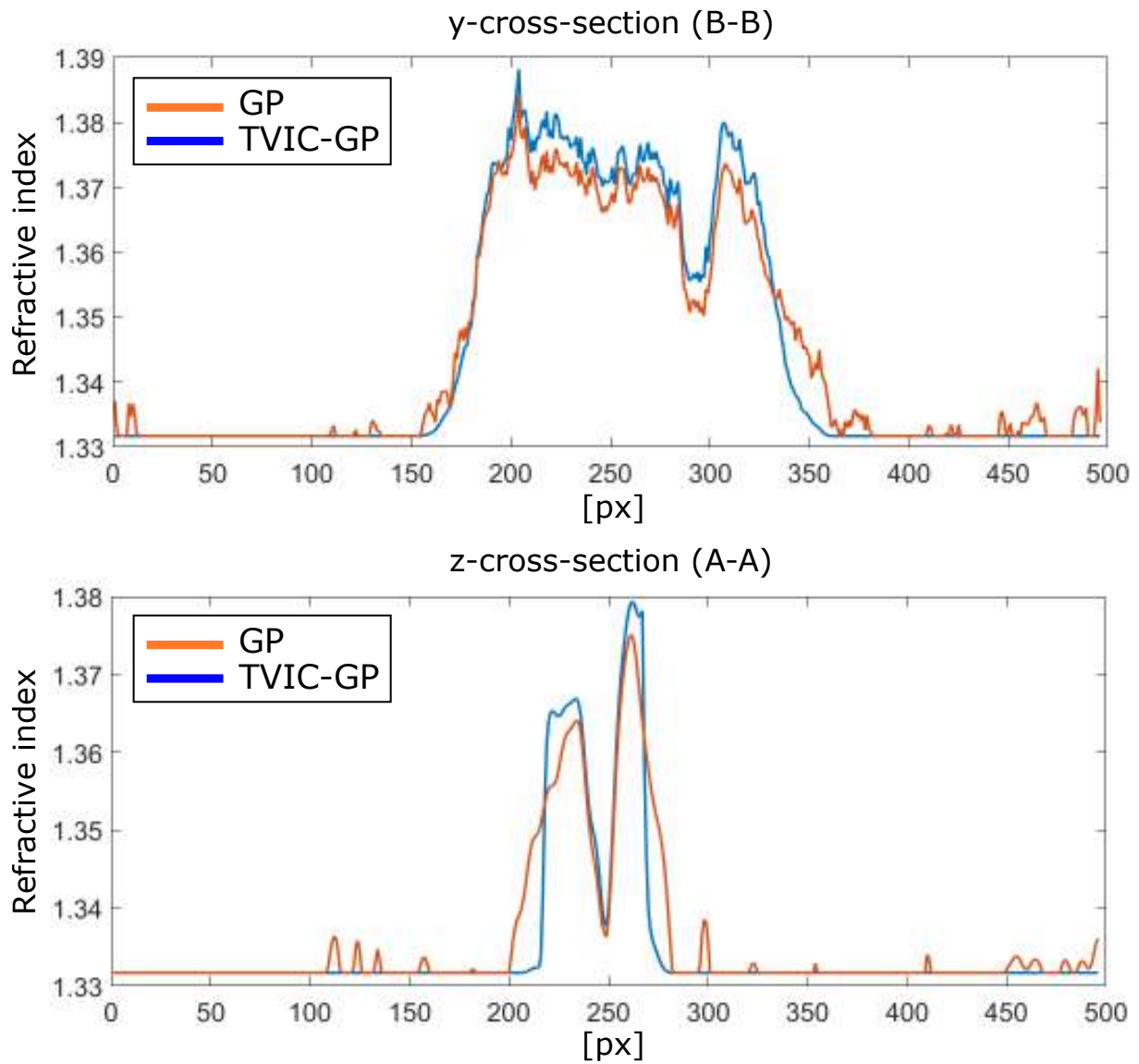


Figure 5.5: Cross-sections along B-B and A-A lines shown in Fig. 5.4 through the reconstructions of a biological cell calculated with the GP and TVIC-GP methods.

5.1.4 Conclusions

The results presented in this section prove that TVIC-GP approach gives superior results when biological micro-structures are measured. The LAODT artifacts that are usually present due to limited angular range of acquired projections are entirely corrected and the refractive index values are closer to the true refractive index distribution, as was proved by measuring the reference PMMA micro-sphere. Thus, this section verifies experimentally that it is possible to apply compressed sensing techniques, like TpV algorithm to retrieve information about objects with non-piecewise-constant refractive index distribution. **Together with the numerical analyses presented in Chapter 3, these results confirm the research hypothesis stated in the Thesis.**

Another important advantage of the TVIC-GP approach, which has not been mentioned so far, is associated with the method of storing reconstruction data by computers. When tomographic reconstruction algorithms, like DI or GP, are used with real experimental data to retrieve 3D refractive index distribution in the measurement volume, there is always some noise in the voxels surrounding the reconstructed specimen. The computer does not, by default, distinguish the sample from the background, so it has to store information about values in all voxels. Since the 3D reconstructions are relatively big matrices (e.g. $400 \times 400 \times 400$ [px] matrix consists of 64 million voxels) and information about each voxel is typically stored as a double-precision floating-point number, the size of the file with this reconstruction is large (512MB in the aforementioned case). When one takes into account the fact that usually numerous measurements of a single biological specimen are carried out, the problem with limited memory space becomes crucial. This is a problem with not only ODT, but advanced image-based measurement techniques altogether, where enormous quantities of data are produced.

When the TVIC-GP method is used to reconstruct tomographic projections, the surrounding of the retrieved refractive index distribution of an investigated specimen is noise-free. This is due to utilization of 3D mask in each iteration of the algorithm. As a result, all voxels of the 3D reconstruction that are outside the specimen have the same value - the refractive index of an immersion liquid. Such data are efficiently compressed by a computer when saved. As a result, files with significantly smaller size are obtained with the TVIC-GP method compared to alternative reconstruction approaches. As an example, the tomographic reconstruction of the micro-sphere calculated with the GP approach (Fig. 5.2(b)) occupies 161MB of disk space, whereas the one calculated with the TVIC-GP method (Fig. 5.2(c)) occupies only 15MB, while having the same size.

5.2 Focus-tunable tomography with TVIC-GP

In this section, experimental verification of F-TT is carried out. For this purpose, two samples are investigated: a reference technical object and two biological specimens. The objective of the experiments is to prove effectiveness of the described measurement process and to reconstruct 3D refractive index distributions with quasi-uniform resolution and minimized missing-frequency errors.

5.2.1 Focus-tunable tomography setup

In order to carry out experiments in this Section, the LAODT setup (Fig. 5.1) has been extended with an axial scanning module (ASM). The module is added between the beam splitter which combines the object and reference laser beams and the CCD detector. ASM consists of a 4f system with a focus-tunable lens in the Fourier plane. The focus-tunable lens is controlled electronically to shift the object plane conjugate to the detector. This allows the system to capture object projections with a different part of the specimen being in focus. The complete system is presented in Fig. 5.6.

5.2.2 Objects description

First, in order to verify the proof of concept of F-TT, the PMMA micro-sphere described in Section 5.1.2 is measured.

Next, two representatives of biological samples have been measured. The first specimen is a cell from the permanent mouse fibroblast cell line Balb/c 3T3. This cell comes from the same culture as the one measured in Section 5.1.1, however it is not the same cell.

The second biological sample, a tissue slice from a prostate cancer, was fixed in 4% formalin solution and embedded in paraffin. After a $4\mu\text{m}$ thick slice has been cut, it underwent a standard histological procedure [97], however, without the haematoxylin and eosin staining. The description of the tissue slice preparation stage and the tissue slice itself were provided by dr Ewa Skrzypek from Medical University of Warsaw. From the investigated sample, a region with red blood cells was chosen to be analyzed. The size of the measurement volume was $70\mu\text{m} \times 70\mu\text{m} \times 2\mu\text{m}$.

5.2.3 Experimental results

In the case of the micro-sphere, the conventional approach with a single focal plane produces SDOF that does not cover the whole object, thus 4 focal planes, distant from each other by $2.5\mu\text{m}$, have been used (recall Fig. 4.1). 360 projections were captured for each focal plane. Conical illumination scenario has been utilized (Fig. 2.8(a)), with the zenith angle of 52° .

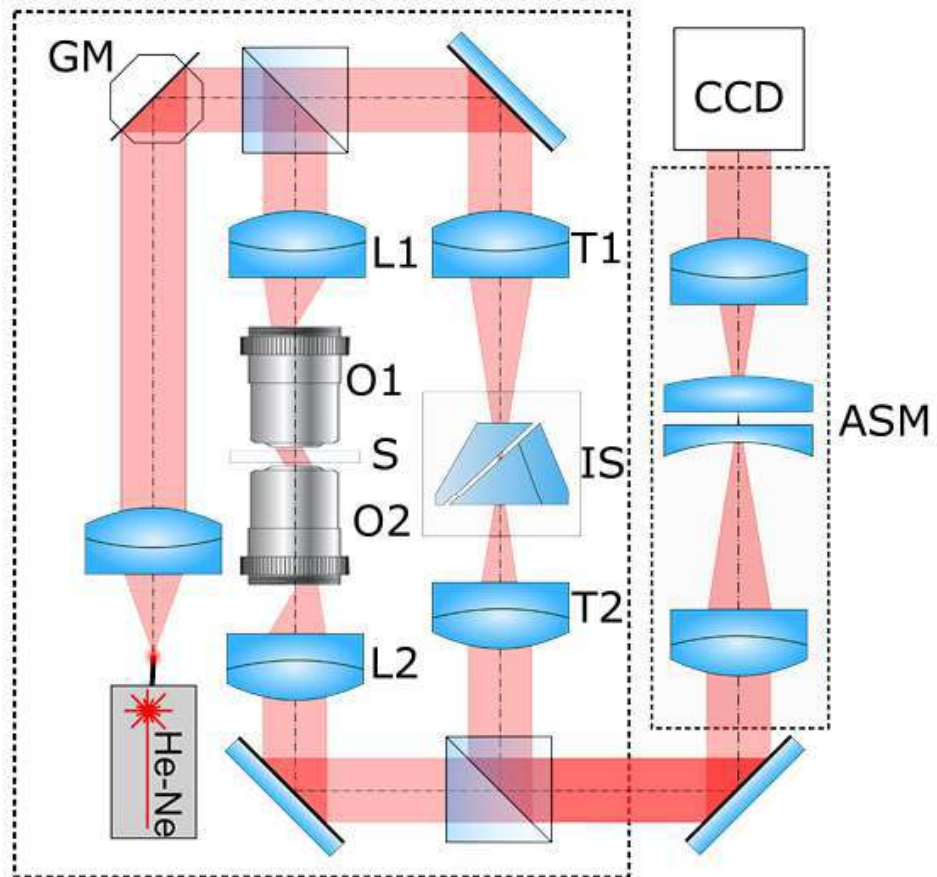


Figure 5.6: Optical setup for extended depth-of-field LAODT. GM - galvanometric mirror, L1,L2 - lenses, O1,O2 - microscope objectives, S - specimen stage, T1,T2 - collimating lenses, IS - inverting prism, ASM - axial scanning module. Author: A. Kuś [83]

Since the object is symmetric, the experiment has been designed in such way that the combined SDOFs from all focal planes covered only the upper half of the sphere. This allows to visualize the difference between focus-tunable and standard tomography by comparing the reconstruction of the top and bottom halves of this object. Despite the fact that the micro-sphere belongs to a group of piecewise-constant samples, it has been reconstructed with both approaches, presented in Fig. 3.3. This way, the full TVIC-GP procedure can be metrologically assessed and compared with the TpV algorithm.

Figure 5.7 presents the z - y cross-section (z being parallel to the optical axis) through the reconstruction calculated with the TVIC-GP procedure (according to the right part of Fig. 3.3). Lines FP1-FP4 represent 4 planes that were conjugated with the detector plane through the focus-tunable lens. The bottom half of the sphere has been reconstructed from a sinogram acquired for the focal plane FP4. The upper half of the sphere is reconstructed with higher quality, compared to the bottom half in terms of the object's retrieved geometry and refractive index distribution. This is confirmed by the vertical cross-section presented in Fig. 5.7(b), in which the upper edge of the sphere is retrieved without a drop in the refractive index level near the edge. It can be observed that in Fig. 5.7(b) the nature of noise in the cross-sections A-A and FP4 is different. This is caused by the "speckles" visible in the reconstruction, which are elongated in the z direction due to the resultant different spatial resolution in the $x - y$ plane and in the direction of the optical axis.

To quantitatively assess the obtained geometry, I compare the volume of the reconstructed object to the theoretical volume of the object under study, which is equal to $6795\mu\text{m} \pm 312\mu\text{m}^3$ (4.6% relative uncertainty). The volume of the retrieved sphere calculated based on the upper half of the sphere (which is within SDOFs) equals $7413\mu\text{m}^3$ (9% error with respect to the nominal value), while the same volume calculated based on the bottom half equals $8206\mu\text{m}^3$ (21% error with respect to the nominal value). These experimental volumes were calculated as a sum of reconstruction voxels thresholded at the immersion liquid level. The increase of volume in the case of the standard tomography is related to the distortion of 3D geometry in the areas distant from the focal plane (as shown in Fig. 5.8(c,d)). This clearly shows the advantage of the F-TT over the standard optical tomography in terms of the reconstructed geometry of the object.

Figure 5.8 presents x - y cross-sections through the reconstruction calculated with the first step of the TVIC-GP procedure: TpV algorithm (dedicated to piecewise-constant samples, like the measured micro-sphere), and with the TVIC-GP strategy. The x - y cross-sections correspond to planes FP4, FP1 and Z1, presented in Fig. 5.7. The results calculated with the TpV algorithm provide highly homogeneous and noise-free refractive index distribution, which is expected. The results obtained with the TVIC-GP procedure contain more noise due to lack of piecewise-constant regularization utilized during retrieval of the refractive index distribution.

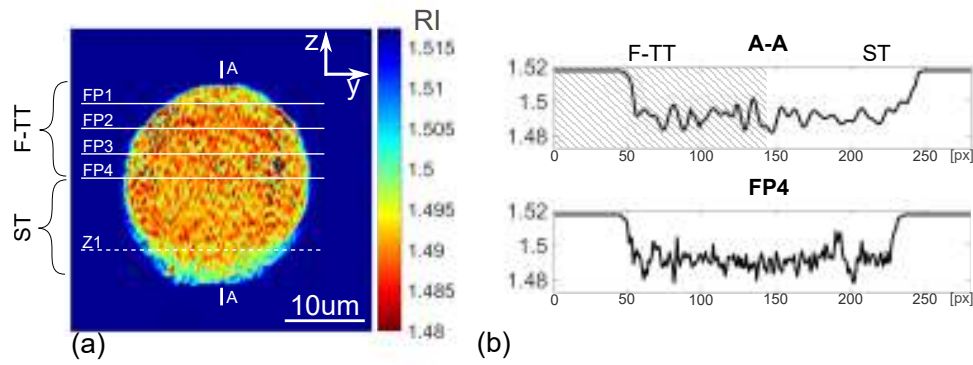


Figure 5.7: Tomographic reconstruction of the $23.5\mu\text{m}$ PMMA micro-sphere calculated with the TVIC-GP procedure: (a) z - y cross-section through a 3D reconstruction; (b) Vertical and horizontal 1D cross-sections; FP1-FP4 - positions of focal planes, Z1 - plane which is compared with FP1 plane in Fig.5.8, ST - standard tomography, F-TT - focus-tunable tomography. Note the inverted colorbar. [83]

The difference between Fig. 5.8(d) and Fig. 5.8(f) shows the advantages of utilizing F-TT. Ideally, both cross-sections should be identical, since they are taken from planes that are equally distant from the central FP4 plane. However, since the cross-section presented in Fig. 5.8(f) is extracted from the part of the reconstruction which is within the SDOF, its geometry and refractive index distribution are of significantly higher quality. This is confirmed by Fig. 5.8(g), in which one can notice that, unlike Z1 plane, the FP1 plane matches the theoretical geometry and the refractive index value of the micro-sphere. The noise present in the results calculated with the TVIC-GP method can be significantly limited by applying $3\times 3\times 3$ median filtering (not applied here).

Similarly to the technical object, in the case of biological samples the approach with a single focal plane produces a SDOF that covers only a thin fragment of the investigated object. Thus, multiple focal planes were used, and when SDOFs from all focal planes were combined, they covered the whole volume of the sample. The projections have been reconstructed with a full TVIC-GP procedure, dedicated to biological micro-objects.

The first biological sample, the fibroblast cell, has been measured with 4 focal planes, separated from each other by $1.7\mu\text{m}$. For each focal plane, 360 projections were acquired using the conical illumination scenario, with the illumination zenith angle of 47.7° .

Figure 5.9 presents the comparison between reconstructions calculated from one focal plane (Fig. 5.9(a), standard tomography case) and 4 focal planes (Fig. 5.9(b), F-TT case). Fig. 5.9(c) shows the x - y cross-section through the FP3, which is common for both reconstructions. The advantage of F-TT is visible when one analyzes the details of both reconstructions, especially the structure with the high refractive index, which might be associated with cell division, and a pseudopod, marked with red arrows. When 4 focal planes are utilized, the high refractive index

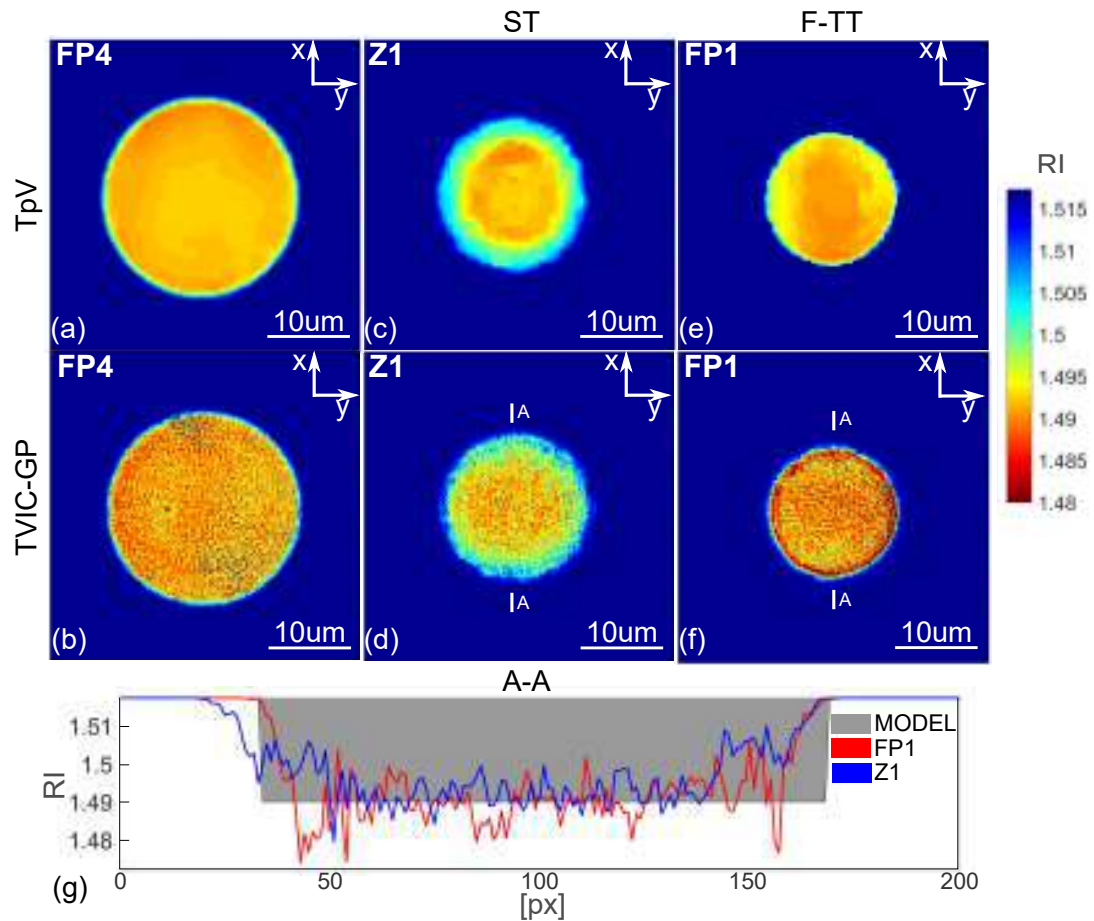


Figure 5.8: Visualization of the effect of the F-TT on 3D reconstruction of the PMMA microsphere reconstructed with (a,c,e) TpV algorithm and (b,d,e) TVIC-GP procedure. (a,b) central x - y cross-sections - FP4 plane in Fig. 5.7; (c,d) Z1 plane from Fig. 5.7 which is distant from central plane by $-7.5\mu\text{m}$; (e,f) FP1 plane from Fig. 5.7 which is distant from the FP4 plane by $7.5\mu\text{m}$; (g) 1D cross-sections through (d) and (f) compared with the reference, theoretic refractive index distribution. ST - standard tomography with 1 focal plane, F-TT - focus-tunable tomography. Note the inverted colorbar. [83]

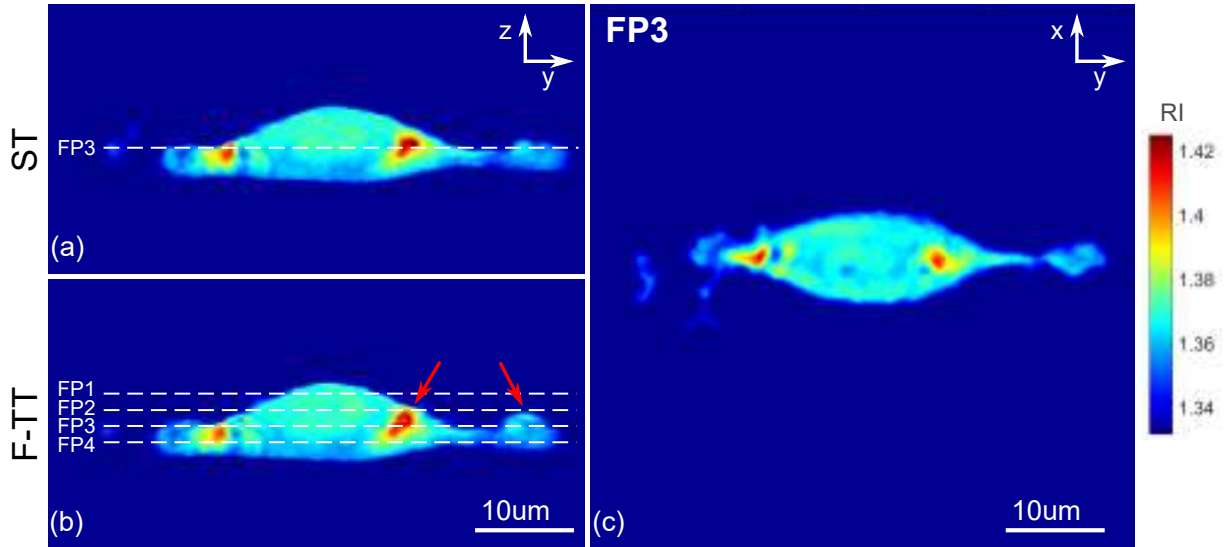


Figure 5.9: TVIC-GP reconstructions of the 3T3 cell in: (a) standard tomography (ST) case with 1 focal plane, (b) focus-tunable tomography (F-TT) case with 4 focal planes; (c) x - y cross-section through the cell. FP1-FP4 - focal planes. [83]

structure becomes larger and adopts more regular shape. Also, a part of the pseudopod becomes visible, which results in a larger pseudopod with more distinct boundaries.

The second biological micro-object is the tissue slice from a prostate cancer. 3 focal planes were uniformly distributed within the $2\mu\text{m}$ thick measurement volume. 360 projections were acquired for each focal plane using the conical illumination scenario, with the illumination zenith angle of 47.7° . From the whole tissue sample, a region with well-defined red blood cells surrounded by cellular debris has been chosen as a region of interest.

Figure 5.10 shows comparison between the tomographic reconstruction calculated for one focal plane, which is in the middle of the $2\mu\text{m}$ thick object volume (standard tomography case), and the one calculated for 3 focal planes (F-TT case). The presented x - y cross-sections are planes that are distant from the center of the measurement volume by $0.6\mu\text{m}$. In the case of the F-TT, the biological micro-structures are sharply reconstructed, whereas in the standard reconstruction this plane suffers from reduced resolution. Also, the refractive index values are, by average, higher in the stitched reconstruction. It should be noted, however, that such differences are present in x - y planes distant from the center of the reconstruction only.

5.2.4 Conclusions

The described F-TT approach has been combined with the TVIC-GP reconstruction method. Tests conducted on the reference object confirmed that this combined technique guarantees both quasi-uniform resolution in the whole measurement volume and minimization of errors that are present due to limited angular range of acquired projections. It has been shown that both

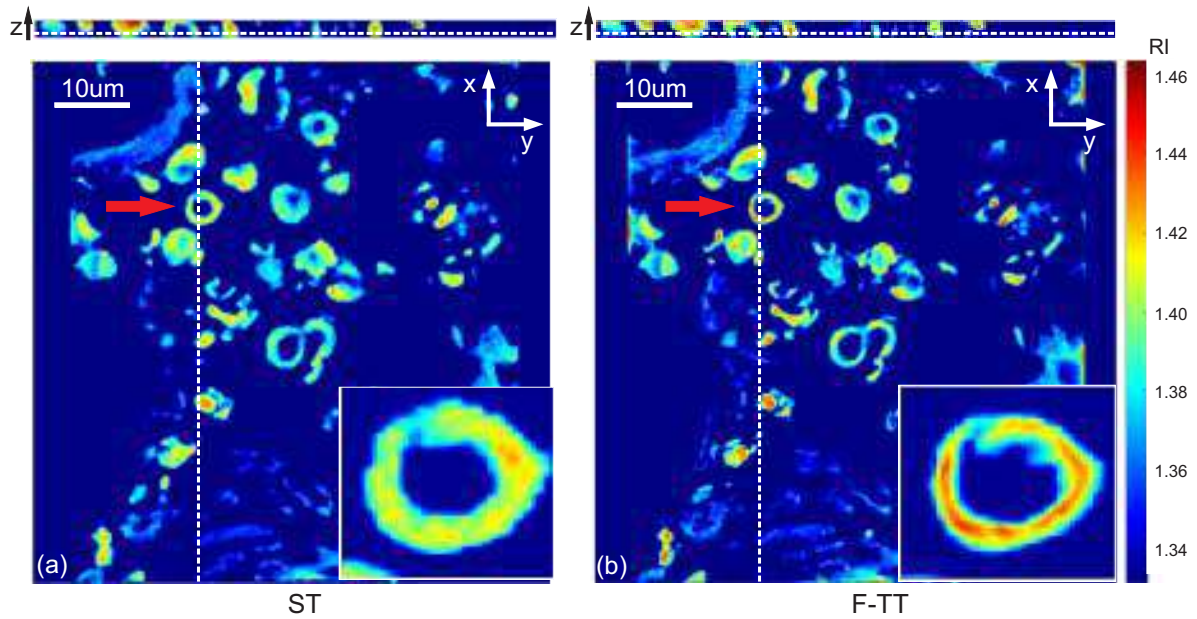


Figure 5.10: Comparison of the standard tomography (ST) reconstruction of the tissue sample calculated for one focal plane with the focus-tunable tomography (F-TT) reconstruction calculated for three different focal planes; (a) x - y and z - y cross-sections of the TVIC-GP reconstruction calculated for one focal plane. The x - y cross-section shown presents a plane distant from the focal plane (which is in the center of the measurement volume) by $0.6\mu m$. The magnified structure is the red blood cell marked with red arrow. (b) The same cross-sections of the reconstruction calculated for three focal planes, uniformly distributed in the measurement volume. [83]

refractive index distribution and external geometry of an investigated sample are reconstructed with increased quality.

The quasi-uniform resolution along z -axis, achieved in this system, extends the range of cells that can be investigated with high accuracy. What is more, the reconstructions of a tissue sample show that this approach is useful even when the thickness of an investigated sample is small ($\sim 2\mu m$) but the Rytov condition is violated by the strong scattering properties of the tissue. The capability of this method to conduct phase analysis of tissue slices without the necessity of staining or labeling, makes the extended-depth-of-field LAODT a very promising tool in new digital diagnostic methods in the field of histology.

The main disadvantage of this method is associated with the amount of data that has to be captured. If N focal planes are utilized in the measurement process, $N \times S$ data has to be captured, where S is the size of a sinogram for a single focal plane. This is a time-consuming process both for the projection-acquisition and reconstruction stages. Currently, it takes 15 seconds per focal plane to acquire 180 projections, 10 minutes to preprocess the data and 10 minutes per focal plane to reconstruct the data with the TVIC-GP procedure on the computer with parameters given at the beginning of this section. The method may be sped up by using a faster camera (currently 14fps). What is more, the hologram preprocessing may be enhanced by using CUDA and since the fringe orientation may be easily controlled in the presented setup, other faster preprocessing approaches may be used [98]. However, in terms of presented solution, the main direction of further study is limitation of data acquired for each focal plane.

Chapter 6

Conclusions and future trends

6.1 Conclusions

The Main Objective stated in the Thesis has been accomplished through presentation of a full processing path that can be applied to the limited angle optical diffraction tomography (LAODT) data when biological specimens are measured, including the preprocessing steps that have to be carried out. However, the key part is the novel reconstruction strategy, called Total Variation Iterative Constraint (TVIC). This procedure is, according to my knowledge, the first tomographic reconstruction approach dedicated to biological micro-samples. By utilizing the total p-variation (TpV) minimization, TVIC calculates reconstructions of the analyzed specimens that are free from the LAODT artifacts. However, despite the fact that TpV minimization is used, the non-piecewise-constant refractive index distribution of biological objects under study is preserved in the reconstructions, which confirms the hypothesis stated in the Thesis. This is thanks to an innovative way of using the TpV minimization. In TVIC, this regularization mechanism is used to retrieve the external geometry only. The retrieval of the refractive index distribution of internal structures is conducted with the tomographic reconstruction method of choice, e.g. Gerchberg-Papoulis (GP) algorithm which dominates in the research literature regarding LAODT.

The numerical analyses presented in the Thesis proved that GP algorithm supported with the TVIC strategy converges to a solution when noise-free input data are used. The same tests have been repeated for noisy data and the reconstructions show that the TVIC-GP method gives significantly better-quality results compared to GP algorithm which is not supported by the TVIC strategy. The TVIC-GP gives also better reconstructions compared to the algorithms which directly implement TpV minimization procedure since these methods require constant-piecewise refractive index distribution of investigated specimens and can be successfully applied only to a very narrow group of bio-samples, like red blood cells. It has also been proven that the number

of acquired object projections can be significantly limited without loss of the reconstruction quality. What is more, a procedure for clearing the reconstruction from unwanted structures has been presented. Through a dedicated processing scheme, this procedure removes information from original sinograms about unwanted structures to enhance the effectiveness of the support constraint in the GP algorithm.

The above numerical tests have been experimentally verified by performing measurements of a reference PMMA micro-sphere and biological cells. The results show that TVIC-GP gives superior results compared to alternative tomographic reconstruction approaches like DI or GP. The refractive index values in the reconstructions are more correct and the elongation in the direction of an optical axis is removed. As far as biological specimens are concerned, this results in better visibility of internal structures. What is more, it has been shown that the files with reconstructions calculated with the TVIC-GP method are at least 10 times smaller in size than the ones calculated with other tomographic procedures.

The numerical simulations and experimental measurements carried out on a reference PMMA micro-sphere show that the reconstruction error, understood as the maximum difference between the TVIC reconstruction and reference data, is not higher than 0.01, which was the requirement stated in the "Aim of Thesis". This condition is violated only where steep boundaries of an investigated sample are present. Correction of this phenomenon will be the objective of my future works.

To accomplish the secondary task stated in the Thesis, which is increasing the depth-of-field of LAODT, a procedure called focus-tunable tomography (F-TT) has been proposed. The method includes hardware modifications, namely insertion of an electric focus-tunable lens in front of a CCD detector used in LAODT. This allows the system to acquire a set of object sinograms with different parts of the object being in focus. What is more, a novel processing strategy has been proposed which includes independent reconstructions of sinograms with TVIC-GP and stitching of the parts of reconstructions which are within the synthetic depth-of-field. As a result the refractive index distribution of an analyzed sample with enhanced depth-of-field is obtained. The experimental verification proved that this approach can be successfully applied to investigation of biological samples like cells or tissue slices to increase the overall quality.

To conclude, the most important results of my research are:

- Tomographic reconstruction strategy, called TVIC, which is dedicated to tomographic investigation of biological micro-samples with non-piecewise-constant refractive index distribution [59, 77, 80];
- Method of clearing the tomographic reconstruction from unwanted inclusions, like dust particles, cellular debris and others to enhance effectiveness of the spatial support constraint in the iterative reconstruction.

- Method of increasing the depth-of-field in LAODT [83, 93], which involved:
 - Method of acquiring tomographic projections with different parts of an investigated sample being in focus, by introducing a focus-tunable lens into the LAODT optical system;
 - Data processing procedure, including reconstruction and stitching algorithms, which results in the tomographic reconstruction of an investigated specimen with extended depth-of-field.

From the application point of view, I presented promising results of the tomographic and holographic analysis of different biological specimens, including fibroblasts [65, 83], myoblasts [64, 80, 94], tissue slices [83, 93], cancer cells [70] and bacterial colonies [15].

6.2 Future works

The research tasks that have to be addressed in the nearest future include:

- Decreasing the computation time for TVIC-GP through further utilization of parallel computing with the CUDA technology.
- Optimization of the calculation time when F-TT is conducted with the TVIC-GP approach. In F-TT only a fragment of each independent reconstruction is used to create the final result with extended depth-of-field. Region-of-interest tomography [99] is a promising technique which could potentially speed-up the reconstruction calculation process.
- Improvement of the quality of tomographic reconstructions with inner structures that have steep boundaries.

The long-term objectives are:

- Development of a method for visualization of the calculated 3D reconstructions that would be coherent with the expectations of the medical and biological communities.
- Development of the data processing strategy for the measurement of large histological tissue slices.
- Development of tomographic reconstruction procedures that take higher order scattering into account. This is especially important when histological tissue slices are to be investigated.
- Systematic work with the medical community on the interpretation of the results obtained with with LAODT systems.

- Development of numerical procedures utilizing deep learning techniques for the support of diagnosis based on the results obtained with LAODT setups.
- Development of a commercial version of the LAODT setup with the team of collaborators and implementation of the setup in medical institutions.

References

- [1] *WHO Cancer Fact Sheet*. <http://www.who.int/mediacentre/factsheets/fs297/en/>. (accessed 13.11.2017). 2017.
- [2] P. Lewis. The US cancer moonshot—A need and opportunity for primary care participation and collaboration, *Eur. J. Cancer Care* **26**, no. 3 (2017).
- [3] *EU Key Research Areas*. <https://ec.europa.eu>. (accessed 27.09.2017). 2017.
- [4] *Phase Holographic Imaging*. <http://phiab.se/>. (accessed 17.12.2017). 2017.
- [5] *3D Holographic Microscopy*. <http://tomocube.com>. (accessed 28.07.2017). 2016.
- [6] *The 3D Cell Explorer*. <http://nanolive.ch>. (accessed 28.07.2017). 2016.
- [7] D. Jin, R. Zhou, Z. Yaqoob, and P. T. So. Tomographic phase microscopy: principles and applications in bioimaging, *JOSA B* **34**, no. 5 (2017), B64–B77.
- [8] A. H. Delaney and Y. Bresler. Globally convergent edge-preserving regularized reconstruction: an application to limited-angle tomography, *IEEE Trans. Image Process.* **7**, no. 2 (1998), pp. 204–221.
- [9] D. Verhoeven. Limited-data computed tomography algorithms for the physical sciences, *Appl. Opt.* **32**, no. 20 (1993), pp. 3736–3754.
- [10] K. M. Hanson and G. W. Wecksung. Bayesian approach to limited-angle reconstruction in computed tomography, *JOSA* **73**, no. 11 (1983), pp. 1501–1509.
- [11] F. Zernike. Phase contrast, a new method for the microscopic observation of transparent objects, *Physica* **9**, no. 7 (1942), pp. 686–698.
- [12] W. Lang. *Nomarski differential interference-contrast microscopy*. Oberkochen, Carl Zeiss, 1982.
- [13] P. Ferraro, A. Wax, and Z. Zalevsky. *Coherent light microscopy: imaging and quantitative phase analysis*. Vol. 46. Springer Science & Business Media, 2011.
- [14] J. Garcia-Sucerquia, W. Xu, S. K. Jericho, P. Klages, M. H. Jericho, and H. J. Kreuzer. Digital in-line holographic microscopy, *Appl. Opt.* **45**, no. 5 (2006), pp. 836–850.

- [15] I. Buzalewicz, M. Kujawińska, W. **Krauze**, and H. Podbielska. **Novel Perspectives on the Characterization of Species-Dependent Optical Signatures of Bacterial Colonies by Digital Holography**, *PLOS ONE* **11**, no. 3 (2016), e0150449.
- [16] E. Sánchez-Ortiga, A. Doblas, G. Saavedra, M. Martínez-Corral, and J. Garcia-Sucerquia. Off-axis digital holographic microscopy: practical design parameters for operating at diffraction limit, *Appl. Opt.* **53**, no. 10 (2014), pp. 2058–2066.
- [17] J. Min, B. Yao, S. Ketelhut, C. Engwer, B. Greve, and B. Kemper. Simple and fast spectral domain algorithm for quantitative phase imaging of living cells with digital holographic microscopy, *Opt. Lett.* **42**, no. 2 (2017), pp. 227–230.
- [18] B. Kemper, S. Kosmeier, P. Langehanenberg, G. von Bally, I. Bredebusch, W. Domschke, and J. Schnekenburger. Integral refractive index determination of living suspension cells by multifocus digital holographic phase contrast microscopy, *J. Biomed. Opt.* **12**, no. 5 (2007), pp. 054009–054009.
- [19] D. Carl, B. Kemper, G. Wernicke, and G. v. Bally. Parameter-optimized digital holographic microscope for high-resolution living-cell analysis, *Appl. Opt.* **43**, no. 36 (2004), pp. 6536–6544.
- [20] M. Takeda, H. Ina, and S. Kobayashi. Fourier-transform method of fringe-pattern analysis for computer-based topography and interferometry, *J. Opt. Soc. Am.* **72**, no. 1 (Jan. 1982), pp. 156–160.
- [21] M. Kujawinska and J. Wojciak. “Spatial-carrier phase-shifting technique of fringe pattern analysis”, *Industrial Applications of Holographic and Speckle Measuring Techniques*. Vol. 1508. International Society for Optics and Photonics. 1991, pp. 61–68.
- [22] C. Remmersmann, S. Stürwald, B. Kemper, P. Langehanenberg, and G. von Bally. Phase noise optimization in temporal phase-shifting digital holography with partial coherence light sources and its application in quantitative cell imaging, *Appl. Opt.* **48**, no. 8 (2009), pp. 1463–1472.
- [23] D. Bettenworth, A. Bokemeyer, C. Poremba, N. S. Ding, S. Ketelhut, P. Lenz, and B. Kemper. Quantitative phase microscopy for evaluation of intestinal inflammation and wound healing utilizing label-free biophysical markers. *HH* (2017), pp. 11937–11937.
- [24] B. Kemper, J. Schnekenburger, and S. Ketelhut. “Chemotaxis of cancer cells in three-dimensional environment monitored label-free by quantitative phase digital holographic microscopy”, *Quantitative Phase Imaging III*. Vol. 10074. International Society for Optics and Photonics. 2017, p. 1007412.
- [25] X. Ou, R. Horstmeyer, C. Yang, and G. Zheng. Quantitative phase imaging via Fourier ptychographic microscopy, *Opt. Lett.* **38**, no. 22 (2013), pp. 4845–4848.

- [26] G. Zheng, R. Horstmeyer, and C. Yang. Wide-field, high-resolution Fourier ptychographic microscopy, *Nat. Photonics* **7**, no. 9 (2013), pp. 739–745.
- [27] Z. Wang, L. Millet, M. Mir, H. Ding, S. Unarunotai, J. Rogers, M. U. Gillette, and G. Popescu. Spatial light interference microscopy (SLIM), *Opt. Express* **19**, no. 2 (2011), pp. 1016–1026.
- [28] M. Mir, Z. Wang, Z. Shen, M. Bednarz, R. Bashir, I. Golding, S. G. Prasanth, and G. Popescu. Optical measurement of cycle-dependent cell growth, *PNAS* **108**, no. 32 (2011), pp. 13124–13129.
- [29] B. Bhaduri, D. Wickland, R. Wang, V. Chan, R. Bashir, and G. Popescu. Cardiomyocyte imaging using real-time spatial light interference microscopy (SLIM), *PLoS one* **8**, no. 2 (2013), e56930.
- [30] Z. Wang, D. L. Marks, P. S. Carney, L. J. Millet, M. U. Gillette, A. Mihi, P. V. Braun, Z. Shen, S. G. Prasanth, and G. Popescu. Spatial light interference tomography (SLIT), *Opt. Express* **19**, no. 21 (2011), pp. 19907–19918.
- [31] V. Lauer. New approach to optical diffraction tomography yielding a vector equation of diffraction tomography and a novel tomographic microscope, *J. Microsc.* **205**, no. 2 (2002), pp. 165–176.
- [32] M. Kujawińska, W. Krauze, A. Kus, J. Kostencka, T. Kozacki, B. Kemper, and M. Dudek. **Problems and Solutions in 3-D Analysis of Phase Biological Objects by Optical Diffraction Tomography**, *Int. J. Optomechatronics* **8**, no. 4 (2014), pp. 357–372.
- [33] J. Martinez-Carranza, K. Falaggis, M. Jozwik, and T. Kozacki. Comparison of phase retrieval techniques based on the transport of intensity equation using equally and unequally spaced plane separation criteria, *Proc. SPIE* **9204** (2014), 92040G.
- [34] M. A. Herráez, D. R. Burton, M. J. Lalor, and M. A. Gdeisat. Fast two-dimensional phase-unwrapping algorithm based on sorting by reliability following a noncontinuous path, *Appl. Opt.* **41**, no. 35 (Dec. 2002), pp. 7437–7444.
- [35] J. M. Bioucas-Dias and G. Valadao. Phase unwrapping via graph cuts, *IEEE Trans. Image Process.* **16**, no. 3 (2007), pp. 698–709.
- [36] M. Kujawinska, V. Parat, M. Dudek, B. Siwicki, S. Wojcik, G. Baethge, and B. Dahmani. Interferometric and tomographic investigations of polymer microtips fabricated at the extremity of optical fibers, *Proc. SPIE* **8494** (2012), p. 849404.
- [37] M. Dudek, M. Kujawinska, V. Parat, G. Baethge, A. Michalska, B. Dahmani, and H. Ottevaere. Tomographic and numerical studies of polymer bridges between two optical fibers for telecommunication applications, *Opt. Eng.* **53**, no. 1 (2014), pp. 016113–016113.

- [38] J. Kostencka, T. Kozacki, A. Kuś, and M. Kujawińska. Accurate approach to capillary-supported optical diffraction tomography, *Opt. Express* **23**, no. 6 (2015), pp. 7908–7923.
- [39] A. Kuś, M. Dudek, B. Kemper, M. Kujawińska, and A. Vollmer. Tomographic phase microscopy of living three-dimensional cell cultures, *J. Biomed. Opt.* **19**, no. 4 (2014), pp. 046009–046009.
- [40] K. Kim, J. Yoon, and Y. Park. Simultaneous 3D visualization and position tracking of optically trapped particles using optical diffraction tomography, *Optica* **2**, no. 4 (2015), pp. 343–346.
- [41] L. Zehnder. Ein neuer interferenzrefraktor, *Z. Instrum.* **11** (1891), pp. 275–285.
- [42] Y. Cotte, F. Toy, P. Jourdain, N. Pavillon, D. Boss, P. Magistretti, P. Marquet, and C. Depeursinge. Marker-free phase nanoscopy, *Nat. Photonics* **7**, no. 2 (2013), pp. 113–117.
- [43] Y. Sung, W. Choi, C. Fang-Yen, K. Badizadegan, R. R. Dasari, and M. S. Feld. Optical diffraction tomography for high resolution live cell imaging, *Opt. Express* **17**, no. 1 (2009), pp. 266–277.
- [44] J. Kostencka, T. Kozacki, A. Kuś, B. Kemper, and M. Kujawińska. Holographic tomography with scanning of illumination: space-domain reconstruction for spatially invariant accuracy, *Biomed. Opt. Express* **7**, no. 10 (2016), pp. 4086–4101.
- [45] K. Kim, H. Yoon, M. Diez-Silva, M. Dao, R. R. Dasari, and Y. Park. High-resolution three-dimensional imaging of red blood cells parasitized by *Plasmodium falciparum* and in situ hemozoin crystals using optical diffraction tomography, *J. Biomed. Opt.* **19**, no. 1 (2014), pp. 011005–011005.
- [46] Y. Kim, H. Shim, K. Kim, H. Park, S. Jang, and Y. Park. Profiling individual human red blood cells using common-path diffraction optical tomography, *Sci. Rep.* **4**, no. 6659 (2014), pp. 1–7.
- [47] Y. Kim, H. Shim, K. Kim, H. Park, J. H. Heo, J. Yoon, C. Choi, S. Jang, and Y. Park. Common-path diffraction optical tomography for investigation of three-dimensional structures and dynamics of biological cells, *Opt. Express* **22**, no. 9 (2014), pp. 10398–10407.
- [48] K. Kim, Z. Yaqoob, K. Lee, J. W. Kang, Y. Choi, P. Hosseini, P. T. So, and Y. Park. Diffraction optical tomography using a quantitative phase imaging unit, *Opt. Lett.* **39**, no. 24 (2014), pp. 6935–6938.
- [49] P. C. Hansen. *Discrete inverse problems: insight and algorithms*. SIAM, 2010.
- [50] J. Hsieh. *Computed tomography: principles, design, artifacts, and recent advances*. Vol. 114. SPIE press, 2003.

- [51] P. Müller, M. Schürmann, and J. Guck. The Theory of Diffraction Tomography, *arXiv* no. 1507.00466 (July 2015).
- [52] A. C. Kak and M. Slaney. *Principles of computerized tomographic imaging*. SIAM, 2001.
- [53] T. M. Habashy, R. W. Groom, and B. R. Spies. Beyond the Born and Rytov approximations: A nonlinear approach to electromagnetic scattering, *J. Geophys. Res.* **98**, no. B2 (1993), pp. 1759–1775.
- [54] J. W. Goodman. *Introduction to Fourier optics*. Roberts and Company Publishers, 2005.
- [55] A. Devaney. Inverse-scattering theory within the Rytov approximation, *Opt. Lett.* **6**, no. 8 (1981), pp. 374–376.
- [56] K. Kim, J. Yoon, S. Shin, S. Lee, S.-A. Yang, and Y. Park. Optical diffraction tomography techniques for the study of cell pathophysiology, *J. Biomed. Photonics Eng.* **2**, no. 2 (2016).
- [57] A. Kuś. *Aktywny tomograf holograficzny do pomiaru mikroobektów biologicznych*. Oficyna Wydawnicza PW, Warszawa, 2017.
- [58] C. Fang-Yen, W. Choi, Y. Sung, C. J. Holbrow, R. R. Dasari, and M. S. Feld. Video-rate tomographic phase microscopy, *J. Biomed. Opt.* **16**, no. 1 (2011), pp. 011005–011005.
- [59] W. Krauze, A. Kuś, and M. Kujawinska. **Limited-angle hybrid optical diffraction tomography system with total-variation-minimization-based reconstruction**, *Opt. Eng.* **54**, no. 5 (2015), pp. 054104–054104.
- [60] M. Debailleul, V. Georges, B. Simon, R. Morin, and O. Haeberlé. High-resolution three-dimensional tomographic diffractive microscopy of transparent inorganic and biological samples, *Opt. Lett.* **34**, no. 1 (2009), pp. 79–81.
- [61] S. Shin, K. Kim, J. Yoon, and Y. Park. Active illumination using a digital micromirror device for quantitative phase imaging, *Opt. Lett.* **40**, no. 22 (Nov. 2015), pp. 5407–5410.
- [62] W.-H. Lee. Binary computer-generated holograms, *Appl. Opt.* **18**, no. 21 (Nov. 1979), pp. 3661–3669.
- [63] X. Chen, B.-b. Yan, F.-j. Song, Y.-q. Wang, F. Xiao, and K. Alameh. Diffraction of digital micromirror device gratings and its effect on properties of tunable fiber lasers, *Appl. Opt.* **51**, no. 30 (2012), pp. 7214–7220.
- [64] A. Kuś, W. Krauze, and M. Kujawińska. **Active limited-angle tomographic phase microscope**, *J. Biomed. Opt.* **20**, no. 11 (2015), p. 111216.

- [65] M. Kujawinska, A. Kus, W. **Krauze**, and T. Lekszycki. “**Limited Angle Optical Diffraction Tomography With Generalized Total Variation Iterative Constraint Algorithm**”, *Digital Holography and Three-Dimensional Imaging*. Optical Society of America. 2016, DW2H-1.
- [66] H. Stark, J. W. Woods, I. Paul, and R. Hingorani. An investigation of computerized tomography by direct Fourier inversion and optimum interpolation, *IEEE Trans. Biomed. Eng.* no. 7 (1981), pp. 496–505.
- [67] R. Gordon. A tutorial on ART (algebraic reconstruction techniques), *IEEE Trans. Nucl. Sci.* **21**, no. 3 (1974), pp. 78–93.
- [68] A. H. Andersen and A. C. Kak. Simultaneous algebraic reconstruction technique (SART): a superior implementation of the ART algorithm, *Ultrason. Imaging* **6**, no. 1 (1984), pp. 81–94.
- [69] J. Trampert and J.-J. Leveque. Simultaneous iterative reconstruction technique: physical interpretation based on the generalized least squares solution, *J. Geophys. Res.* **95**, no. B8 (1990), pp. 12553–12559.
- [70] W. **Krauze** and M. Kujawińska. **Limited-angle tomography applied to biological objects**, *Photonics Lett. Pol.* **5**, no. 4 (2013), pp. 149–151.
- [71] A. Kuś, W. **Krauze**, M. Kujawinska, and M. Filipiak. **Limited-angle hybrid diffraction tomography for biological samples**, *Proc. SPIE* **9132** (2014), 91320O.
- [72] E. Y. Sidky, C.-M. Kao, and X. Pan. Accurate image reconstruction from few-views and limited-angle data in divergent-beam CT, *J. X-ray Sci. Technol.* **14**, no. 2 (2006), pp. 119–139.
- [73] B. K. Natarajan. Sparse approximate solutions to linear systems, *SIAM J. Comput.* **24**, no. 2 (1995), pp. 227–234.
- [74] X. Jin, L. Li, Z. Chen, L. Zhang, and Y. Xing. “Anisotropic total variation for limited-angle CT reconstruction”, *Nuclear Science Symposium Conference Record (NSS/MIC), 2010 IEEE*. IEEE. 2010, pp. 2232–2238.
- [75] E. Y. Sidky, J. H. Jørgensen, and X. Pan. Convex optimization problem prototyping for image reconstruction in computed tomography with the Chambolle–Pock algorithm, *Phys. Med. Biol.* **57**, no. 10 (2012), p. 3065.
- [76] A. Chambolle and T. Pock. A first-order primal-dual algorithm for convex problems with applications to imaging, *J. Math. Imaging Vis.* **40**, no. 1 (2011), pp. 120–145.
- [77] W. **Krauze**, P. Makowski, and M. Kujawińska. **Total variation iterative constraint algorithm for limited-angle tomographic reconstruction of non-piecewise-constant structures**, *Proc. SPIE* **9526** (2015), 95260Y.

- [78] A. Kuś, W. Krauze, and M. Kujawińska. **Limited-angle holographic tomography with optically controlled projection generation**, *Proc. SPIE* **9330** (2015), p. 933007.
- [79] Z. Wang and A. C. Bovik. A universal image quality index, *IEEE Signal Process. Lett.* **9**, no. 3 (2002), pp. 81–84.
- [80] W. Krauze, P. Makowski, M. Kujawińska, and A. Kuś. **Generalized total variation iterative constraint strategy in limited angle optical diffraction tomography**, *Opt. Express* **24**, no. 5 (2016), pp. 4924–4936.
- [81] J. Lim, K. Lee, K. H. Jin, S. Shin, S. Lee, Y. Park, and J. C. Ye. Comparative study of iterative reconstruction algorithms for missing cone problems in optical diffraction tomography, *Opt. Express* **23**, no. 13 (2015), pp. 16933–16948.
- [82] P.-C. Lee. Multigrid iterative method with adaptive spatial support for computed tomography reconstruction from few-view data, *Proc. SPIE* **9033** (2014), p. 90338.
- [83] W. Krauze, A. Kuś, D. Śladowski, E. Skrzypek, and M. Kujawińska. **Reconstruction method for extended depth-of-field optical diffraction tomography**, *Methods*, doi: 10.1016/j.ymeth.2017.10.005 (2017).
- [84] N. Otsu. A threshold selection method from gray-level histograms, *IEEE Trans. Syst. Man Cybern.* **9**, no. 1 (1979), pp. 62–66.
- [85] W. van Aarle, W. J. Palenstijn, J. Cant, E. Janssens, F. Bleichrodt, A. Dabrovolski, J. D. Beenhouwer, K. J. Batenburg, and J. Sijbers. Fast and flexible X-ray tomography using the ASTRA toolbox, *Opt. Express* **24**, no. 22 (Oct. 2016), pp. 25129–25147.
- [86] W. van Aarle, W. J. Palenstijn, J. D. Beenhouwer, T. Altantzis, S. Bals, K. J. Batenburg, and J. Sijbers. The ASTRA Toolbox: A platform for advanced algorithm development in electron tomography, *Ultramicrosc.* **157** (2015), pp. 35–47.
- [87] A. J. Devaney. A filtered backpropagation algorithm for diffraction tomography, *Ultrason. Imaging* **4**, no. 4 (1982), pp. 336–350.
- [88] S. Pan and A. Kak. A computational study of reconstruction algorithms for diffraction tomography: Interpolation versus filtered-backpropagation, *IEEE Trans. Acoust. Speech Signal Process.* **31**, no. 5 (1983), pp. 1262–1275.
- [89] T. Wedberg, J. Stamnes, and W. Singer. Comparison of the filtered backpropagation and the filtered backprojection algorithms for quantitative tomography, *Appl. Opt.* **34**, no. 28 (1995), pp. 6575–6581.
- [90] J. Kostencka and T. Kozacki. Computational and experimental study on accuracy of off-axis reconstructions in optical diffraction tomography, *Opt. Eng.* **54**, no. 2 (2015), pp. 024107–024107.

- [91] W. Choi, C. Fang-Yen, K. Badizadegan, R. R. Dasari, and M. S. Feld. Extended depth of focus in tomographic phase microscopy using a propagation algorithm, *Opt. Lett.* **33**, no. 2 (2008), pp. 171–173.
- [92] A. D. Yablon. Multifocus tomographic algorithm for measuring optically thick specimens, *Opt. Lett.* **38**, no. 21 (Nov. 2013), pp. 4393–4396.
- [93] W. Krauze, A. Kuś, E. Skrzypek, and M. Kujawinska. **Reconstruction method for extended depth-of-field limited-angle tomography**, *Proc. SPIE 10074* (2017), pp. 100741D–1.
- [94] A. Kuś, W. Krauze, and M. Kujawińska. **Focus-tunable lens in limited-angle holographic tomography**, *Proc. SPIE 10070* (2017), pp. 1007009–1.
- [95] N. Tanio and T. Nakanishi. Physical aging and refractive index of poly (methyl methacrylate) glass, *Polym. J.* **38**, no. 8 (2006), pp. 814–818.
- [96] H. Spielmann, M. Balls, J. Dupuis, W. Pape, G. Pechovitch, O. De Silva, H.-G. Holzhütter, R. Clothier, P. Desolle, F. Gerberick, et al. The international EU/COLIPA in vitro phototoxicity validation study: results of phase II (blind trial). Part 1: the 3T3 NRU phototoxicity test, *Toxicol. in vitro* **12**, no. 3 (1998), pp. 305–327.
- [97] K. S. Suvarna, C. Layton, and J. D. Bancroft. *Bancroft's Theory and Practice of Histological Techniques*. Elsevier Health Sciences, 2013.
- [98] G. Dardikman, M. Habaza, L. Waller, and N. T. Shaked. Video-rate processing in tomographic phase microscopy of biological cells using CUDA, *Opt. Express* **24**, no. 11 (2016), pp. 11839–11854.
- [99] A. Kyrieleis, V. Titarenko, M. Ibison, T. Connolley, and P. Withers. Region-of-interest tomography using filtered backprojection: assessing the practical limits, *J. Microscopy* **241**, no. 1 (2011), pp. 69–82.